Florian Engels

Multidimensional Frequency Estimation with Applications in Automotive Radar

Forschungsberichte aus dem Institut für Nachrichtentechnik des Karlsruher Instituts für Technologie

Herausgeber: Prof. Dr. rer. nat. Friedrich Jondral

Forschungsberichte aus dem Institut für Nachrichtentechnik des Karlsruher Instituts für Technologie

Herausgeber: Prof. Dr. rer. nat. Friedrich Jondral

Forschungsberichte aus dem Institut für Nachrichtentechnik des Karlsruher Instituts für Technologie

Herausgeber: Prof. Dr. rer. nat. Friedrich Jondral

Forschungsberichte aus dem Institut für Nachrichtentechnik des Karlsruher Instituts für Technologie

Herausgeber: Prof. Dr. rer. nat. Friedrich Jondral

Vorwort des Herausgebers

Ein Radarsender sendet eine elektromagnetische Welle aus, deren am zu untersuchenden Objekt entstehende Reflektion sodann vom Radarempfänger detektiert und ausgewertet wird. Von einem Radargerät kann nicht nur das Vorhandensein eines reflektierenden Objekts erkannt sondern es können auch dessen Abstand, Geschwindigkeit und Azimut gemessen werden. Natürlich erfasst ein Radargerät gleichzeitig viele Objekte, die getrennt, und darüber hinaus Störungen, die durch die Signalverarbeitung klassifiziert und unterdrückt werden sollen. Radargeräte wurden im großen Stil zunächst für militärische Zwecke und danach in der zivilen Schifffahrt sowie im Luftverkehr eingesetzt. Seit den siebziger Jahren des zwanzigsten Jahrhunderts werden Radare für Anwendungen im Kraftfahrzeug untersucht. Aus modernen Kraftfahrzeugen sind Radarsensoren nicht mehr wegzudenken. Adaptives Abstandhalten, automatisches Abbremsen bei Auffahrgefahr, Warnung vor Verkehrsteilnehmern im toten Winkel des Rückspiegels sind typische Aufgaben. Der rasante Fortschritt der Mikroelektronik sowie die Nutzung höherer Frequenzen haben das ihre dazu beigetragen, dass Radargeräte leicht, klein und preisgünstig geworden sind und in großen Stückzahlen produziert werden. Sowohl im Automotive-Bereich als auch in der Automatisierungstechnik steht der ganz große Durchbruch der Radartechnik erst noch bevor. Dabei werden nicht nur die Geräte (Hardware) sondern auch die Wellenformen, die Detektionsalgorithmen, die Signalauswertung und die Nachverarbeitung (Software) laufend weiterentwickelt.

Besonders komplex sowie algorithmisch und rechentechnisch anspruchsvoll erscheint die Aufgabe eine gleichzeitige und hochauflösende Schätzung von Abstand, Geschwindigkeit und Azimut mehrerer Objekte in Echtzeit durchzuführen. Der Abstand eines Objekts wird über die Laufzeit des Signals vom Radarsender zum Objekt und von dort zurück zum Radarempfänger, seine Relativgeschwindigkeit über die Dopplerverschiebung des Empfangs- gegenüber dem Sendesignal bestimmt. Der Azimut ergibt sich aus der Einfallsrichtung des am Objekt reflektierten Signals. Die oben formulierte Aufgabe kann als dreidimensionales Spektralschätzproblem interpretiert und einer Lösung zugeführt werden. Allerdings ist dabei auch auf die Praktikabilität und Wirtschaftlichkeit des angewendeten Verfahrens zu achten. An dieser Stelle setzt die von Florian Engels vorgelegte Dissertation Multidimensional Frequency Estimation with Applications in Automotive Radar an. Sie beschreibt und bewertet ein praktisch durchführbares, auf der mehrdimensionalen Fourieranalyse basierendes Verfahren zur simultanen Echtzeit-Schätzung von Abstand, Geschwindigkeit und Azimut mehrerer

Objekte und wendet die Ergebnisse zur deutlichen Verbesserung der Leistungsfähigkeit eines handelsüblichen, in großen Stückzahlen produzierten Kfz-Radarsensors an.

Karlsruhe, im Februar 2016 Friedrich Jondral

Multidimensional Frequency Estimation with Applications in Automotive Radar

Zur Erlangung des akademischen Grades eines

DOKTOR-INGENIEURS

von der Fakultät für

Elektrotechnik und Informationstechnik

des Karlsruher Instituts für Technologie

genehmigte

DISSERTATION

von

Florian Engels

geboren in

Wuppertal

Danksagung

Abstract

This thesis considers multidimensional frequency estimation with a focus on computational efficiency and high-resolution capability. A novel framework on multidimensional high-resolution frequency estimation is developed and applied to increase the range, radial velocity, and angular resolution capcability of state-of-the-art automotive radars.

In many practical applications, measurement data can be modelled by the superposition of multidimensional complex sinusoids, also called cisoids. For such a model, an optimal approach for high-resolution frequency estimation is the multidimensional nonlinear least squares (NLS) method, which obtains frequency estimates by minimizing the sum of the squared model deviations with respect to the unknown cisoid frequencies. However, due the dimensionality of that minimization, which is determined by the number of frequency dimensions and the number of cisoids in the model, the computational complexity of the NLS approach is in most cases not feasible. Existing approaches for reducing computational complexity employ pre-processing based on Fourier transformation. A straightforward approach is the application of the NLS methods in the Fourier domain. This can reduce complexity by restricting the minimization to a pre-defined frequency sub-band, which contains a sub-set of cisoid frequencies. However, such an approach is only practical if the number of relevant cisoids is smaller than the total number and their frequencies are concentrated in a knwon frequency sub-band. For a large number of arbitrary cisoid frequencies, estimates can be obtained by peak searching in the periodogram. For well separated cisoids, this provides an approximation of optimal frequency estimation. However, the frequency resolution achievable with periodogram-based estimation is limited. To overcome these limitations, a framework on multidimensional high-resolution frequency estimation is proposed. Fourier-transform pre-processing is employed to select multiple local frequency sub-bands, which are either represented by a local single-cisoid model or a local two-cisoid model. The sub-bands are obtained by the frequency neighborhoods of periodogram peaks. Local periodogram maximization is used to estimate the frequencies of the single-cisoid model, whereas local NLS-based frequency estimation is used for the two-cisoid model. To reduce computational complexity, multidimensional NLS-based frequency estimation is decoupled in a sequence of one-dimensional (1-D) estimation problems. For decoupling, one has to decide on the processing sequence. In one dimension, referred to as resolution dimension, a 1-D NLS-based frequency estimation for two cisoids has to be

performed first. Subsequently, resolved frequencies in the resolution dimension are used for signal component extraction, so that frequency estimation in the remaining dimensions is simplified to two single-cisoid estimation problems. The success of the decoupled approach depends critically on a sufficiently large frequency separation in the resolution dimension. To ensure this, a criterion is proposed for selecting the best resolution dimension adaptively. To further reduce computational complexity, a novel frequency estimation, referred to as single-cisoid search, is proposed, which can replace NLS-based estimation when the cisoid frequencies are distinct in at least two dimensions.

Radar technology is used for target localization in adavnced driver assistance systems (ADAS) and is considered as one of the key technologies for developing ADAS towards highly automated driving (HAD). State-of-the-art automotive radars obtain range, radial velocity, and angle of relevant targets via three-dimensional (3-D) frequency estimation. The frequency resolution which is achievable with conventional radar processing is limited for given system parameters such as bandwidth, coherent processing time, and antenna aperture. To meet critical ADAS and HAD use-cases, increasing the resolution capability is crucial. To achieve this, the proposed framework on multidimensional high-resolution frequency estimation is applied. The effectiveness of that approach is demonstrated with experimental data obtained with a series production automotive radar sensor.

Zusammenfassung

In dieser Dissertation werden mehrdimensionale Verfahren zur Frequenzschätzung betrachtet, wobei besonders auf Recheneffizienz und hohe Auflösungsleistung eingegangen wird. Es wird ein neuartiges Verfahren zur entkoppelten Frequenzschätzung entwickelt, dass angewendet wird, um die Entfernungs-, Radialgeschwindigkeits- und Winkelauflösung von aktuellen Automobilradaren zu erhöhen.

Die Messdaten vieler praktischen Anwendungen lassen sich über die Überlagerung von mehrdimensionalen komlexen Sinustermen, auch Cisoiden genannt, beschreiben. Für solche Modelle ist eine optimale Frequenzschätzung über die Methode der kleinsten Quadrate gegeben, wobei hier berücksichtigt werden muss, dass die Frequenzparameter nichtlinear in das Modell eingehen. Dadurch wird eine hochdimensionale Minimierung notwendig, deren Komplexität durch die Anzahl der Frequenzdimensionen und durch die Modellordnung bestimmmt wird. Dadurch ist der optimale Ansatz für die meisten Anwendungen nicht praktikabel. Ansätze zur Reduizierung der Rechenkomplexität basieren auf Fouriertransformation als Vorverarbeitungsschritt. Ein naheliegender Ansatz ist die Anwendung der Methode der nichlinearen kleinsten Quadrate, die im Fourierbereich angewendet wird. Dadurch kann eine Minimierung auf ein Frequenzband beschränkt werden, dass eine reduzierte Anzahl von Cisoidfrequenzen enthält. Damit dieser Ansatz prakitkabel ist muss die Anzahl relevanter Cisoiden kleiner sein als die Gesamtanzahl. Gleichzeitig müssen die zugehörigen Frequenzen in einem bekannten Frequenzband liegen. Für einen große Anzahl an Cisoid-Frequenzen im gesamten Frequenzband kann Frequenzschätzung über eine Maximumsuche im Periodogramm realisiert werden. Sind alle Cisosid-Frequenzen hinreichend gut separiert wird hierdurch eine Näherung der optimalen Lösung erreicht. Allerdings ist die Auflösungsleistung, die mit dem Periodogramm-Ansatz erreicht werden kann, beschränkt. Daher wird in dieser Arbeit ein neuartiger Ansatz zur hochauflösenden mehrdimensionalen Frequenzschätzung vorgeschlagen der keine der beiden genannten Einschränkungen aufweist. Hier wird Fouriertransformation angewendet, um lokale Frequenzbereiche auszuwählen, die entweder durch ein lokales Ein-Cisoid-Modell oder durch ein lokales Zwei-Cisoid-Modell beschrieben werden können. Für den ersten Fall wird eine lokale Periodogramm-Maximierung zur Frequenzschätzung verwendet, für den zweiten Fall ein NLS-basiertes Verfahren. Letzteres wird rechengünstig realisiert, indem das mehrdmensionale Frequenzschätzproblem in eine Folge von eindimensionalen Problemen zerlegt wird. Hierfür muss eine Verarbeitungsreihenfolge festgelegt werden. Zunächst wird in einer Dimension,

die als Auflösungsdimension bezeichent wird, eine eindimensionale NLS-basierte Frequenzschätzung für das Zwei-Cisoid-Modell durchgeführt. Anschließend werden die so erhaltenen Frequenzen in der Auflösungsdimension verwendet, um die zugehörigen Signalkomponenten zu extrahieren. Dadurch wird die Frequenzschätzung in den verbleibenden Dimensionen auf zwei Schätzprobleme reduziert, die durch ein einfaches Ein-Cisoid-Modell bestimmt sind. Ein solcher Ansatze kann nur erfolgreich sein, wenn eine hinreichende Frequenzseparation in der Auflösungsdimension gegeben ist. Um dies sicherzustellen wird ein Kriterium vorgeschlagen, dass es erlaubt die Auflösungsdimension datenbasiert zu bestimmen. Des Weiteren wird ein rechengünstiges Verfahren zur Frequenzschätzung entwickelt und im entkoppelten Ansatz anstelle der NLS Methode verwendet. Allerdings setzt dieses Verfahren unterschiedliche Cisoid-Frequenzen in mindestens zwei Dimensionen voraus.

Radartechnik wird zur Zielortung in Fahrerassistenzsystemen verwendet und als Schlüsseltechnologie für hochautonomes Fahren angesehen. Aktuelle Automobilradare bestimmen die Entferung, die Radialgeschwindigkeit und den Winkel von relevanten Zielen über dreidimensionale Frequenzschätzung. Die Auflösungsleistung die mit konventioneller Radarsignalverarbeitung erzielt werden kann, wird durch Systemparameter wie Bandbreite, kohärente Messdauer oder Antennenapertur beschränkt. Um kritische Szenarien zu beherrschen ist es zwinged erforderlich, die Auflösungsleistung zu erhöhen. Um dies zu erreichen wird das vorgeschlagene Verfahren zur mehrdmensionalen hochauflösenden Frequenzschätzung angewendet und mit Messungen eines handelsüblichen Radarsensor verifiziert.

Contents

1 Introduction

In this thesis we present a computationally efficient framework on multidimensional frequency estimation with high-resolution capability. We consider applications in automotive radar and use the developed framework to enable high-resolution frequency estimation in the range, radial velocity, and angular dimension of state-of-the-art radar sensors. The introduction is structured as follows. In Section 1.1 we motivate this work. Section 1.2 lists original contributions and Section 1.3 presents the organization of this thesis.

1.1 Motivation

Multidimensional frequency estimation plays an important role in many fields of application such as radar [Kle06], sonar [vT68b], wireless communication [Pes05], and nuclear magnetic resonance (NMR) spectroscopy [LRL98]. For many applications, high-resolution capability, computational efficiency, and memory efficiency are crucial. An important example is automotive radar, which we consider in this thesis.

Radar technology is used for target localization in ADAS and is considered as one of the key technologies for developing ADAS towards HAD. State-of-the-art automotive radar sensors use the chirp-sequence modulation and antenna arrays to determine the range, radial velocity, and angle of targets via 3-D frequency estimation. Computational efficiency and memory efficiency are key requirements for current ADAS and will become even more important for HAD. To meet these requirements, hardware-accelerated fast Fourier transform (FFT) processors are available, which enable computationally efficient pre-processing based on Fourier transformation. Further processing, e.g. frequency estimation, is based on pre-detected peaks in the Fourier-domain data. Due to this, only a small subset of the complete data set has to be stored and memory efficiency is achieved.

Conventional frequency estimation uses the frequencies of pre-detected peaks, which is equivalent to the classical periodogram method. The achievable frequency resolution of the conventional approach is limited by given radar system parameters, such as bandwidth, coherent processing time, and antenna aperture. To meet critical use-cases and to enable recent advances in target tracking, it is crucial to increase frequency resolution beyond the limits of conventional frequency estimation. This

can not be achieved by changing radar system parameters due to limited computation time, small sensor size, or cost restrictions. Therefore, high-resolution frequency estimation becomes necessary. Existing work focuses on high-resolution array processing [Sch10, Hei12], where high-resolution techniques are applied in the so-called spatial domain, that is the original domain of the angular dimension. However, we point out that a much broader class of critical use-cases can be met by applying high-resolution frequency estimation in either the range, the radial velocity, or the angular dimension. To achieve this, the computationally efficient framework on multidimensional high-resolution frequency estimation, which is developed in this thesis, can be incorporated in the processing sequence of state-of-the-art automotive radar sensors.

1.2 Original contributions

We summarize the original contributions of this thesis. We consider multidimensional frequency estimation with focus on computational efficiency and high-resolution capability. In particular, we consider the case, where the data is represented by a superposition of complex sinusoids, also called cisoids, in multiple dimensions.

A framework on multidimensional frequency estimation

We propose a framework on multidimensional high-resolution frequency estimation, which can achieve computational efficiency and memory efficiency and is thus suited for real-time systems. Preprocessing based on Fourier transformation is employed to select frequency sub-bands, which are either represented by a local single-cisoid model or a two-cisoid model and can be obtained as the frequency neighborhoods of periodogram peaks. For the single-cisoid model, frequency estimation is based on periodogram maximization, whereas for the two-cisoid model, a decoupled high-resolution frequency estimation is employed. We present a processing sequence based on decoupled Fourier-domain models, which decide if the single-cisoid model or the two-cisoid model is more appropriate. If a decision in favor of the two-cisoid model is made, the optimal processing sequence for decoupled frequency estimation is determined based on a novel criterion. The proposed framework is also presented in [EHZ$^+$17] for automotive radar applications.

Frequency estimation based on a single-cisoid search

We propose a novel frequency estimation, referred to as single-cisoid search, which can be used within the proposed frequency estimation framework for reducing computational complexity. However, frequency separation in at least two dimensions is required.

Further, we consider applications in automotive radar, where 3-D frequency estimation is used to obtain range, radial velocity, and angle of relevant targets. In critical use-cases, closely spaced targets can not be resolved by conventional radar processing and high-resolution methods are required.

High-resolution processing for automotive radar

> We consider the developed framework on multidimensional high-resolution frequency estimation to enhance the resolution capability of state-of-the-art automotive radars. Due to the flexible decoupled approach of the proposed framework high-resolution capability in the range, the radial velocity, or the angular dimension is obtained. We consider the single-cisoid search approach and combine it with the original decoupled framework to achieve computational efficiency and to cover a broad range of use-cases.

1.3 Overview

Here, we give an overview of this thesis. Chapter 2 introduces the data model in the original domain as well as in the Fourier domain. We present the multidimensional frequency estimation problem and discuss conventional approaches for computationally efficient solutions. In Chapter 3, we develop a framework on multidimensional high-resolution frequency estimation. The general approach is the combination of periodogram-based frequency estimation and local multidimensional high-resolution frequency estimation in a frequency sub-band, which is decoupled into a sequence of 1-D problems to achieve computational efficiency. In Chapter 4, we aim at further reducing complexity and propose a novel computationally efficient frequency estimation, referred to as single-cisoid search, which can be used in a decoupled approach to multidimensional frequency estimation. We propose a bias correction method to correct errors due to frequency discretization. In Chapter 5, we consider applications in automotive radar. In Section 5.1, we give an overview of automotive radar applications, discuss briefly radar principles, and discuss state-of-the-art radar sensors for which we derive the data model. In Section 5.2, we present conventional signal processing for state-of-the-art radar sensors and discuss practical aspects of system design in Section 5.3. In particular, we consider the system parameters of a series production radar sensor. The main contribution of Chapter 5 is high-resolution processing for automotive radars, which is presented in Section 5.4. Here we motivate high-resolution frequency estimation by critical ADAS or HAD use-cases and propose the framework developed in Chapter 3 for high-resolution frequency estimation in either the range, radial velocity, or angular dimension of state-of-the-art radar sensors. In Section 5.4.3, we demonstrate the effectiveness of such an approach by experimental data obtained with a series production radar sensor.

2 Data model and problem formulation

In this chapter, we introduce the data model and discuss the multidimensional frequency estimation problem. In particular, computationally efficient implementations are considered and state-of-the-art approaches to reduce the computational complexity of multidimensional frequency estimation are discussed. For convenience we consider three-dimensional data. However, this constitutes no loss of generality as the data model as well as the proposed approaches for frequency estimation can be straightforwardly extended to an arbitrary number of data dimensions.

In Section 2.1 we consider the original-domain data model, discuss pre-processing based on Fourier transformation, and develop the corresponding Fourier-domain data model. Section 2.2, discusses multidimensional frequency estimation, where the focus is on low computational complexity and high-resolution capability.

2.1 Data model

Consider a superposition of 3-D complex sinusoids, also called cisoids,

$$x(l_s, m_s, n_s) = \sum_{k=1}^{K_c} a_k e^{j(\lambda_k l_s + \mu_k m_s + \nu_k n_s)} + \xi(l_s, m_s, n_s), \tag{2.1}$$

$$l_s = 0, \ldots, L_s - 1, \quad m_s = 0, \ldots, M_s - 1, \quad n_s = 0, \ldots, N_s - 1,$$

where L_s, M_s, N_s denotes the sample support in each dimension, K_c denotes the number of cisoids, and λ_k, μ_k, ν_k, a_k denote normalized frequencies and complex amplitude of cisoid k, respectively. The frequencies as well as the complex amplitudes are unknown but deterministic and $\xi(l_s, m_s, n_s)$ denotes circular complex white Gaussian noise with covariance function

$$\mathrm{E}\big\{\xi(l_s, m_s, n_s)\, \xi^*(\tilde{l}_s, \tilde{m}_s, \tilde{n}_s)\big\} = \sigma^2\, \delta_{l_s, \tilde{l}_s}\, \delta_{m_s, \tilde{m}_s}\, \delta_{n_s, \tilde{n}_s}. \tag{2.2}$$

Herein $\mathrm{E}\{\cdot\}$ is the expected value and δ the Kronecker-Delta. Multidimensional sum-of-cisoid models such as (2.1) apply for many practical applications, like radar processing [Kle06, GMP12, Fri08], channel sounding for wireless communication systems [HBN98, RHST00], or multichannel nuclear magnetic resonance (NMR) spectroscopy [LRL98].

2 Data model and problem formulation

An important special case are so called frequency selective applications, which are only concerned with cisoids lying in a predefined frequency sub-band. The motivation for this can be for instance, that the sum of cisoid model may only apply in that sub-band, or the number of cisoids in the complete frequency band is huge, so that a cisoid sub-set has to be considered to reduce the computational complexity. Examples of sub-band frequency estimation include interference cancellation in array processing [ZL91a], NMR spectroscopy [PSH08, VSH+00], electroencephalogram (EEG) signal processing, magnetoencephalogram (MEG) signal processing [RBVW06, RRH14], audio processing [ZCD+09], and fault detection for induction machines [KHC07].

A natural pre-processing step for sub-band frequency estimation is the discrete time Fourier transform (DTFT) of the data samples

$$
\begin{aligned}
&X\left(\lambda, \mu, \nu\right) \\
&= \sum_{l_s=0}^{L_s-1} \sum_{m_s=0}^{M_s-1} \sum_{n_s=0}^{N_s-1} w_\lambda(l_s) w_\mu(m_s) w_\nu(n_s)\, x(l_s, m_s, n_s)\, e^{-j(\lambda l_s + \mu m_s + \nu n_s)},
\end{aligned} \quad (2.3)
$$

where the frequencies $\lambda \in (\lambda_a, \lambda_b)$, $\mu \in (\mu_a, \mu_b)$, $\nu \in (\nu_a, \nu_b)$, lie within a predefined frequency sub-band, which is bounded by λ_a, λ_b, μ_a, μ_b, ν_a, and ν_b. The window functions $w_\lambda(l)$, $w_\mu(m)$, $w_\nu(n)$ are needed to attenuate out-of-band interference. Typical window functions can be found in [Har78].

Substituting the original-domain model (2.1) in (2.3), yields the Fourier-domain data model

$$
X\left(\lambda, \mu, \nu\right) = \sum_{k=1}^{K} a_k W_\lambda\left(\lambda - \lambda_k\right) W_\mu\left(\mu - \mu_k\right) W_\nu\left(\nu - \nu_k\right) + \Xi(\lambda, \mu, \nu), \quad (2.4)
$$

$$
\{\lambda, \lambda_1, \ldots, \lambda_K\} \in (\lambda_a, \lambda_b), \ \{\mu, \mu_1, \ldots, \mu_K\} \in (\mu_a, \mu_b), \ \{\nu, \nu_1, \ldots, \nu_K\} \in (\nu_a, \nu_b).
$$

Herein, $K \leq K_c$ is the number of cisoids, whose frequencies lie in the predefined frequency sub-band, and

$$
W_\lambda\left(\lambda\right) = \sum_{l_s=0}^{L_s-1} w_\lambda(l_s)\ e^{-j\lambda l_s} \quad (2.5)
$$

$$
W_\mu\left(\mu\right) = \sum_{m_s=0}^{M_s-1} w_\mu(m_s) e^{-j\mu m_s} \quad (2.6)
$$

$$
W_\nu\left(\nu\right) = \sum_{n_s=0}^{N_s-1} w_\nu(n_s)\ e^{-j\nu n_s} \quad (2.7)
$$

are the DTFT of the window functions $w_\lambda(l)$, $w_\mu(m)$, $w_\nu(n)$, respectively. The DTFT of the noise

$$
\begin{aligned}
&\Xi\left(\lambda, \mu, \nu\right) \\
&= \sum_{l_s=0}^{L_s-1} \sum_{m_s=0}^{M_s-1} \sum_{n_s=0}^{N_s-1} w_\lambda(l_s) w_\mu(m_s) w_\nu(n_s)\, \xi(l_s, m_s, n_s)\, e^{-j(\lambda l_s + \mu m_s + \nu n_s)}
\end{aligned} \quad (2.8)
$$

is circular complex Gaussian, as the noise in the original-domain ξ is white, circular complex Gaussian and the DTFT is a linear transformation. The covariance function of (2.8) is obtained by direct calculation and by considering the covariance function in (2.2)

$$\mathrm{E}\{\Xi\left(\lambda_j, \mu_j, \nu_j\right)\Xi^*\left(\lambda_k, \mu_k, \nu_k\right)\} = \sigma^2 C_\lambda\left(\lambda_k - \lambda_j\right) C_\mu\left(\mu_k - \mu_j\right) C_\nu\left(\nu_k - \nu_j\right), \quad (2.9)$$

where

$$C_\lambda\left(\lambda\right) = \sum_{l_s=0}^{L_s-1} w_\lambda^2(l_s)e^{j\lambda l_s}, \quad (2.10)$$

$$C_\mu\left(\mu\right) = \sum_{m_s=0}^{M_s-1} w_\mu^2(m_s)e^{j\mu m_s}, \quad (2.11)$$

$$C_\nu\left(\nu\right) = \sum_{n_s=0}^{N_s-1} w_\nu^2(n_s)e^{j\nu n_s}. \quad (2.12)$$

Observe from (2.9), that the noise in the Fourier domain is in contrast to the noise in the original domain not white but colored.

The Fourier-domain representation of typical window functions, e.g as considered in [Har78], is concentrated in the mainlobe, which is centered at zero. Consequently, the shifted versions in (2.4) are concentrated around the respective cisoid frequencies. As those lie in the predefined sub-band, all K cisoids are well represented in (2.4) and the sub-band model is feasible.

Two important use-cases for the Fourier-domain model can be distinguished. The first is reducing the computational complexity of frequency estimation in the original-domain, which can be achieved by considering only $K < K_c$ cisoids in a frequency estimation based on model (2.4). The second use-case is that the original-domain model (2.1) applies only locally in a predefined frequency sub-band. In that case, model (2.4) with $K = K_c$ can be used for frequency estimation.

Frequency grid

Calculating the DTFT on a normalized frequency grid enables practical frequency estimation based on (2.3). To this end, the DTFT can be calculated via the discrete Fourier transform (DFT), which employs an equidistant frequency grid

$$\begin{aligned}
&\left\{\Delta_\lambda l \;\;\middle|\; l \;\; = 0, \ldots, L_{\mathrm{DFT}}-1\right\} \\
&\left\{\Delta_\mu m \middle|\, m = 0, \ldots, M_{\mathrm{DFT}}-1\right\} \\
&\left\{\Delta_\nu n \;\;\middle|\; n \;\; = 0, \ldots, N_{\mathrm{DFT}}-1\right\}
\end{aligned}$$

Herein, $\Delta_\lambda = 2\pi/L_{\mathrm{DFT}}$, $\Delta_\mu = 2\pi/M_{\mathrm{DFT}}$, $\Delta_\nu = 2\pi/N_{\mathrm{DFT}}$, is the frequency step size and L_{DFT}, M_{DFT}, N_{DFT} are arbitrary grid sizes. A common choice is $L_{\mathrm{DFT}} = L_s$, $M_{\mathrm{DFT}} = M_s$, $N_{\mathrm{DFT}} = N_s$, which enables to use the computationally efficient FFT algorithm for calculating (2.3) [CT65]. If a finer grid $L_{\mathrm{DFT}} > L_s$, $M_{\mathrm{DFT}} > M_s$, $N_{\mathrm{DFT}} > N_s$ is needed, the FFT algorithm can still be employed, but $L_{\mathrm{DFT}} - L_s$, $M_{\mathrm{DFT}} - M_s$, $N_{\mathrm{DFT}} - N_s$, zeros have to be appended to the original-domain samples. This is known as zero-padding and increases the computations required for the FFT [OSB98].

For the sub-band Fourier-domain model (2.4), only a subset of DFT frequencies, which lie in the sub-band, is needed

$$\{\Delta_\lambda l \mid l = l_a, \ldots, l_b\}, \quad l_a = \lceil \lambda_a/\Delta_\lambda \rceil, \quad l_b = \lfloor \lambda_b/\Delta_\lambda \rfloor \qquad (2.13)$$

$$\{\Delta_\mu m \mid m = m_a, \ldots, m_b\}, \quad m_a = \lceil \mu_a/\Delta_\mu \rceil, \quad m_b = \lfloor \mu_b/\Delta_\mu \rfloor \qquad (2.14)$$

$$\{\Delta_\nu n \mid n = n_a, \ldots, n_b\}, \quad n_a = \lceil \nu_a/\Delta_\nu \rceil, \quad n_b = \lfloor \nu_b/\Delta_\nu \rfloor \qquad (2.15)$$

where $\lfloor \cdot \rfloor$ and $\lceil \cdot \rceil$ denote the floor and ceiling functions, respectively. If the cardinalities of (2.13), (2.14), (2.15), $L = l_b - l_a + 1$, $M = m_b - m_a + 1$, $N = n_b - n_a + 1$, are much smaller than the complete grid sizes L_{DFT}, M_{DFT}, N_{DFT}, the chirp-Z transform [RSR69] can be used to efficiently calculate (2.3) for the subset of frequency samples and thus avoid a complete FFT calculation.

For convenience we use the same functional notation for $X(\cdot)$ in the case of continuous and discrete variables. Thus $X(l, m, n) = X(\Delta_\lambda l, \Delta_\mu m, \Delta_\nu n)$ is (2.3) evaluated at the corresponding DFT frequencies.

2.2 Problem formulation

The main objective of this thesis is the estimation of the cisoid frequencies in (2.1) from either original-domain or Fourier-domain samples, in a computational and memory efficient way. This is a special case of multidimensional frequency estimation, which is extensively covered in the literature [CS94, HN98, Pes05, NS10, PPG12].

An optimal approach to multidimensional frequency estimation is fitting the time-domain model (2.1). However, this requires a computational demanding optimization in $3K_c$ dimensions. In particular for large K_c, this is not practical. To circumvent a high-dimensional optimization, subspace methods have been proposed. However, these require an eigendecomposition of a $L_s M_s N_s$-dimensional matrix and additional pre-processing, as only a single observation of (2.1) is available due to measurement-time restrictions. This is known as single-snapshot or coherent sources case in the literature. The computational complexity of the eigendecomposition, which is determined by the sample support $O(L_s M_s N_s)^3$ [GvL96], limits the practical relevance of subspace approaches whenever computation time is crucial. This holds in particular

for large a sample support. As the focus here is on computational efficiency, we do not consider multidimensional frequency estimation in the original-domain.

Rather, we consider two state-of-the-art approaches for computationally efficient multidimensional frequency estimation, which are both based on the Fourier-domain model (2.4). The first, considered in Section 2.2.1, is based on NLS fitting of the sub-band Fourier-domain model. Therefore it is only reasonable if a frequency sub-band with a reduced number of cisoids $K \ll K_c$ can be identified. The second, discussed in Section 2.2.2, is the classical periodogram approach, which works without a sub-band restriction and can handle K_c cisoids in the complete frequency range. However, it has no high-resolution capability, which is required for many practical applications.

In this thesis, we combine NLS-based frequency estimation in the Fourier-domain with periodogram-based frequency estimation to overcome their respective limitations. To this end, we develop a framework in Chapter 3.

2.2.1 Sub-band nonlinear least squares

The Fourier-domain model (2.4) can be straightforwardly applied in an NLS frequency estimation. To achieve computational efficiency a frequency sub-band with a reduced number of practically relevant cisoids has to be identified so that the Fourier-domain model with $K \ll K_c$ can be used. Note that depending on the application this might not be possible and thus the practicality of such an approach is limited. We proceed as follows: we introduce necessary notation, derive the optimal maximum likelihood (ML) estimator, and simplify it to obtain the NLS estimator, which achieves almost the same performance in practice.

Consider the following vectorization of (2.4) evaluated on a frequency grid

$$[\mathbf{x}]_i = X\left(l_i, m_i, n_i\right), \tag{2.16}$$

where the indices

$$l_i = l_a + \frac{i}{MN} \quad \mathrm{mod}\ L, \quad m_i = m_a + \frac{i}{N} \quad \mathrm{mod}\ M, \quad n_i = n_a + i \quad \mathrm{mod}\ N,$$

are such that (2.16) has a row-major order, which is a common sequential representation of multidimensional arrays [Knu97, Sec. 2.2.6]. Substituting (2.4) in (2.16), yields the model

$$\mathbf{x} = \mathbf{W}_K\left(\boldsymbol{\lambda}_K, \boldsymbol{\mu}_K, \boldsymbol{\nu}_K\right)\mathbf{a}_K + \boldsymbol{\xi}, \tag{2.17}$$

where $\mathbf{a}_K = [a_1, \ldots, a_K]^{\mathrm{T}}$, $[\boldsymbol{\xi}]_i = \Xi(\Delta_\lambda l_i, \Delta_\mu m_i, \Delta_\nu n_i)$, $\boldsymbol{\lambda}_K = [\lambda_1, \ldots, \lambda_K]^{\mathrm{T}}$, $\boldsymbol{\mu}_K = [\mu_1, \ldots, \mu_K]^{\mathrm{T}}$, and $\boldsymbol{\nu}_K = [\nu_1, \ldots, \nu_K]^{\mathrm{T}}$. Due to the row-major order of (2.16), the model matrix in (2.17) is

$$\mathbf{W}_K\left(\boldsymbol{\lambda}_K, \boldsymbol{\mu}_K, \boldsymbol{\nu}_K\right)$$
$$= [\mathbf{w}_\lambda\left(\lambda_1\right) \otimes \mathbf{w}_\mu\left(\mu_1\right) \otimes \mathbf{w}_\nu\left(\nu_1\right), \ldots, \mathbf{w}_\lambda\left(\lambda_K\right) \otimes \mathbf{w}_\mu\left(\mu_K\right) \otimes \mathbf{w}_\nu\left(\nu_K\right)]$$

where $\otimes$ denotes the Kronecker product and

$$\mathbf{w}_\lambda\left(\lambda\right) = [W_\lambda(\Delta_\lambda l_a\ -\lambda),\ldots,W_\lambda(\Delta_\lambda l_b\ -\lambda)]^\mathrm{T} \tag{2.18}$$

$$\mathbf{w}_\mu\left(\mu\right) = [W_\mu(\Delta_\mu m_a-\mu),\ldots,W_\mu(\Delta_\mu m_b-\mu)]^\mathrm{T} \tag{2.19}$$

$$\mathbf{w}_\nu\left(\nu\right) = [W_\nu(\Delta_\nu n_a\ -\nu),\ldots,W_\nu(\Delta_\nu n_b\ -\nu)]^\mathrm{T} \tag{2.20}$$

In a maximum likelihood estimation, the likelihood function of model (2.17) is maximized with respect to the unknown parameters $\boldsymbol{\lambda}_K$, $\boldsymbol{\mu}_K$, $\boldsymbol{\nu}_K$, $\mathbf{a}_K$, and σ^2. The likelihood function is given by the conditional distribution of (2.17)

$$p\left(\mathbf{x}\mid\boldsymbol{\lambda}_K,\boldsymbol{\mu}_K,\boldsymbol{\nu}_K,\mathbf{a}_K,\sigma^2\right)$$
$$= \frac{1}{(\pi\sigma^2)^{LMN}\det\left(\mathbf{C}\right)}\,e^{-[\mathbf{x}-\mathbf{W}_K(\boldsymbol{\lambda}_K,\boldsymbol{\mu}_K,\boldsymbol{\nu}_K)\mathbf{a}_K]^\mathrm{H}\mathbf{C}^{-1}[\mathbf{x}-\mathbf{W}_K(\boldsymbol{\lambda}_K,\boldsymbol{\mu}_K,\boldsymbol{\nu}_K)\mathbf{a}_K]/\sigma^2} \tag{2.21}$$

where $\mathbf{C} = \mathbf{C}_\lambda \otimes \mathbf{C}_\mu \otimes \mathbf{C}_\nu$ and

$$[\mathbf{C}_\lambda]_{i,j} = C_\lambda\left(\Delta_\lambda\left(j-i\right)\right),\quad [\mathbf{C}_\mu]_{i,j} = C_\mu\left(\Delta_\mu\left(j-i\right)\right),\quad [\mathbf{C}_\nu]_{i,j} = C_\nu\left(\Delta_\nu\left(j-i\right)\right).$$

Note that (2.21) follows directly from the circular complex Gaussian distribution of the noise vector $\boldsymbol{\xi}$ and the covariance function in (2.9). Equivalent results can be obtained by minimizing the negative log-likelihood function

$$-\ln p\left(\mathbf{x}\mid\boldsymbol{\lambda}_K,\boldsymbol{\mu}_K,\boldsymbol{\nu}_K,\mathbf{a}_K,\sigma^2\right)$$
$$= \mathrm{const} + LMN\ln\sigma^2$$
$$+\frac{1}{\sigma^2}\left[\mathbf{x}-\mathbf{W}_K\left(\boldsymbol{\lambda}_K,\boldsymbol{\mu}_K,\boldsymbol{\nu}_K\right)\mathbf{a}_K\right]^\mathrm{H}\mathbf{C}^{-1}\left[\mathbf{x}-\mathbf{W}_K\left(\boldsymbol{\lambda}_K,\boldsymbol{\mu}_K,\boldsymbol{\nu}_K\right)\mathbf{a}_K\right], \tag{2.22}$$

which can be concentrated with respect to the noise variance. Equating the derivative of (2.22) with respect to σ^2 to zero yields

$$\sigma^2 = \frac{1}{LMN}\left[\mathbf{x}-\mathbf{W}_K\left(\boldsymbol{\lambda}_K,\boldsymbol{\mu}_K,\boldsymbol{\nu}_K\right)\mathbf{a}_K\right]^\mathrm{H}\mathbf{C}^{-1}\left[\mathbf{x}-\mathbf{W}_K\left(\boldsymbol{\lambda}_K,\boldsymbol{\mu}_K,\boldsymbol{\nu}_K\right)\mathbf{a}_K\right].$$

Using this in (2.22)

$$\mathrm{const} + LMN\ln\Big(\underbrace{\left[\mathbf{x}-\mathbf{W}_K\left(\boldsymbol{\lambda}_K,\boldsymbol{\mu}_K,\boldsymbol{\nu}_K\right)\mathbf{a}_K\right]^\mathrm{H}\mathbf{C}^{-1}\left[\mathbf{x}-\mathbf{W}_K\left(\boldsymbol{\lambda}_K,\boldsymbol{\mu}_K,\boldsymbol{\nu}_K\right)\mathbf{a}_K\right]}_{\text{ML criterion function}}\Big)$$

allows to minimize the ML criterion function, which is independent of the noise variance, with respect to $\boldsymbol{\lambda}_K$, $\boldsymbol{\mu}_K$, $\boldsymbol{\nu}_K$, and $\mathbf{a}_K$.

To simplify ML frequency estimation further we approximate $\mathbf{C} \approx \mathbf{I}$, so that the ML criterion function reduces to the NLS criterion function

$$\left\|\mathbf{x}-\mathbf{W}_K\left(\boldsymbol{\lambda}_K,\boldsymbol{\mu}_K,\boldsymbol{\nu}_K\right)\mathbf{a}_K\right\|^2, \tag{2.23}$$

which can be concentrated with respect to the cisoid amplitudes. To see this, observe that for known $\boldsymbol{\lambda}_K$, $\boldsymbol{\mu}_K$, $\boldsymbol{\nu}_K$ the cisoid amplitudes can be obtained as

$\mathbf{a}_K = \mathbf{W}_K^+ \left(\boldsymbol{\lambda}_K, \boldsymbol{\mu}_K, \boldsymbol{\nu}_K \right) \mathbf{x}$. Inserting this in (2.23) and after manipulations, yields the NLS frequency estimator

$$\hat{\boldsymbol{\lambda}}_K, \hat{\boldsymbol{\mu}}_K, \hat{\boldsymbol{\nu}}_K = \arg \max_{\boldsymbol{\lambda}_K, \boldsymbol{\mu}_K, \boldsymbol{\nu}_K} \left\| \mathbf{W}_K \left(\boldsymbol{\lambda}_K, \boldsymbol{\mu}_K, \boldsymbol{\nu}_K \right) \mathbf{W}_K^+ \left(\boldsymbol{\lambda}_K, \boldsymbol{\mu}_K, \boldsymbol{\nu}_K \right) \mathbf{x} \right\|^2. \quad (2.24)$$

With (2.24), the number of real parameters in the optimization is reduced from $5K$ for the ML estimation to $3K$. The performance of NLS estimator is asymptotically equivalent to the optimal ML estimator [SJL97].

Note, that model (2.17) could be used in a subspace approach. However, this requires the noise vector to be white. To achieve this in (2.17) a frequency grid with $L_{\mathrm{DFT}} = L_s$, $M_{\mathrm{DFT}} = M_s$, $N_{\mathrm{DFT}} = N_s$ has to be used and window functions are restricted to the rectangular window. Using such a frequency grid constitutes no practical restriction, whereas the rectangular window is not feasible in a sub-band approach. This is due to its high sidelobe level (SLL), which leads to a poor out-of-band cisoids suppression and therefore to a violation of the white noise assumption. In principle, window functions with a lower SLL could be used in combination with pre-whitening. However, pre-whitening increases the effective SLL [vT02, Sec. 3.10] and thus leads again to a poor out-of-band cisoids suppression. Therefore, we do not consider subspace approaches here.

2.2.2 Periodogram

If it is not possible to identify an application-relevant frequency sub-band, a common approach to frequency estimation is based on the periodogram. The periodogram was first introduced by Schuster in 1898 [Sch98] to reveal hidden periodicities in time series. It constitutes a classical non-parametric spectral estimation method [Tho82, Bri81] and is as such applied e.g. in spectral sensing for cognitive radios [MLJ09]. For the model (2.1) and well separated cisoids it provides an approximation to optimal frequency estimation in the original domain [SM05] and is thus widely used in radar signal processing [Ric14]. The periodogram is simply the squared magnitude of the DTFT in (2.3), considered for the complete frequency range

$$P \left(\lambda, \mu, \nu \right) = \left| X \left(\lambda, \mu, \nu \right) \right|^2, \quad \lambda \in (0, 2\pi], \ \mu \in (0, 2\pi], \ \nu \in (0, 2\pi]. \quad (2.25)$$

The periodogram frequency estimates are then the frequencies corresponding to the K_c largest peaks of (2.25). Note that in most applications K_c is not known and has to be estimated. For example in radar signal processing, K_c is obtained prior to parameter estimation by power detection [RSH10, Ch.15/16].

The main advantage of periodogram-based frequency estimation is computationally efficiency, which is achieved by the FFT, as discussed in Section 2.1, followed by a peak search. Its main drawback is limited resolution. Periodogram-based frequency

estimation can resolve two cisoids only, if their frequency separation exceeds the respective resolution limit

$$F_\lambda = \frac{2\pi}{L_s}, \quad F_\mu = \frac{2\pi}{M_s}, \quad F_\nu = \frac{2\pi}{N_s}, \tag{2.26}$$

in at least one dimension. Only if this holds for every possible cisoid pair, the periodogram provides a good approximation of optimal frequency estimation [SM05].

Note that (2.26) are known as Fourier, Rayleigh, or periodogram resolution limits [SM05]. The Fourier limits are equal to the mainlobe width (MLW) of the respective rectangular window functions. For window functions with larger MLW the effective resolution limits are larger than the Fourier limits [Har78].

2.A Appendix

2.A.1 Window functions

Here we discuss properties and representations of window functions $w_\lambda(l)$, $w_\mu(m)$, $w_\nu(n)$, which are needed in the course of this thesis. A detailed discussion can be found in [Har78].

In this thesis, we consider window functions, which are real, non-negative, symmetric around $(L_s - 1)/2$, $(M_s - 1)/2$, $(N_s - 1)/2$, respectively, and normalized

$$\sum_{l_s=0}^{L_s-1} w_\lambda(l_s) = \sum_{m_s=0}^{M_s-1} w_\mu(m_s) = \sum_{n_s=0}^{N_s-1} w_\nu(n_s) = 1.$$

The DTFT of such window functions as in (2.5), (2.6), (2.7) can be written as

$$W_\lambda(\lambda) = \Omega_\lambda(\lambda)\, e^{-j\frac{L_s-1}{2}\lambda} \tag{2.27}$$

$$W_\mu(\mu) = \Omega_\mu(\mu)\, e^{-j\frac{M_s-1}{2}\mu} \tag{2.28}$$

$$W_\nu(\nu) = \Omega_\nu(\nu)\, e^{-j\frac{N_s-1}{2}\nu} \tag{2.29}$$

where

$$\Omega_\lambda(\lambda) = \sum_{l_s=0}^{L_s-1} w_\lambda(l_s)\ \cos\left(\lambda\left[l_s - \frac{L_s-1}{2}\right]\right) \tag{2.30}$$

$$\Omega_\mu(\mu) = \sum_{m_s=0}^{M_s-1} w_\mu(m_s) \cos\left(\mu\left[m_s - \frac{M_s-1}{2}\right]\right) \tag{2.31}$$

$$\Omega_\nu(\nu) = \sum_{n_s=0}^{N_s-1} w_\nu(n_s)\ \cos\left(\nu\left[n_s - \frac{N_s-1}{2}\right]\right) \tag{2.32}$$

denote amplitude functions, which are real, symmetric, 2π periodic, and have a global maximum at $\lambda = 0$, $\mu = 0$, $\nu = 0$, respectively. Due to the normalization of the original-domain window function we have $\Omega_\lambda(0) = \Omega_\mu(0) = \Omega_\nu(0) = 1$.

We can derive (2.29) by writing

$$W_\nu(\nu) = e^{-j\frac{N_s-1}{2}\nu} \sum_{n_s=0}^{N_s-1} w_\nu(n_s) e^{-j\nu\left(n_s - \frac{N_s-1}{2}\right)}$$

$$= e^{-j\frac{N_s-1}{2}\nu} \left[\Omega_\nu(\nu) - j \underbrace{\sum_{n_s=0}^{N_s-1} w_\nu(n_s)\sin\left(\nu\left[n_s - \frac{N_s-1}{2}\right]\right)}_{=0}\right],$$

where the last term is zero because w_λ is by assumption symmetric around $(N_s - 1)/2$ and the sine is an odd function. The same argument holds for (2.27), (2.28). The symmetry, periodicity, and the global maximum position follow directly from (2.30), (2.31), (2.32) as the cosine is even, 2π periodic, and has range $(-1, 1)$.

Mainlobe width and sidelobe level

Two performance indicators of window functions are the MLW and the SLL. The first determines the resolution performance [Har78] and the latter the out-of-band interference suppression.

The MLW is defined as the smallest positive null of the Fourier-domain window function. In particular

$$\mathrm{MLW}_\lambda, \quad \mathrm{MLW}_\mu, \quad \mathrm{MLW}_\nu,$$

are equal to the smallest positive null of (2.30), (2.31), (2.32), respectively. The SLL is defined as

$$\mathrm{SLL}_\lambda = \Omega_\lambda^2 (\lambda_{\mathrm{SL}}), \quad \mathrm{SLL}_\mu = \Omega_\mu^2 (\mu_{\mathrm{SL}}), \quad \mathrm{SLL}_\nu = \Omega_\nu^2 (\nu_{\mathrm{SL}})$$

where λ_{SL}, μ_{SL}, ν_{SL} denote the position of the second largest peak of $\Omega_\lambda^2(\lambda)$, $\Omega_\mu^2(\mu)$, $\Omega_\nu^2(\nu)$, respectively.

Figure 2.1 shows the MLW and the SLL for a rectangular window $w_\lambda(l) = 1$. On the left-hand side, the squared magnitude of the Fourier-domain window function for the complete normalized frequency range is shown. On the right-hand side, the region around zero is shown and the MLW and SLL are marked. For the rectangular window we have [Har78]

$$\mathrm{MLW}_\lambda = \frac{2\pi}{L_s}, \quad \mathrm{MLW}_\mu = \frac{2\pi}{M_s}, \quad \mathrm{MLW}_\nu = \frac{2\pi}{N_s},$$
$$\mathrm{SLL}_\lambda = \mathrm{SLL}_\mu = \mathrm{SLL}_\nu = 13\,\mathrm{dB}.$$
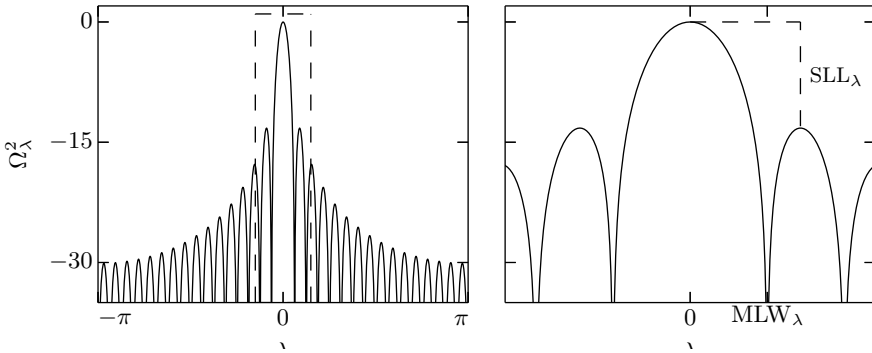
Figure 2.1: Fourier-domain window function for the rectangular window (left) with marked MLW$_\lambda$ and SLL$_\lambda$ (right).

Derivatives

The derivatives of the Fourier-domain window functions (2.5), (2.6), (2.7), are given by

$$\dot{W}_\lambda(\lambda) = -\sum_{l_s=0}^{L_s-1} j\, l_s w_\lambda(l_s)\quad e^{-j\lambda l_s}, \tag{2.33}$$

$$\dot{W}_\mu(\mu) = -\sum_{m_s=0}^{M_s-1} j\, m_s w_\mu(m_s)\, e^{-j\mu m_s}, \tag{2.34}$$

$$\dot{W}_\nu(\nu) = -\sum_{n_s=0}^{N_s-1} j\, n_s w_\nu(n_s)\quad e^{-j\nu n_s}, \tag{2.35}$$

respectively. The derivatives of the window amplitude functions (2.30), (2.31), (2.32), are

$$\dot{\Omega}_\lambda(\lambda) = -\sum_{l_s=0}^{L_s-1} w_\lambda(l_s)\ \left(l_s - \frac{L_s-1}{2}\right) \sin\left[\lambda\left(l_s - \frac{L_s-1}{2}\right)\right], \tag{2.36}$$

$$\dot{\Omega}_\mu(\mu) = -\sum_{m_s=0}^{M_s-1} w_\mu(m_s)\left(m_s - \frac{M_s-1}{2}\right) \sin\left[\mu\left(m_s - \frac{M_s-1}{2}\right)\right], \tag{2.37}$$

$$\dot{\Omega}_\nu(\nu) = -\sum_{n_s=0}^{N_s-1} w_\nu(n_s)\ \left(n_s - \frac{N_s-1}{2}\right) \sin\left[\nu\left(n_s - \frac{N_s-1}{2}\right)\right], \tag{2.38}$$

respectively. This follows from direct calculation.

2.A.2 Accuracy and resolution

The accuracy of any unbiased estimator can be assessed by the Cramér Rao bound (CRB), which represents a lower bound on the estimation error variance [vT68a]. For a given frequnecy sub-band we derive the CRB matrix for model (2.17).

Another crucial concept regarding frequency estimation is resolution. We adopt a commonly used resolution definition and consider two cisoids resolved if we can estimate their frequencies such that

$$\sqrt{\left(\hat{\lambda}_1 - \lambda_1\right)^2 + \left(\hat{\mu}_1 - \mu_1\right)^2 + \left(\hat{\nu}_1 - \nu_1\right)^2} < \frac{\delta}{2} \quad \wedge$$

$$\sqrt{\left(\hat{\lambda}_2 - \lambda_2\right)^2 + \left(\hat{\mu}_2 - \mu_2\right)^2 + \left(\hat{\nu}_2 - \nu_2\right)^2} < \frac{\delta}{2}. \tag{2.39}$$

Herein, λ_1, μ_1, ν_1, λ_2, μ_2, ν_2, $\hat{\lambda}_1$, $\hat{\mu}_1$, $\hat{\nu}_1$, $\hat{\lambda}_2$, $\hat{\mu}_2$, $\hat{\nu}_2$, are the true and estimated cisoid frequencies, respectively, and

$$\delta = \sqrt{\left(\lambda_2 - \lambda_1\right)^2 + \left(\mu_2 - \mu_1\right)^2 + \left(\nu_2 - \nu_1\right)^2}$$

is the frequency separation.

Cramér Rao bound

We derive the CRB for the sub-band, Fourier-domain model (2.17). To this end, consider the parameter vector

$$\left[\text{Re}\left\{\mathbf{a}_{K_c}\right\}, \text{Im}\left\{\mathbf{a}_{K_c}\right\}, \boldsymbol{\lambda}_{K_c}, \boldsymbol{\mu}_{K_c}, \boldsymbol{\nu}_{K_c}\right]^{\text{T}},$$

representing all K_c cisoids. Note that only K of the K_c cisoids frequencies lie within the sub-band Cisoids with frequencies outside the sub-band are considered as interference and will degrade the accuracy when estimating the K cisoid parameters of interest via the sub-band approach.

Applying the results in [SL01, SJL97] to model (2.17) yields

$$\mathbf{CRB} = \frac{\sigma^2}{2}\text{Re}\left\{\mathbf{G}^{\text{H}}\mathbf{C}^{-1}\mathbf{G}\right\}^{-1}, \tag{2.40}$$

where

$$\mathbf{G} = \left[\mathbf{W}_{K_c}(\boldsymbol{\lambda}_{K_c}, \boldsymbol{\mu}_{K_c}, \boldsymbol{\nu}_{K_c}), j\mathbf{W}_{K_c}(\boldsymbol{\lambda}_{K_c}, \boldsymbol{\mu}_{K_c}, \boldsymbol{\nu}_{K_c}), \mathbf{D}_\lambda, \mathbf{D}_\mu, \mathbf{D}_\nu\right]$$

$$\mathbf{D}_\lambda = \left[a_1\dot{\mathbf{w}}_\lambda\left(\lambda_1\right) \otimes \mathbf{w}_\mu\left(\mu_1\right) \otimes \mathbf{w}_\nu\left(\nu_1\right), \ldots, a_{K_c}\dot{\mathbf{w}}_\lambda\left(\lambda_{K_c}\right) \otimes \mathbf{w}_\mu\left(\mu_{K_c}\right) \otimes \mathbf{w}_\nu\left(\nu_{K_c}\right)\right]$$

$$\mathbf{D}_\mu = \left[a_1\mathbf{w}_\lambda\left(\lambda_1\right) \otimes \dot{\mathbf{w}}_\mu\left(\mu_1\right) \otimes \mathbf{w}_\nu\left(\nu_1\right), \ldots, a_{K_c}\mathbf{w}_\lambda\left(\lambda_{K_c}\right) \otimes \dot{\mathbf{w}}_\mu\left(\mu_{K_c}\right) \otimes \mathbf{w}_\nu\left(\nu_{K_c}\right)\right]$$

$$\mathbf{D}_\nu = \left[a_1\mathbf{w}_\lambda\left(\lambda_1\right) \otimes \mathbf{w}_\mu\left(\mu_1\right) \otimes \dot{\mathbf{w}}_\nu\left(\nu_1\right), \ldots, a_{K_c}\mathbf{w}_\lambda\left(\lambda_{K_c}\right) \otimes \mathbf{w}_\mu\left(\mu_{K_c}\right) \otimes \dot{\mathbf{w}}_\nu\left(\nu_{K_c}\right)\right]$$

Herein,

$$\dot{\mathbf{w}}_\lambda (\lambda) = [\dot{W}_\lambda(\Delta_\lambda l_a \ -\lambda), \ldots, \dot{W}_\lambda(\Delta_\lambda l_b \ -\lambda)]^{\mathrm{T}} \tag{2.41}$$

$$\dot{\mathbf{w}}_\mu (\mu) = [\dot{W}_\mu(\Delta_\mu m_a -\mu), \ldots, \dot{W}_\mu(\Delta_\mu m_b -\mu)]^{\mathrm{T}} \tag{2.42}$$

$$\dot{\mathbf{w}}_\nu (\nu) = [\dot{W}_\nu(\Delta_\nu n_a \ -\nu), \ldots, \dot{W}_\nu(\Delta_\nu n_b \ -\nu)]^{\mathrm{T}} \tag{2.43}$$

gather the derivatives of the Fourier-domain window functions evaluated on the frequency grid.

The CRB matrix (2.40) has the following block structure

$$\mathbf{CRB} = \begin{bmatrix} \widetilde{\mathbf{CRB}}_r & * & * & * & * \\ * & \widetilde{\mathbf{CRB}}_i & * & * & * \\ * & * & \widetilde{\mathbf{CRB}}_\lambda & * & * \\ * & * & * & \widetilde{\mathbf{CRB}}_\mu & * \\ * & * & * & * & \widetilde{\mathbf{CRB}}_\nu \end{bmatrix},$$

where $*$ denotes sub matrices of no interest and $\widetilde{\mathbf{CRB}}_r,$, $\widetilde{\mathbf{CRB}}_i,$, $\widetilde{\mathbf{CRB}}_\lambda$, $\widetilde{\mathbf{CRB}}_\mu$, $\widetilde{\mathbf{CRB}}_\nu$, the $K_c \times K_c$ sub matrices associated with the respective cisoid parameter.

Without loss of generality we assume, that the K cisoids parameters of interest are the first elements of $\mathbf{a}_{K_c}, \boldsymbol{\lambda}_{K_c}, \boldsymbol{\mu}_{K_c}, \boldsymbol{\nu}_{K_c}$, respectively. Selecting the upper left $K \times K$ sub blocks yields the sub matrices corresponding to the K cisoids of interest

$$\mathbf{CRB}_r, \quad \mathbf{CRB}_i, \quad \mathbf{CRB}_\lambda, \quad \mathbf{CRB}_\mu, \quad \mathbf{CRB}_\nu. \tag{2.44}$$

The diagonal elements of each matrix represent lower bounds on the error variance of the respective parameter estimates.

3 A framework on multidimensional frequency estimation

In this chapter we propose a framework on multidimensional frequency estimation, where we focus on computational efficiency and high-resolution capability. The framework is most advantageous for a large number of well separated cisoids and only few closely spaced cisoid pairs. For such situations, the periodogram is able to resolve most cisoids and high-resolution processing is only required for a small number of unresolved cisoid pairs.

Section 3.1 states the principle of the proposed framework and introduces necessary notation. Section 3.2 presents the proposed processing sequence in particular decoupled frequency estimation with optimal selection of the so-called resolution dimension. In Section 3.3, periodogram-based frequency estimation based on the single-cisoid model is presented. In particular, correction of estimation errors due to frequency discretization is considered. In Section 3.4.1, decoupled high-resolution frequency estimation for the two-cisoid case is presented. We give an example in Section 3.5 and present simulative results in Section 3.6.

3.1 Preliminaries

Consider the case, where the model in (2.1) comprises

- a large number of well separated cisoids in the complete frequency range and

- a few number of cisoid pairs with separations below the resolution limit of the periodogram.

Practical examples are horizontal multipath scenarios in automotive radar and vertical multipath scenarios in low angle radar tracking, considered in [Hei12, DH07], respectively. For such scenarios, periodogram-based frequency estimation fails for the closely spaced cisoids and it is not possible to predefine a suitable sub-band for NLS-based frequency estimation. Therefore, both conventional approaches for computationally efficient multidimensional frequency estimation can not be used directly.

Here, we propose to apply sub-band frequency estimation locally in the vicinity of periodogram peaks. For each peak, bounded by λ_a, λ_b, μ_a, μ_b, ν_a, ν_b , we consider the Fourier-domain model in (2.4) with either $K = 1$, for well separated cisoids,

$$X\left(\lambda, \mu, \nu\right) = a_0 W_\lambda\left(\lambda - \lambda_0\right) W_\mu\left(\mu - \mu_0\right) W_\nu\left(\nu - \nu_0\right) + \Xi(\lambda, \mu, \nu), \qquad (3.1)$$

$$\{\lambda, \lambda_0\} \in \left(\lambda_a, \lambda_b\right), \quad \{\mu, \mu_0\} \in \left(\mu_a, \mu_b\right), \quad \{\nu, \nu_0\} \in \left(\nu_a, \nu_b\right),$$

or with $K = 2$, for closely spaced cisoid pairs,

$$X\left(\lambda, \mu, \nu\right) = \sum_{k=1}^{2} a_k W_\lambda\left(\lambda - \lambda_k\right) W_\mu\left(\mu - \mu_k\right) W_\nu\left(\nu - \nu_k\right) + \Xi(\lambda, \mu, \nu), \qquad (3.2)$$

$$\{\lambda, \lambda_1, \lambda_2\} \in \left(\lambda_a, \lambda_b\right), \quad \{\mu, \mu_1, \mu_2\} \in \left(\mu_a, \mu_b\right), \quad \{\nu, \nu_1, \nu_2\} \in \left(\nu_a, \nu_b\right).$$

Note that for model (3.2), the frequency separations

$$\delta_\lambda = \lambda_2 - \lambda_1, \quad \delta_\mu = \mu_2 - \mu_1, \quad \delta_\nu = \nu_2 - \nu_1, \qquad (3.3)$$

are below the resolution limits in all three dimensions simultaneously. The models in (3.1) and (3.2) are appropriate as long as window functions with high sidelobe attenuation, such as Chebychev windows [Dol46] are used. In this way, out-of-band cisoids are strongly attenuated compared to the one or two cisoids of interest.

The frequencies of the single-cisoid model λ_0, μ_0, and ν_0, can be straightforwardly obtained by the frequencies of the periodogram peak

$$\hat{\lambda}_0, \hat{\mu}_0, \hat{\nu}_0 = \arg \max_{\lambda, \mu, \nu} P\left(\lambda, \mu, \nu\right), \qquad (3.4)$$

where the maximization is restricted to the peak neighborhood. For the special case $K_c = 1$ and rectangular window functions it represents the classical periodogram maximizer, which is in such a case optimal [SM05]. Another special case is $K_c \gg 1$, rectangular window functions, and well separated cisoids, that is all possible cisoid pairs have a frequency separation above the resolution limit in at least one dimension. In that case, the frequencies of the K_c largest periodogram peaks provide an approximation to the optimal solution if the periodogram is calculated on a DFT frequency grid, with grid sizes equal to the corresponding sample support [SM05]. In practice, window functions with low SLL are required to mitigate mutual interference or leakage. Thereby, the estimation error is increased and a practical trade-off has to be found.

For the two-cisoid model (3.2), the periodogram fails due to its resolution limitation and high-resolution methods, such as the NLS estimator (2.24) for $K = 2$ become necessary

$$\hat{\boldsymbol{\lambda}}_2, \hat{\boldsymbol{\mu}}_2, \hat{\boldsymbol{\nu}}_2 = \arg \max_{\boldsymbol{\lambda}_2, \boldsymbol{\mu}_2, \boldsymbol{\nu}_2} \left\|\mathbf{W}_2\left(\boldsymbol{\lambda}_2, \boldsymbol{\mu}_2, \boldsymbol{\nu}_2\right) \mathbf{W}_2^+\left(\boldsymbol{\lambda}_2, \boldsymbol{\mu}_2, \boldsymbol{\nu}_2\right) \mathbf{x}\right\|^2. \qquad (3.5)$$

However, a direct implementation of (3.5) involves a joint optimization with respect to six parameters, which is computationally demanding.

3.1.1 Decoupled frequency estimation

Optimal multidimensional frequency estimation requires a joint optimization with respect to K frequencies in multiple dimensions. Thus the dimensionality of the optimization problem is given by K times the number of frequency dimensions. A common approach to reduce the computational complexity is to decouple multidimensional frequency estimation into a sequence of 1-D frequency estimation problems, which can achieve almost the same estimation performance [VS98, SS98, Ath01, LHSV95]. When decoupling the multidimensional frequency estimation, one has to decide on the processing sequence. In one dimension, referred to as resolution dimension, a 1-D high-resolution frequency estimation for K cisoids has to be performed first. In the remaining dimensions, the calculated frequency estimates can then be used for signal component extraction, so that the remaining estimation problem is further simplified to K single-cisoid frequency estimation problems.

Existing decoupled methods use a predefined resolution dimension and are based on models in the original domain. Here, we consider a decoupled frequency estimation in the Fourier-domain with optimal selection of the resolution dimension. This can be based on the following vector models

$$\mathbf{z}_\lambda(\mu, \nu) = \sum_{k=1}^{K} \alpha_k(\mu, \nu)\mathbf{w}_\lambda(\lambda_k) + \text{noise}, \tag{3.6}$$

$$\mathbf{z}_\mu(\lambda, \nu) = \sum_{k=1}^{K} \alpha_k(\lambda, \nu)\mathbf{w}_\mu(\mu_k) + \text{noise}, \tag{3.7}$$

$$\mathbf{z}_\nu(\lambda, \mu) = \sum_{k=1}^{K} \alpha_k(\lambda, \mu)\mathbf{w}_\nu(\nu_k) + \text{noise}, \tag{3.8}$$

where $\mathbf{w}_\lambda(\lambda)$, $\mathbf{w}_\mu(\mu)$, $\mathbf{w}_\nu(\nu)$ are given in (2.18), (2.19), (2.20), respectively, and

$$\alpha_k(\mu, \nu) = a_k W_\mu(\mu - \mu_k) W_\nu(\nu - \nu_k), \tag{3.9}$$

$$\alpha_k(\lambda, \nu) = a_k W_\lambda(\lambda - \lambda_k) W_\nu(\nu - \nu_k), \tag{3.10}$$

$$\alpha_k(\lambda, \mu) = a_k W_\lambda(\lambda - \lambda_k) W_\mu(\mu - \mu_k). \tag{3.11}$$

Note that models (3.6), (3.7), and (3.8) are used when the resolution dimension is the first, second, or third dimension, respectively.

If we use $K = 1$ or $K = 2$ in (3.6), (3.7), (3.8), and let $\lambda \in (\lambda_a, \lambda_b)$, $\mu \in (\mu_a, \mu_b)$, $\nu \in (\nu_a, \nu_b)$, local decoupled models for the single-cisoid or the two-cisoid case are obtained.

3.2 Processing sequence

Here we present a processing sequence, which is applied for each significant peak of the periodogram and distinguishes between the local single-cisoid model and the local two-cisoid model. For the single-cisoid model, computationally simple periodogram-based frequency estimation, discussed in Section 3.3, is used, whereas for the two-cisoid model, decoupled high-resolution frequency estimation, as discussed in Section 3.4, is used. In Section 3.2.1, we propose a method to determine the best resolution dimension for the decoupled frequency estimation adaptively. In Section 3.2.2 we discuss how the decision between the local single-cisoid and two-cisoid models can be achieved by using local decoupled models.

3.2.1 Selection of the resolution dimension

The overall success of decoupled frequency estimation depends critically on resolved estimates in the resolution dimension. It is well known that the resolution success of 1-D high-resolution frequency estimation depends on the available signal-to-noise ratio (SNR) and particularly on the frequency separation [vT02]. Therefore, the correct selection of the resolution dimension is crucial for the decoupled approach, where the best results are achieved when it is selected according to the largest frequency separation. For this purpose, we propose to calculate the mean squared errors (MSE) of the single-cisoid model fit for each dimension

$$\text{MSE}_{1,\lambda} = \frac{1}{L}\,\|\mathbf{z}_\lambda(\mu,\nu) - \hat{\alpha}_0(\mu,\nu)\mathbf{w}_\lambda(\hat{\lambda}_0)\|^2, \tag{3.12}$$

$$\text{MSE}_{1,\mu} = \frac{1}{M}\|\mathbf{z}_\mu(\lambda,\nu) - \hat{\alpha}_0(\lambda,\nu)\mathbf{w}_\mu(\hat{\mu}_0)\|^2, \tag{3.13}$$

$$\text{MSE}_{1,\nu} = \frac{1}{N}\,\|\mathbf{z}_\nu(\lambda,\mu) - \hat{\alpha}_0(\lambda,\mu)\mathbf{w}_\nu(\hat{\nu}_0)\|^2. \tag{3.14}$$

Herein, $\hat{\lambda}_1$, $\hat{\mu}_1$, and $\hat{\nu}_1$ are obtained according to (3.4) and

$$\hat{\alpha}_0(\mu,\nu) = \mathbf{w}_\lambda^+(\hat{\lambda}_0)\,\mathbf{z}_\lambda(\mu,\nu) \tag{3.15}$$

$$\hat{\alpha}_0(\lambda,\nu) = \mathbf{w}_\mu^+(\hat{\mu}_0)\,\mathbf{z}_\mu(\lambda,\nu) \tag{3.16}$$

$$\hat{\alpha}_0(\lambda,\mu) = \mathbf{w}_\nu^+(\hat{\nu}_0)\,\mathbf{z}_\nu(\lambda,\mu) \tag{3.17}$$

are the LS estimates of the corresponding amplitude terms. The resolution dimension is now selected according to the largest value among (3.12), (3.13), and (3.14).

To motivate that approach, consider a two-cisoid model with no frequency separation in one of the three dimensions, e.g. the last dimension of (2.4). The corresponding decoupled model (3.8)

$$\mathbf{z}_\nu(\lambda,\mu) = [\alpha_1(\lambda,\mu) + \alpha_2(\lambda,\mu)]\mathbf{w}_\nu(\nu_1) + \text{noise},$$

is then an effective single-cisoid model. The corresponding MSE_ν will be on the order of the noise power and thus small. The same holds for small but non-zero frequency separations. The practicality of the MSE-based approach is demonstrated in Section 3.6.1 by simulations.

3.2.2 Model selection

The optimal solution to decide between the single-cisoid and the two-cisoid model is the generalized likelihood ratio test (GLRT). Here, the test statistic is given by the ratio of the respective likelihood functions, which have been maximized with respect to the unknown model parameters. In a simplified version of the GLRT, a decision for the two-cisoid model is made if

$$\frac{\text{MSE}_1}{\text{MSE}_2} > \gamma_2 \tag{3.18}$$

where MSE_1 and MSE_2 are the mean square fitting errors of the single-cisoid and two-cisoid model in the resolution dimension, respectively. That is, MSE_1 is given by either (3.12), (3.13), or (3.14) and MSE_2 is given by one of

$$\text{MSE}_{2,\lambda} = \frac{1}{L} \left\| \mathbf{z}_\lambda(\mu,\nu) - \hat{\alpha}_1(\mu,\nu)\mathbf{w}_\lambda(\hat{\lambda}_1) - \hat{\alpha}_2(\mu,\nu)\mathbf{w}_\lambda(\hat{\lambda}_2) \right\|^2, \tag{3.19}$$

$$\text{MSE}_{2,\mu} = \frac{1}{M} \left\| \mathbf{z}_\mu(\lambda,\nu) - \hat{\alpha}_1(\lambda,\nu)\mathbf{w}_\mu(\hat{\mu}_1) - \hat{\alpha}_2(\lambda,\nu)\mathbf{w}_\mu(\hat{\mu}_2) \right\|^2, \tag{3.20}$$

$$\text{MSE}_{2,\nu} = \frac{1}{N} \left\| \mathbf{z}_\nu(\lambda,\mu) - \hat{\alpha}_1(\lambda,\mu)\mathbf{w}_\nu(\hat{\nu}_1) - \hat{\alpha}_2(\lambda,\mu)\mathbf{w}_\nu(\hat{\nu}_2) \right\|^2. \tag{3.21}$$

Herein, $\hat{\lambda}_1$, $\hat{\lambda}_2$, $\hat{\mu}_1$, $\hat{\mu}_2$, $\hat{\nu}_1$, $\hat{\nu}_2$ are maximum likelihood estimates obtained for the two-cisoid model, and

$$\left[\hat{\alpha}_1(\mu,\nu), \hat{\alpha}_2(\mu,\nu)\right]^{\text{T}} = \left[\mathbf{w}_\lambda(\hat{\lambda}_1), \mathbf{w}_\lambda(\hat{\lambda}_2)\right]^+ \mathbf{z}_\lambda(\mu,\nu), \tag{3.22}$$

$$\left[\hat{\alpha}_1(\lambda,\nu), \hat{\alpha}_2(\lambda,\nu)\right]^{\text{T}} = \left[\mathbf{w}_\mu(\hat{\mu}_1), \mathbf{w}_\mu(\hat{\mu}_2)\right]^+ \mathbf{z}_\mu(\lambda,\nu), \tag{3.23}$$

$$\left[\hat{\alpha}_1(\lambda,\mu), \hat{\alpha}_2(\lambda,\mu)\right]^{\text{T}} = \left[\mathbf{w}_\nu(\hat{\nu}_1), \mathbf{w}_\nu(\hat{\nu}_2)\right]^+ \mathbf{z}_\nu(\lambda,\mu), \tag{3.24}$$

are the corresponding amplitude estimates. The threshold γ_2 can be obtained empirically by fixing the false-alarm rate to a desired level, where false alarm refers to erroneously deciding for the two-cisoid model when only a single-cisoid is present.

Calculating the GLRT test statistic requires the estimation of the two-cisoid model parameters, which is computationally intensive even for the efficient decoupled approach described in Section 3.4. Therefore it should only be performed, when the single-cisoid model is unlikely and a two-cisoid is indicated. This indication can be based on a goodness-of-fit test of the single-cisoid model [Hei12], which is here performed in the selected resolution dimesion

$$\text{MSE}_1 > \gamma_1.$$

The threshold γ_1 depends on the noise power and the sample support in the resolution dimension. It can be obtained empirically with the help of simulations.
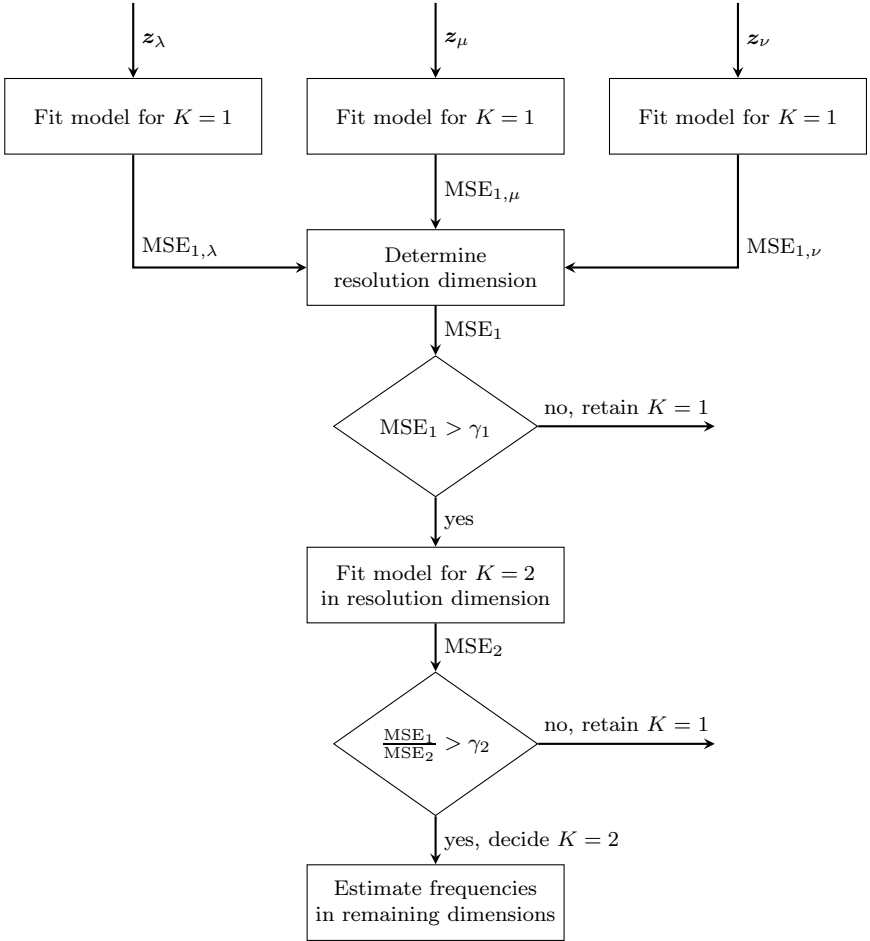
Figure 3.1: Processing sequence with optimal selection of the resolution dimension.

3.2.3 Overview

Figure 3.1 gives an overview of the proposed processing sequence for multidimensional decoupled high-resolution frequency estimation. The shown processing steps are performed for each peak of the periodogram and the decoupled models in (3.6), (3.7), and (3.8) are defined locally in the vicinity of each peak. The frequencies of the single-cisoid and the two-cisoid model, required for calculating the corresponding MSE values, are obtained as described in Section 3.3 and Section 3.4, respectively.

3.3 Single-cisoid frequency estimation

The accuracy of periodogram-based frequency estimation according to (3.4) is determined by the step-size of the employed frequency grid. Fine step-sizes are often not practical due to memory and processing power restrictions. Therefore we propose a computational efficient implementation of (3.4), which achieves sub-grid accuracy.

To this end, consider

$$\Delta_\lambda l_0, \ \Delta_\mu m_0, \ \Delta_\nu n_0, \quad l_0, m_0, n_0 = \arg \max_{l,m,n} P\left(l, m, n\right), \tag{3.25}$$

with predefined frequency step-sizes Δ_λ, Δ_μ, Δ_ν. The finite step-sizes introduce a bias

$$\beta_\lambda = \Delta_\lambda l_0 - \hat{\lambda}_1, \quad \beta_\mu = \Delta_\mu m_0 - \hat{\mu}_1, \quad \beta_\nu = \Delta_\nu n_0 - \hat{\nu}_1, \tag{3.26}$$

in the range of $(-\Delta_\lambda/2, \Delta_\lambda/2)$, $(-\Delta_\mu/2, \Delta_\mu/2)$, $(-\Delta_\nu/2, \Delta_\nu/2)$, respectively. The maximal bias values correspond to the cases where the true frequencies lie exactly in the middle of two adjacent grid values and the bias terms vanish if the true frequencies coincide with a grid value. There exists a wealth of method for reducing the grid induced bias terms in (3.26) [RV70, Gra83, Qui94, Qui97, Mac98, Can13]. However all of those methods restrict either the frequency grid step size or the choice of window functions. Only the parabolic interpolation approach in [Ric14, Sec. 5.3.4] is applicable for arbitrary step sizes and window functions. However, the remaining bias after correction is large compared to the CRB, which we show in Section 3.6.2 by simulations.

3.3.1 Proposed approach

We propose a new periodogram-based frequency estimator for the single-cisoid model, which corrects the frequency-grid induced bias (3.26) for arbitrary window functions and grid-sizes. We begin with a derivation for the first frequency dimension and extent the result to the remaining dimensions afterwards.

Consider the logarithmic ratio of the DFT-grid periodogram maximizer and the larger one of the adjacent values

$$R_\lambda = \log \frac{P\left(l_0, m_0, n_0\right)}{\max\left\{P\left(l_0 - 1, m_0, n_0\right), P\left(l_0 + 1, m_0, n_0\right)\right\}}. \tag{3.27}$$

Note that (3.27) is a bounded function of the bias $R_\lambda = f(\beta_\lambda)$ in the domain $(-\Delta_\lambda/2, \Delta_\lambda/2)$. The inverse function $f^{-1}(R_\lambda)$ yields the absolute bias for a given R_λ. If we consider that the true cisoid frequency lies between the grid point of the

maximal periodogram value and its largest neighboring value, the following approach could be used to obtain the bias

$$\beta_\lambda = \begin{cases} +f^{-1}(R_\lambda), & P\left(l_0, m_0, n_0 + 1\right) > P\left(l_0, m_0, n_0 - 1\right) \\ -f^{-1}(R_\lambda), & P\left(l_0, m_0, n_0 + 1\right) < P\left(l_0, m_0, n_0 - 1\right) \end{cases}.$$

However, the function $f^{-1}(R_\lambda)$ appears hard to obtain analytically for common window functions and therefore we propose a method for constructing a look-up table (LUT) for it.

To this end, consider the noiseless 1-D single-cisoid model with a predefined frequency λ_0, which we vary within half of the frequency step size $\Delta_\lambda l_0 + u\Delta_\lambda/(2U)$, $u = 0, \ldots, U - 1$, where U is a predefined LUT size. The corresponding DFT-grid periodogram maximizer is l_0 for all u and the continuous periodogram maximizer is λ_0. This yields bias values $\beta_\lambda = u\Delta_\lambda/(2U)$, for which the corresponding periodogram ratio as in (3.27) can be calculated. More precisely, the maximal DFT-grid periodogram value at l_0 and the largest neighboring value at $l_0 + 1$ can be calculated. Taking the logarithm and forming the ratio, yields

$$R_\lambda\left(u\right) = \log \left| \sum_{l_s=0}^{L_s-1} w_\lambda(l_s) \, e^{j\frac{\Delta_\lambda}{2U}l_s u} \right|^2 - \log \left| \sum_{l_s=0}^{L_s-1} w_\lambda(l_s) \, e^{j\frac{\Delta_\lambda}{2U}l_s u} e^{-j\Delta_\lambda l_s} \right|^2.$$

In this way, pairs of bias $u\Delta_\lambda/(2U)$ and periodogram ratio values $R_\lambda(u)$ are obtained. To use these pairs as a LUT, a regular grid of periodogram ratio values $R_\lambda = 0, \Delta_{R,\lambda}, \ldots, (U-1)\Delta_{R,\lambda}$ is required, where $\Delta_{R,\lambda} = \max R_\lambda(u)/(U-1)$. Thereby, the LUT index for a given value of R_λ can be obtained by simply dividing with the step length $\Delta_{R,\lambda}$ and rounding to the nearest integer value. To obtain such a regular grid the corresponding bias values can be linearly interpolated. Gathering these values yields the desired LUT

$$\text{LUT}_\lambda(u) = \frac{\Delta_\lambda}{2U} \left[\tilde{u} + \frac{\Delta_{R,\lambda} \, u - R_\lambda\left(\tilde{u}\right)}{R_\lambda\left(\tilde{u} + 1\right) - R_\lambda\left(\tilde{u}\right)} \right], \quad \tilde{u} = \arg\min_k \left\{ \Delta_{R,\lambda}u - R_\lambda(k) \right\}. \ (3.28)$$

Note that (3.28) is calculated off-line and stored. This enables the following bias corrected estimator

$$\hat{\lambda}_1 = \begin{cases} \Delta_\lambda \, l_0 + \text{LUT}_\lambda\left(\lfloor R_\lambda/\Delta_{R,\lambda}\rceil\right), & P\left(l_0 + 1, m_0, n_0\right) > P\left(l_0 - 1, m_0, n_0\right) \\ \Delta_\lambda \, l_0 - \text{LUT}_\lambda\left(\lfloor R_\lambda/\Delta_{R,\lambda}\rceil\right), & P\left(l_0 + 1, m_0, n_0\right) < P\left(l_0 - 1, m_0, n_0\right) \end{cases}. \ (3.29)$$

Note that (3.29) can be further refined by linear interpolation to compensate for potentially small LUT sizes.

The same approach is straightforwardly extended to the remaining dimensions. The respective LUTs are

$$\text{LUT}_\mu(u) = \frac{\Delta_\mu}{2U} \left[\tilde{u} + \frac{\Delta_{R,\mu} \, u - R_\mu\left(\tilde{u}\right)}{R_\mu\left(\tilde{u} + 1\right) - R_\mu\left(\tilde{u}\right)} \right], \tilde{u} = \arg\min_k \left\{ \Delta_{R,\mu}u - R_\mu(k) \right\}, \quad (3.30)$$

$$\text{LUT}_\nu(u) = \frac{\Delta_\nu}{2U} \left[\tilde{u} + \frac{\Delta_{R,\nu} \, u - R_\nu\left(\tilde{u}\right)}{R_\nu\left(\tilde{u} + 1\right) - R_\nu\left(\tilde{u}\right)} \right], \tilde{u} = \arg\min_k \left\{ \Delta_{R,\nu}u - R_\nu(k) \right\}. \quad (3.31)$$

Herein, $\Delta_{R,\mu} = \max R_\mu(u)/(U-1)$, $\Delta_{R,\nu} = \max R_\nu(u)/(U-1)$,

$$R_\mu(u) = \log\left|\sum_{m_s=0}^{M_s-1} w_\mu(m_s)\, e^{j\frac{\Delta_\mu}{2U}m_s u}\right|^2 - \log\left|\sum_{m_s=0}^{M_s-1} w_\mu(m_s)\, e^{j\frac{\Delta_\mu}{2U}m_s u} e^{-j\Delta_\mu m_s}\right|^2,$$

$$R_\nu(u) = \log\left|\sum_{n_s=0}^{N_s-1} w_\nu(n_s)\, e^{j\frac{\Delta_\nu}{2U}n_s u}\right|^2 - \log\left|\sum_{n_s=0}^{N_s-1} w_\nu(n_s)\, e^{j\frac{\Delta_\nu}{2U}n_s u} e^{-j\Delta_\nu n_s}\right|^2.$$

The bias corrected single-cisoid estimators are then

$$\hat{\mu}_1 = \begin{cases} \Delta_\mu\, m_0 + \mathrm{LUT}_\mu\left(\lfloor R_\mu/\Delta_{R,\mu}\rfloor\right), & P(l_0, m_0+1, n_0) > P(l_0, m_0-1, n_0) \\ \Delta_\mu\, m_0 - \mathrm{LUT}_\mu\left(\lfloor R_\mu/\Delta_{R,\mu}\rfloor\right), & P(l_0, m_0+1, n_0) < P(l_0, m_0-1, n_0) \end{cases}, (3.32)$$

$$\hat{\nu}_1 = \begin{cases} \Delta_\nu\, n_0 + \mathrm{LUT}_\nu\left(\lfloor R_\nu/\Delta_{R,\nu}\rfloor\right), & P(l_0, m_0, n_0+1) > P(l_0, m_0, n_0-1) \\ \Delta_\nu\, n_0 - \mathrm{LUT}_\nu\left(\lfloor R_\nu/\Delta_{R,\nu}\rfloor\right), & P(l_0, m_0, n_0+1) < P(l_0, m_0, n_0-1) \end{cases}, (3.33)$$

where

$$R_\mu = \log \frac{P(l_0, m_0, n_0)}{\max\{P(l_0, m_0-1, n_0), P(l_0, m_0+1, n_0)\}},$$

$$R_\nu = \log \frac{P(l_0, m_0, n_0)}{\max\{P(l_0, m_0, n_0-1), P(l_0, m_0, n_0+1)\}}.$$

With (3.29), (3.32), and (3.33), the frequencies of a single-cisoid model can be obtained with high accuracy based on only three local periodogram values per dimension. Compared to existing methods the frequency grid size as well as the window functions can be chosen arbitrarily. The proposed method is computationally most simple: it requires only the ratio of the periodogram peak value and its larger neighbor to obtain the corresponding bias in a pre-calculated LUT.

3.4 Decoupled two-cisoid frequency estimation

Here, decoupled high-resolution frequency estimation for the local two-cisoid model is discussed. Section 3.4.1 presents 1-D high-resolution frequency estimation based on the local Fourier-domain model in the resolution dimension, given by one of the models in (3.6), (3.7), or (3.8) for $K = 2$. Section 3.4.2 considers frequency estimation in the remaining dimension based on the resolution dimension estimates. To simplify the notation we restrict the discussion to the case, where the first frequency dimension is the resolution dimension. The corresponding local model in (3.6) is for $K = 2$ given by

$$\mathbf{z}_\lambda(\mu, \nu) = \underbrace{[\mathbf{w}_\lambda(\lambda_1), \mathbf{w}_\lambda(\lambda_2)]}_{\mathbf{W}(\lambda_1, \lambda_2)}[\alpha_1(\mu, \nu), \alpha_2(\mu, \nu)]^{\mathrm{T}} + \text{noise}. \tag{3.34}$$

For notational convenience we let $\mathbf{z}_\lambda(m, n)$ and $\alpha_k(m, n)$ denote (3.34) and (3.9) evaluated on a frequency grid with step sizes Δ_μ and Δ_ν, respectively.

3.4.1 Resolution dimension

Here, we discuss how the frequencies in the resolution dimension λ_1 and λ_2 can be obtained by 1-D high-resolution methods. For a practical implementation, a frequency discretization in all dimension is given and thus a set of local vector models $\mathbf{z}_\lambda(m, n)$ has to be considered, where m and n are restricted to the peak neighborhood.

We present two pre-processing steps for applying 1-D high-resolution methods. The first uses only the vector corresponding to the largest periodogram peak. The second averages over all data vectors $\mathbf{z}_\lambda(m, n)$ in the vicinity of the peak. Both approaches can be treated uniformly by introducing

$$\hat{\mathbf{R}} = \begin{cases} \mathbf{z}_\lambda(m_0, n_0)\, \mathbf{z}_\lambda^{\mathrm{H}}(m_0, n_0), & \text{Pre-processing 1,} \\[2mm] \dfrac{1}{MN} \displaystyle\sum_{m=0}^{M-1} \sum_{n=0}^{N-1} \mathbf{z}_\lambda(m, n)\, \mathbf{z}_\lambda^{\mathrm{H}}(m, n), & \text{Pre-processing 2} \end{cases} \tag{3.35}$$

where m_0 and n_0 are the peak indices. Note that (3.35) constitutes an estimate of the so called data covariance matrix, which plays an important role in subspace based frequency estimation as its eigenstructure contains complete information on the cisoid frequencies [SM05]. We refrain from discussing (3.35) further and use it only for notational convenience.

3.4.1.1 Sub-band frequency estimation

In principle, any 1-D high-resolution method can be used to estimate the cisoid frequencies in the resolution dimension, as long as it is applicable in the Fourier domain and allows for frequency band limitation. Thus either so called frequency selective approaches such as in [TN88, SSSL04, MV01] can be used or beamspace array processing methods can be employed, which are equivalent to 1-D Fourier-domain frequency estimation for uniform linear arrays (ULA) [SM05]. Methods applicable for ULAs include beamspace maximum likelihood [ZL91b, Zol88], beamspace multiple signal classification (BS-MUSIC) [SA91], the beamspace root MUSIC technique [ZKS93], or the beamspace version of estimation of signal parameters via rotational invariance techniques (BS-ESPRIT) [ZHM96].

All of the array processing methods require an orthonormal beamspace transformation [WF94]. To see how this applies to the decoupled Fourier-domain model (3.34), write

$$\mathbf{z}_\lambda(m, n) = (\mathbf{W}_s \mathbf{F})^{\mathrm{H}} \underbrace{\left\{ [\mathbf{v}(\lambda_1), \mathbf{v}(\lambda_2)][\alpha_1(m, n), \alpha_2(m, n)]^{\mathrm{T}} + \text{noise} \right\}}_{\text{original-domain model}} \tag{3.36}$$

where $\mathbf{v}(\lambda) = [1, e^{j\lambda}, \ldots, e^{j\lambda(L_s-1)}]^T$ and the elements of $\mathbf{F} \in \mathbb{C}^{L_s \times L}$, $\mathbf{W}_s \in \mathbb{R}^{L_s \times L_s}$, are given by

$$[\mathbf{F}]_{l_s,l} = e^{j\Delta_\lambda(l_a+l)l_s}, \quad [\mathbf{W}_s]_{l,m} = \begin{cases} w_\lambda(l) & l = m \\ 0 & l \neq m \end{cases}.$$

Herein, $\mathbf{W}_s\mathbf{F}$ is equivalent to a beamspace transformation, which is applied to a decoupled model in the original domain. That transformation is orthonormal only if

$$L_{\mathrm{DFT}} = L_s \quad \text{and} \quad w_\lambda(l) = \sqrt{L_s}, \quad l = 0, \ldots, L_s - 1.$$

The DFT grid constraint is usually acceptable in practice as $L_{\mathrm{DFT}} = L_s$ is in many practical applications enforced by limited processing and memory resources. In contrast, the scaled rectangular window is not acceptable due to its high SLL and thus weak out-of-band interference suppression. To apply the above methods for other than the rectangular window we can apply orthonormalization [vT02]

$$\mathbf{z}_o(m,n) = \left[(\mathbf{F}^H\mathbf{W}_s^H\mathbf{W}_s\mathbf{F})^{-\frac{1}{2}}\right]^H \mathbf{z}_\lambda(m,n). \tag{3.37}$$

The downside of using (3.37) is an increased SLL in the Fourier-domain window functions [vT02] and as a consequence a degraded out-of-band interference suppression. In particular subspace based methods such as BS-MUSIC and BS-ESPRIT deteriorate due to out-of-band interference since they critically depend on a white noise assumption.

Subspace based methods as well as the method proposed in [ZL91b] require multiple data snapshots of non-coherent sources. If we still want to apply subspace based methods for our data model, pre processing such as spatial smoothing becomes necessary [SWK85]. For NLS, the white noise assumption assumption is not crucial [SJL97]. Furthermore it is directly applicable to our model without the need of additional pre processing such as the equivalent of spatial smoothing. Thus we propose a direct calculation of the NLS criterion function on a coarse frequency grid, which is followed by a Gauss-Newton-type method to refine the estimates.

Before discussing the proposed approach, we comment on the identifiability of the two cisoid Fourier-domain problem, which impacts the minimal size of the frequency sub-band. To uniquely identify two cisoids from $\mathbf{z}_\lambda(m,n)$

$$L + \underbrace{\mathrm{rank}\{\mathbf{W}(\lambda_1, \lambda_2)\}}_{=2} > 4 \quad \Rightarrow \quad L > 2$$

has to hold [WZ89]. Thus we require that at least three DFT frequencies lie in the sub-band of interest. To see that $\mathbf{W}(\lambda_1, \lambda_2)$ has full rank 2 we write

$$\mathbf{W}(\lambda_1, \lambda_2) = \left(\mathbf{W}_s\mathbf{F}\right)^H[\mathbf{v}(\lambda_1), \mathbf{v}(\lambda_2)]$$

as in (3.36). Both $\mathbf{F}$ and $[\mathbf{v}(\lambda_1), \mathbf{v}(\lambda_2)]$ are Vandermond matrices and thus of rank L and 2 respectively. The rank of $\mathbf{W}_s$ is L_s since it is square and diagonal. By employing $\mathrm{rank}(\mathbf{XY}) = \min\{\mathrm{rank}(\mathbf{X}), \mathrm{rank}(\mathbf{Y})\}$ twice the proposition follows.

3.4.1.2 Proposed approach

We propose a two step NLS-based frequency estimation in the resolution dimension. Here, the NLS criterion function is maximized on a coarse frequency grid first. In a second step, the coarse-grid estimates are refined using the Gauss Newton type method proposed by Viberg et al. [VOK91], which is adapted to the decoupled Fourier-domain model.

Coarse grid nonlinear least squares

We consider a direct evaluation of the NLS criterion function in the resolution dimension. The derivation of the 1-D NLS method is equivalent to the derivation in Section 2.2.1 for the 3-D case. The only difference is how the remaining dimensions are incorporated. To this end, consider two approaches, which lead to the following NLS criterion function

$$
c(\lambda_1, \lambda_2) = \begin{cases} \left\| \mathbf{P}(\lambda_1, \lambda_2)\, \mathbf{z}_\lambda\,(m_0, n_0) \right\|^2, & \text{Pre-processing 1} \\ \dfrac{1}{MN} \sum_{m=0}^{M-1} \sum_{n=0}^{N-1} \left\| \mathbf{P}(\lambda_1, \lambda_2)\, \mathbf{z}_\lambda\,(m, n) \right\|^2, & \text{Pre-processing 2} \end{cases}
$$
$$
= \mathrm{Tr}\{\mathbf{P}(\lambda_1, \lambda_2)\,\hat{\mathbf{R}}\}, \tag{3.38}
$$

where $\mathbf{P}(\lambda_1, \lambda_2) = \mathbf{W}(\lambda_1, \lambda_2)\mathbf{W}^+(\lambda_1, \lambda_2)$ and $\mathrm{Tr}\{\cdot\}$ denotes the trace operator. We evaluate criterion function (3.38) on a few grid points around the peak frequencies

$$
\Delta_{\lambda,\mathrm{NLS}} = \frac{2\pi}{L_{\mathrm{NLS}}}, \quad \left\{ \Delta_{\lambda,\mathrm{NLS}}\, l \,\middle|\, l = l_{a,\mathrm{NLS}}, \ldots, l_{b,\mathrm{NLS}} \right\},
$$

where $l_{a,\mathrm{NLS}} = \lceil \lambda_a / \Delta_{\lambda,\mathrm{NLS}} \rceil$ and $l_{b,\mathrm{NLS}} = \lfloor \lambda_b / \Delta_{\lambda,\mathrm{NLS}} \rfloor$. This yields the coarse-grid NLS estimates

$$
\hat{\lambda}_{c,1} = \Delta_{\lambda,\mathrm{NLS}}\, l_{c,1}, \;\; \hat{\lambda}_{c,2} = \Delta_{\lambda,\mathrm{NLS}}\, l_{c,2},
$$
$$
l_{c,1},\, l_{c,2} = \arg \max_{l_1, l_2} c(l_1, l_2), \quad l_1, l_2 = l_{a,\mathrm{NLS}}, \ldots, l_{b,\mathrm{NLS}},
$$

where $c(l_1, l_2)$ is the criterion function (3.38) evaluated at the grid frequencies represented by l_1 and l_2. The choice of the frequency step size determines the computational cost of evaluating (3.38), which is of order $O[(l_{b,\mathrm{NLS}} - l_{a,\mathrm{NLS}} + 1)^2 L^2]$.

Gauss Newton method

The coarse-grid NLS frequency estimates can be used as initial estimate for Gauss-Newton-type iterations, which have been proposed in [VOK91] for the array processing problem. The technique can be straightforwardly adapted to the Fourier-domain model. One iteration is

$$
\left[\hat{\lambda}_1^{(j+1)}, \hat{\lambda}_2^{(j+1)}\right]^{\mathrm{T}} = \left[\hat{\lambda}_1^{(j)}, \hat{\lambda}_2^{(j)}\right]^{\mathrm{T}} - \mathbf{H}^{-1}\!\left(\hat{\lambda}_1^{(j)}, \hat{\lambda}_2^{(j)}\right)\mathbf{g}\!\left(\hat{\lambda}_1^{(j)}, \hat{\lambda}_2^{(j)}\right), \tag{3.39}
$$

where $\hat{\lambda}_1^{(j)}$ and $\hat{\lambda}_2^{(j)}$ denote the estimates in iteration j,

$$\mathbf{g}(\lambda_1, \lambda_2) = -2\mathrm{Re}\Big\{\mathrm{diag}\big\{\mathbf{W}^+(\lambda_1, \lambda_2)\,\hat{\mathbf{R}}\,\mathbf{P}_\perp(\lambda_1, \lambda_2)\dot{\mathbf{W}}(\lambda_1, \lambda_2)\big\}\Big\}$$

$$\mathbf{H}(\lambda_1, \lambda_2) =$$
$$2\mathrm{Re}\left\{\left[\dot{\mathbf{W}}^{\mathrm{H}}(\lambda_1, \lambda_2)\,\mathbf{P}_\perp(\lambda_1, \lambda_2)\dot{\mathbf{W}}(\lambda_1, \lambda_2)\right] \odot \left[\mathbf{W}^+(\lambda_1, \lambda_2)\,\hat{\mathbf{R}}\left(\mathbf{W}^+(\lambda_1, \lambda_2)\right)^{\mathrm{H}}\right]^{\mathrm{T}}\right\}$$

denote the gradient and the approximate Hessian matrix of (3.38), respectively,

$$\mathbf{P}_\perp(\lambda_1, \lambda_2) = \mathbf{I} - \mathbf{P}(\lambda_1, \lambda_2), \quad \dot{\mathbf{W}}(\lambda_1, \lambda_2) = [\dot{\mathbf{w}}_\lambda(\lambda_1), \dot{\mathbf{w}}_\lambda(\lambda_2)].$$

and $\odot$ denotes the elementwise matrix product. The iterations are initialized with the coarse grid estimates, that is $\hat{\lambda}_1^{(0)} = \hat{\lambda}_{c,1}$ and $\hat{\lambda}_2^{(0)} = \hat{\lambda}_{c,2}$.

Note that typically only a few iterations are required to reach a sufficient accuracy. Thus the maximal number of iterations can be limited to ensure computational efficiency. The computational cost of each iteration is of order $O(KL^2)$ [VOK91].

3.4.2 Remaining dimensions

The frequencies in the remaining dimensions can be estimated by exploiting the structure of $\alpha_1(\mu, \nu)$ and $\alpha_2(\mu, \nu)$, given in (3.9). Considering the model in (3.6) with known λ_1 and λ_2, estimates for $\alpha_1(\mu, \nu)$ and $\alpha_2(\mu, \nu)$, can be obtained using a linear least squares approach. By substituting estimates $\hat{\lambda}_1$ and $\hat{\lambda}_2$, we obtain (3.22), restated here for reference,

$$\left[\hat{\alpha}_1(\mu, \nu), \hat{\alpha}_2(\mu, \nu)\right]^{\mathrm{T}} = \mathbf{W}^+(\hat{\lambda}_1, \hat{\lambda}_2)\,\mathbf{z}_\lambda(\mu, \nu)$$

which is in turn used to estimate the frequencies in the remaining dimensions. In two NLS optimizations for $K = 1$,

$$\hat{\mu}_1, \hat{\nu}_1 = \arg\max_{\mu, \nu} |\alpha_1(\mu, \nu)|^2, \tag{3.40}$$

$$\hat{\mu}_2, \hat{\nu}_2 = \arg\max_{\mu, \nu} |\alpha_2(\mu, \nu)|^2, \tag{3.41}$$

estimates for $\hat{\mu}_1$, $\hat{\nu}_1$, $\hat{\mu}_2$, and $\hat{\nu}_2$ are obtained. Given $\hat{\lambda}_1$ and $\hat{\lambda}_2$ are sufficiently close to the respective true values, the calculated frequency estimates for the remaining dimensions approximate the maximum likelihood estimates [Ath01].

For a practical implementation, (3.22) is calculated on a frequency grid and (3.40) and (3.41) can be obtained via the LUT table approach proposed in Section 3.3

$$
\hat{\mu}_k = \begin{cases} \Delta_\mu m_k + \mathrm{LUT}_\mu \left(\lfloor R_{\mu,k}/\Delta_{R,\mu} \rfloor\right), & |\alpha_k(m_k+1,n_k)|^2 > |\alpha_k(m_k-1,n_k)|^2 \\ \Delta_\mu m_k - \mathrm{LUT}_\mu \left(\lfloor R_{\mu,k}/\Delta_{R,\mu} \rfloor\right), & |\alpha_k(m_k+1,n_k)|^2 < |\alpha_k(m_k-1,n_k)|^2 \end{cases}
$$
(3.42)

$$
\hat{\nu}_k = \begin{cases} \Delta_\nu n_k + \mathrm{LUT}_\nu \left(\lfloor R_{\nu,k}/\Delta_{R,\nu} \rfloor\right), & |\alpha_k(m_k,n_k+1)|^2 > |\alpha_k(m_k,n_k-1)|^2 \\ \Delta_\nu n_k - \mathrm{LUT}_\nu \left(\lfloor R_{\nu,k}/\Delta_{R,\nu} \rfloor\right), & |\alpha_k(m_k,n_k+1)|^2 < |\alpha_k(m_k,n_k-1)|^2 \end{cases}
$$
(3.43)

Herein, $m_k, n_k = \arg \max\limits_{m,n} |\alpha_k(m,n)|^2$ are the maximizing grid indices and

$$
R_{\mu,k} = \log \frac{|\alpha_k(m_k,n_k)|^2}{\max\left\{|\alpha_k(m_k-1,n_k)|^2, |\alpha_k(m_k+1,n_k)|^2\right\}},
$$
$$
R_{\nu,k} = \log \frac{|\alpha_k(m_k,n_k)|^2}{\max\left\{|\alpha_k(m_k,n_k-1)|^2, |\alpha_k(m_k,n_k+1)|^2\right\}}.
$$

Note that the computational cost of the remaining dimension frequency estimator is negligible compared to the NLS estimator in the resolution dimension.

3.5 Example

We consider an example for two cisoids with parameters

$$
a_1 = e^{j5.3}, \quad \lambda_1 = \pi - 0.5\delta_\lambda, \quad \mu_1 = \pi - 0.5\delta_\mu, \quad \nu_1 = \pi - 0.5\delta_\nu,
$$
$$
a_2 = e^{j0.66}, \quad \lambda_2 = \pi + 0.5\delta_\lambda, \quad \mu_2 = \pi + 0.5\delta_\mu, \quad \nu_2 = \pi + 0.5\delta_\nu,
$$

with frequency separations $\delta_\lambda = 0.5\,F_\lambda, \delta_\mu = 0.3\,F_\mu$, $\delta_\nu = 0.3\,F_\nu$ and signal-to-noise-ratios $\mathrm{SNR}_1 = \mathrm{SNR}_2 = 0\,\mathrm{dB}$, where

$$
\mathrm{SNR}_k = \frac{|a_k|^2}{\sigma^2}
$$
(3.44)

The sample and frequency grid sizes are $L_s = 256$, $M_s = 256$, $N_s = 4$, $L_{\mathrm{DFT}} = 256$, $M_{\mathrm{DFT}} = 256$, $N_{\mathrm{DFT}} = 4$, respectively. In the first two dimensions, a 40 dB Chebyshev window is used and in the last dimension a rectangular window. We consider a frequency sub-band around the periodogram peak

$$
(\pi - 2F_\lambda, \pi + 2F_\lambda) \times (\pi - 3F_\mu, \pi + 3F_\mu) \times (\pi - 2F_\nu, \pi + 2F_\nu)
$$

and first test if it is due to a single or two cisoids. To this end, we calculate (3.12), (3.13), (3.14), yielding

$$
\mathrm{MSE}_\lambda = -10\,\mathrm{dB}, \quad \mathrm{MSE}_\mu = -34\,\mathrm{dB}, \quad \mathrm{MSE}_\nu = -24\,\mathrm{dB}.
$$
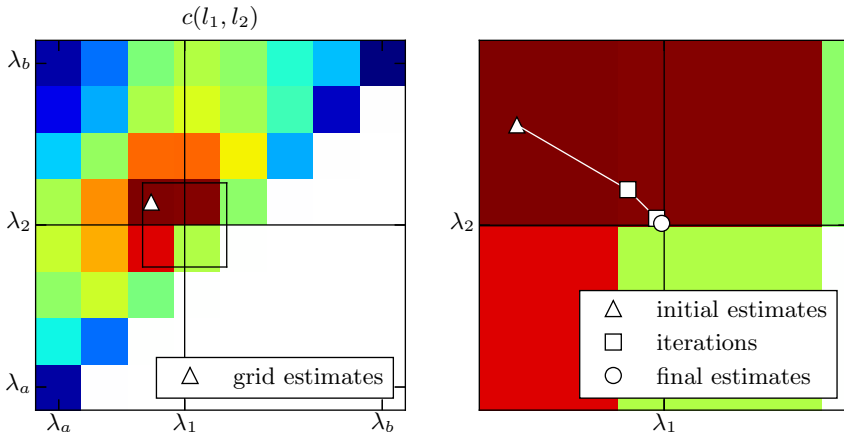
Figure 3.2: Left: NLS criterion function evaluated on a 64 point frequency grid. The position of its maximum is shown as triangle and is used as a starting point for the Gauss-Newton type iterations. Right: improved estimates per iteration in the vicinity of the coarse-grid result and final estimate after three iterations.

The largest value, $\mathrm{MSE}_1 = \mathrm{MSE}_\lambda = -10\,\mathrm{dB}$, is used to test for the single-cisoid model and to this end compare to $\gamma_1 = -50\,\mathrm{dB}$. Note that this particular value corresponds to a false alarm probability of 0.01 for the noise variance defined via (3.44). As MSE_1 clearly exceeds γ_1 we reject the single-cisoid hypothesis and opt for calculating the two-cisoid model. For the decoupled NLS method presented in Section 3.4.1.2 we select the resolution dimension according to the largest MSE value and thus the first dimension.

Having selected the resolution dimension we calculate the NLS criterion function (3.38) on a coarse, predefined grid $\Delta_{\lambda,\mathrm{NLS}} = 2\pi/400$ leading to 64 grid points in selected sub-band, as shown on the left hand side of Figure 3.2. The coarse-grid NLS estimate $\hat{\lambda}_{c,1}$ and $\hat{\lambda}_{c,2}$ are given by the position of the maximum, which is marked with a triangle. For reference we show the true values of λ_1 and λ_2 as solid lines. The estimation errors are $0.46F_\lambda$ and $0.32F_\lambda$, for the first and second cisoid, respectively. The coarse-grid NLS estimates serve now as a starting point for the Gauss-Newton refinement. To show the improvement per iteration, the rectangular area indicated in the left hand side plot is enlarged on the right hand side of Figure 3.2. Starting from the coarse grid estimates (triangle) we show two intermediate estimates obtained as in (3.39) (squares) and the final estimates (circle). After three iterations we have an
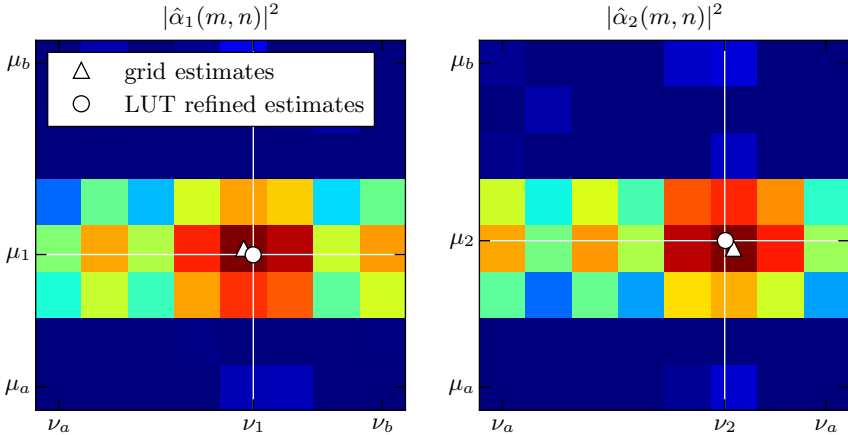
Figure 3.3: Magnitude squared of the estimated cisoid amplitudesevaluated on the DFT grid in the frequency sub-band. The true frequencies are shown as horizontal/vertical lines for reference. The maximizing frequencies on the DFT grid are shown as triangles and the LUT-refined estimates as circles.

estimation error of $0.001F_\lambda$ for both estimates. Thus the coarse-grid estimates are improved by two orders of magnitude by the Gauss-Newton method.

Based on the so obtained resolution-dimension estimates $\hat{\lambda}_1$ and $\hat{\lambda}_1$ we calculate $|\hat{\alpha}_1(\mu, \nu)|^2$ and $|\hat{\alpha}_2(\mu, \nu)|^2$ according to (3.22), which are shown in Figure (3.3) on a DFT grid. The frequencies of each maximum are indicated by triangles and the LUT-refined estimates according to (3.42) and (3.43) are shown as circles. The corresponding estimation errors are gathered in Table 3.1. Observe an improvement of two orders of magnitude due to the LUT refinement.

3.6 Simulation Results

We show Monte-Carlo (MC) simulation results for our proposed frequency estimation framework. In the simulations we considered two cisoids with parameters

$$a_1 = 1, \quad \lambda_1 = \lambda_m - 0.5\delta_\lambda, \quad \mu_1 = \mu_m - 0.5\delta_\mu, \quad \nu_1 = \nu_m - 0.5\delta_\nu, \quad (3.45)$$

$$a_2 = e^{j\varphi}, \quad \lambda_2 = \lambda_m + 0.5\delta_\lambda, \quad \mu_2 = \mu_m + 0.5\delta_\mu, \quad \nu_2 = \nu_m + 0.5\delta_\nu, \quad (3.46)$$

Table 3.1: Example: frequency estimation errors for the remaining dimensions.

Estimation error	DFT grid	LUT-refined
$|\hat{\mu}_1 - \mu_1|/F_\mu$	0.13	0.007
$|\hat{\nu}_1 - \nu_1|/F_\nu$	0.1	0.002
$|\hat{\mu}_2 - \mu_2|/F_\mu$	0.16	0.0004
$|\hat{\nu}_2 - \nu_2|/F_\nu$	0.09	0.001

where

$$\lambda_m = \frac{\lambda_1 + \lambda_2}{2}, \quad \mu_m = \frac{\mu_1 + \mu_2}{2}, \quad \nu_m = \frac{\nu_1 + \nu_2}{2}, \tag{3.47}$$

denote the two cisoids mid frequencies and δ_λ, δ_μ, and δ_ν denote the frequency separations. Optionally we consider a third, interfering, out-of-band cisoid with parameters λ_i, μ_i, ν_i, and

$$a_3 = \text{SIR}^{-1} e^{j\varphi_i}, \tag{3.48}$$

where SIR denotes the signal-to-interference ratio. We let the data sizes be

$$L_s = 256, \quad M_s = 256, \quad N_s = 4, \quad L_\text{DFT} = 256, \quad M_\text{DFT} = 256, \quad N_\text{DFT} = 8,$$

and use a 40 dB Chebyshev window in the first two and a rectangular window in the last dimension. We consider a frequency sub-band

$$(\pi - 2F_\lambda, \pi + 2F_\lambda) \times (\pi - 3F_\mu, \pi + 3F_\mu) \times (\pi - 2F_\nu, \pi + 2F_\nu)$$

such that all relevant periodogram peaks will be included.

3.6.1 Resolution dimension selection

We asses the performance of resolution dimension identification based on the single-cisoid model violation, which we proposed in Section 3.2.1. To this end we vary the frequency separation in the first frequency dimension δ_λ from 50 % to 100 % of the resolution limit and fix the frequency separations in the remaining dimensions δ_μ and δ_ν to 30 % of the respective resolution limit. Note that the frequency separation in the first dimension is at all times the largest and consequently the first dimension should be selected as resolution dimension. We carry out 1000 MC runs, where we draw the correlation phase φ uniformly from $(0, 2\pi)$ and the mid frequencies from $(\pi - \Delta_\lambda/2, \pi + \Delta_\lambda/2)$, $(\pi - \Delta_\mu/2, \pi + \Delta_\mu/2)$, $(\pi - \Delta_\nu/2, \pi + \Delta_\nu/2)$, respectively. As performance metric we consider the empirical probability of correct resolution dimension selection, that is the number of MC runs in which the resolution dimension was selected correctly over the total number of MC runs N_MC.
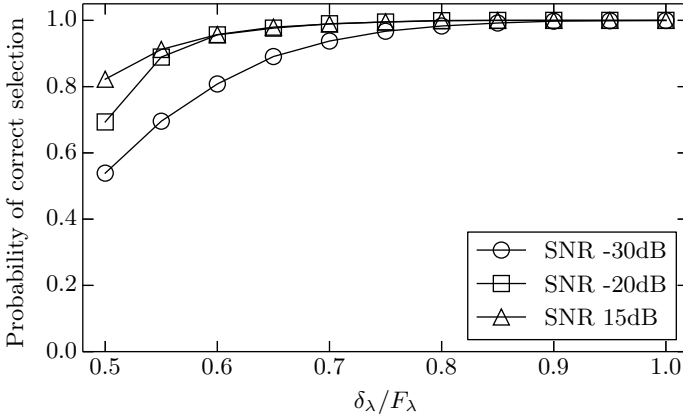
Figure 3.4: Probability of correctly selecting the dimension with largest frequency separation as resolution dimension. The frequency separation in the first dimension δ_λ is varied from 50 % to 100 % of the corresponding resolution limit and the separations in the remaining dimensions, δ_μ, δ_ν, are fixed to 30 % of the respective resolution limits.

Figure 3.4 shows the probability of correct resolution dimension selection over the frequency separation in the first dimension for different SNR values. Observe that for frequency separations above 60 % of the resolution limit the probability of correct resolution dimension selection is above 80 % for all SNR values.

3.6.2 Frequency estimation

We want to reveal the influence of the SNR, the frequency separation, and the SIR, on the single-cisoid and the decoupled two-cisoid frequency estimator. For the two-cisoid case we let the first dimension have the largest frequency separation and assume, that it was correctly selected as resolution dimension. Further, we let the grid size for the direct NLS search be

$$\Delta_{\lambda,\mathrm{NLS}} = 2\pi/400 \quad \Rightarrow \quad l_{b,\mathrm{NLS}} - l_{a,\mathrm{NLS}} = 8,$$

so that the NLS criterion function has to be evaluated on 64 grid points.

As performance metrics we consider the root mean square error (RMSE)

$$\mathrm{RMSE}_{\lambda,k} = \sqrt{\frac{1}{N_r} \sum_{c=1}^{N_r} \left(\hat{\lambda}_{k,c} - \lambda_k \right)^2}, \tag{3.49}$$

$$\mathrm{RMSE}_{\mu,k} = \sqrt{\frac{1}{N_r} \sum_{c=1}^{N_r} \left(\hat{\mu}_{k,c} - \mu_k \right)^2}, \tag{3.50}$$

$$\mathrm{RMSE}_{\nu,k} = \sqrt{\frac{1}{N_r} \sum_{c=1}^{N_r} \left(\hat{\nu}_{k,c} - \nu_k \right)^2}, \tag{3.51}$$

and the empirical probability of resolution

$$p_r = \frac{N_r}{N_{\mathrm{MC}}}. \tag{3.52}$$

Herein, $\hat{\lambda}_{k,c}$, $\hat{\mu}_{k,c}$, $\hat{\nu}_{k,c}$ denote the k-th frequency estimates in the c-th MC run, N_r the number of MC runs for which the two cisoids are successfully resolved, and N_{MC} denotes the total number of MC runs. To obtain N_r we consider the resolution definition (2.39). Note that we treat the non resolved cases as outliers and exclude them from the calculation of (3.49), (3.50), (3.51). To asses the simulation results we will compare the RMSE values with the corresponding CRB

$$\mathrm{CRB}_{\lambda,k} = \sqrt{[\mathbf{CRB}_\lambda]_{k,k}}, \tag{3.53}$$

$$\mathrm{CRB}_{\mu,k} = \sqrt{[\mathbf{CRB}_\mu]_{k,k}}, \tag{3.54}$$

$$\mathrm{CRB}_{\nu,k} = \sqrt{[\mathbf{CRB}_\nu]_{k,k}}, \tag{3.55}$$

where $\mathbf{CRB}_\lambda$, $\mathbf{CRB}_\mu$, $\mathbf{CRB}_\nu$ are given in (2.44).

We carried out 5000 MC runs, where we draw correlation phase φ and the out-of-band cisoids phase φ_i uniformly from $(0, 2\pi)$. The mid frequencies are uniformly drawn from

$$\begin{cases} (\pi - \Delta_\lambda/2, \pi + \Delta_\lambda/2), & \text{single-cisoid case} \\ (\pi - \Delta_{\lambda,\mathrm{NLS}}/2, \pi + \Delta_{\lambda,\mathrm{NLS}}/2), & \text{two-cisoid case} \end{cases}$$

in the first dimension and from $(\pi - \Delta_\mu/2, \pi + \Delta_\mu/2)$, $(\pi - \Delta_\nu/2, \pi + \Delta_\nu/2)$, in the remaining dimensions. We show only simulation points for which the probability of resolution as given in (3.52) is above 90 %.
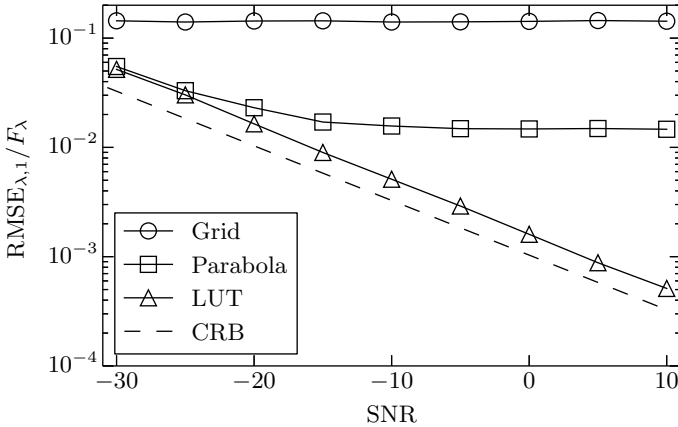
Figure 3.5: RMSE of single-cisoid frequency estimators for varying SNR. Compared are the conventional, frequency grid, periodogram maximizer, the parabolic interpolation approach, and the newly proposed LUT approach.

3.6.2.1 Noise influence

We want to reveal the noise influence on the performance of out frequency estimation framework. We consider the single as well as the two-cisoid cases. For the former we let $a_2 = a_3 = 0$ and compare the conventional, frequency-grid, periodogram maximizer, the parabolic interpolation approach, and the newly proposed LUT-refined approach of Section 3.3. Figure 3.5 shows the RMSE normalized to the resolution limit in the first frequency dimension for varying SNR. As the results are very similar in the other dimensions we omit the corresponding RMSE values.

To reveal the noise influence on decoupled frequency estimation in the two-cisoid case, we vary the SNR given in (3.44). The frequency separation in the resolution dimension is fixed to 50 % of the resolution limit and to 30 % of the respective resolution limit in the remaining dimensions. Further we let $a_3 = 0$, that means we consider no interfering out-of-band cisoid. Figure 3.6 shows the RMSE normalized to the respective resolution limits in one subplot per frequency dimension. For reference the CRB is shown for each frequency dimension. We compare the performance of the two pre-processing approaches according to (3.35) and consider the effect of orthogonalization as in (3.37). Observe that all approaches yield an RMSE close to the CRB.

3.6.2.2 Frequency separation

For assessing the influence of frequency separation we consider the separation in the resolution dimension and the separation in the remaining dimension, in one simulation each. For both cases we let $a_3 = 0$ and SNR $= 0\,$dB.

In the first simulation, the frequency separation in the resolution dimension is varied and the frequency separations in the remaining dimensions are fixed to $30\,\%$ of the respective resolution limit. The upper, middle, and lower plots of Figure 3.7 show the normalized RMSE and CRB for the first, second, and third frequency dimension, respectively. Observe that all pre-processing methods show a RMSE close to the CRB, in particular for increasing frequency separation. For small frequency separation, averaging over the non resolution dimensions (pre-processing 2) yields a slightly lower RMSE, compared to the maximum based pre-processing 1.

In the second simulation, the frequency separation in the resolution dimension is fixed to $50\,\%$ of the resolution limit and the frequency separations in the remaining dimension are varied equally, that is $\delta_\mu = \delta_\nu$. Figure 3.8 shows the RMSE for the first, second, and third frequency dimension together with the respective CRB. We can observe a performance close to the CRB for pre-processing 2 and an increasing RMSE for pre-processing 1 and larger frequency separations. This can be explained by the occurrence of multiple periodogram peaks for increasing frequency separation in the remaining dimensions. This results in an attenuation of one of the cisoids when using the maximal peak only, that is pre-processing 1, and in turn to a degraded estimation performance of the corresponding frequencies. In contrast, pre-processing 2 is based on averaging in the remaining dimensions and thus considers multiple peaks inherently.

3.6.2.3 Interfering cisoids

To assess the influence of out-of-band interference on decoupled frequency estimation, we consider one out-of-band cisoid with frequencies

$$\lambda_i = \lambda_m + 3F_\lambda, \quad \mu_i = \mu_m + 5F_\mu, \quad \nu_i = \nu_m + 5F_\nu,$$

and vary the SIR. The frequency separations of the two cisoids of interest are fixed to $50\,\%$ of the resolution limit in the resolution dimension and to $30\,\%$ of the respective resolution limit in the remaining dimensions. The SNR is $0\,$dB. Figure 3.9 shows the RMSE for the first, second, and third frequency dimension together with the respective CRB. Observe the degraded performance for the orthogonalization pre-processing according to (3.37) for low SIR values. This is expected from the discussion in Section 3.4.1.1 as the orthogonalization decreases the out-of-band interference suppression. For SIR above -20\,dB the noise influence starts to dominate

and the orthogonalization pre-processing outperforms the estimates without orthogonalization slightly.
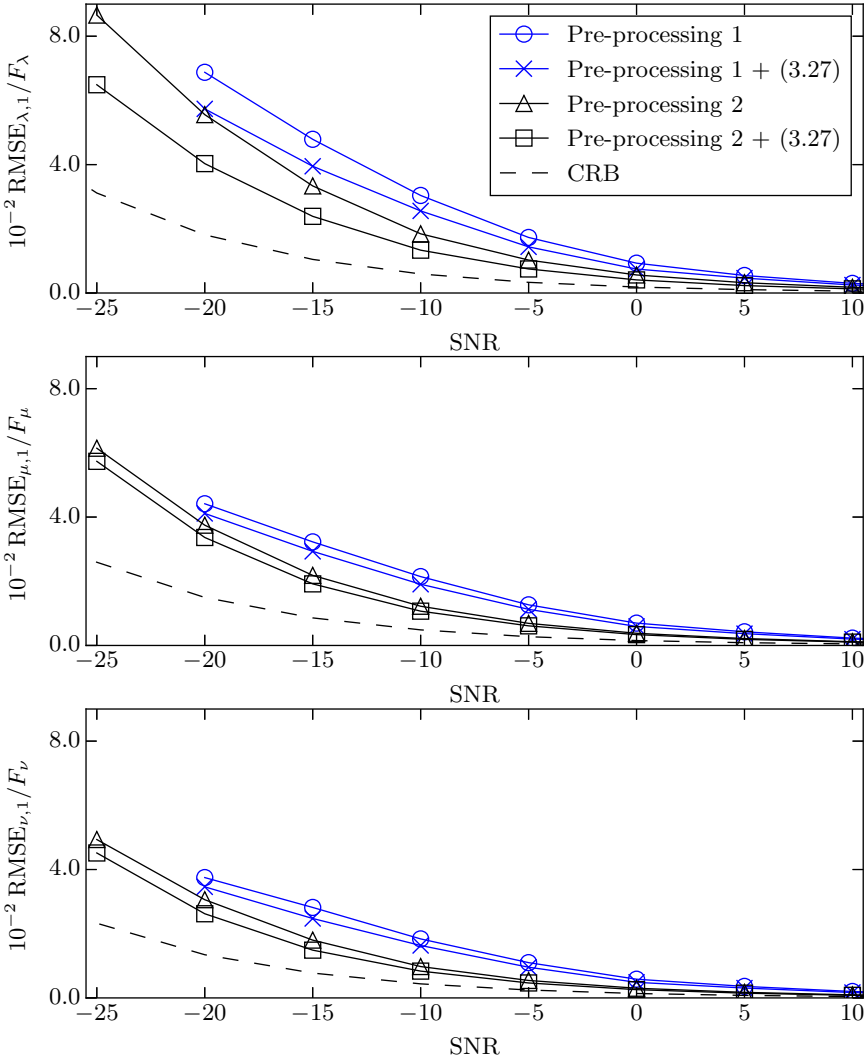
Figure 3.6: RMSE of the proposed decoupled two-cisoid frequency estimation for varying SNR. Compared are the two different pre-processing approaches according to (3.35) and the effects of orthogonalization. The RMSE is close to the CRB for all pre-processing approaches.
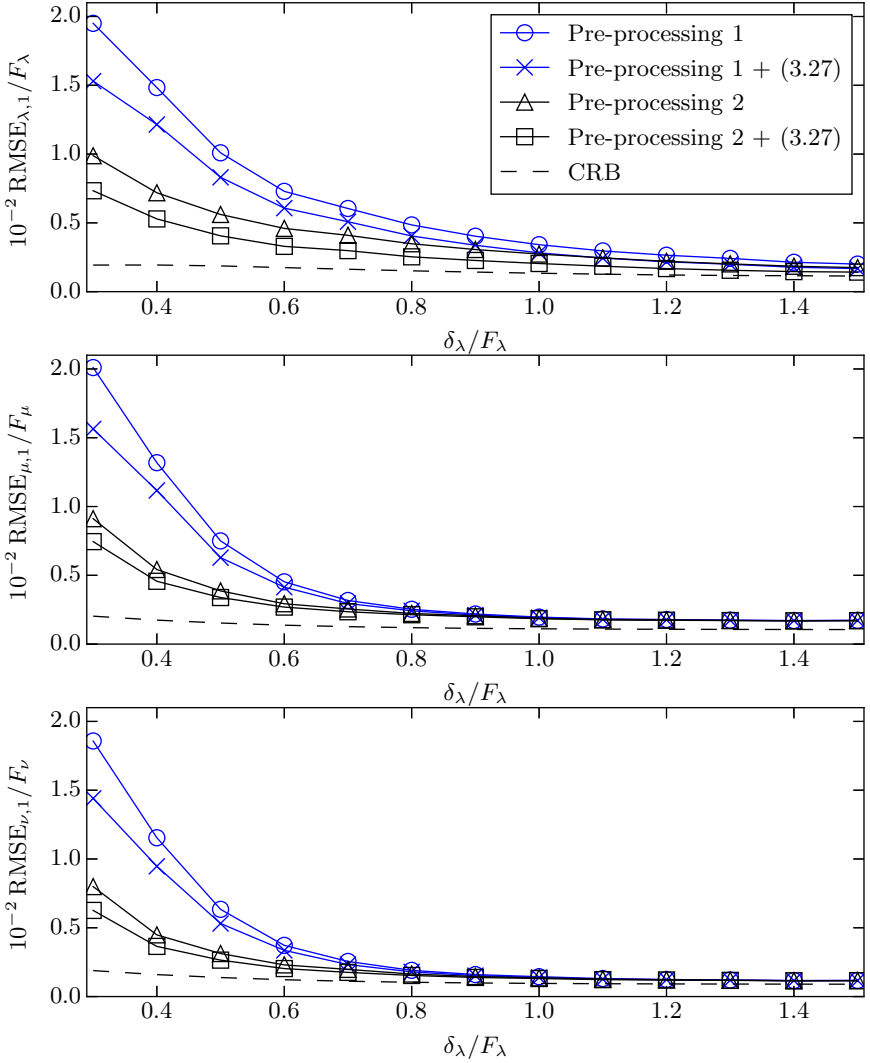
Figure 3.7: RMSE of the proposed decoupled two-cisoid frequency estimation for varying frequency separation in the resolution dimension. Compared are the two different pre-processing approaches according to (3.35) and the effects of orthogonalization. The RMSE is close to the CRB for all pre-processing approaches.
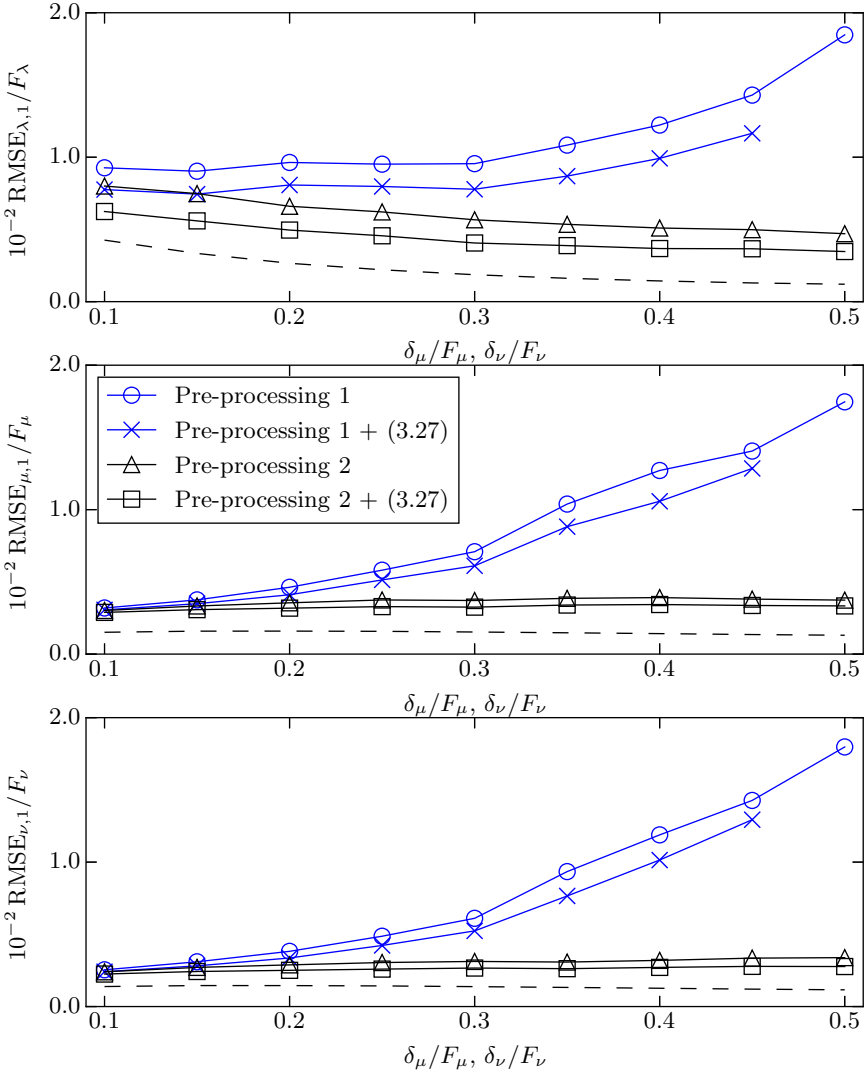
Figure 3.8: RMSE of the proposed decoupled two-cisoid frequency estimation for varying frequency separation in the remaining dimensions. Compared are the two different pre-processing approaches according to (3.35) and the effects of orthogonalization. For larger frequency separations, averaging in the remaining dimensions (pre-processing 2) is beneficial.
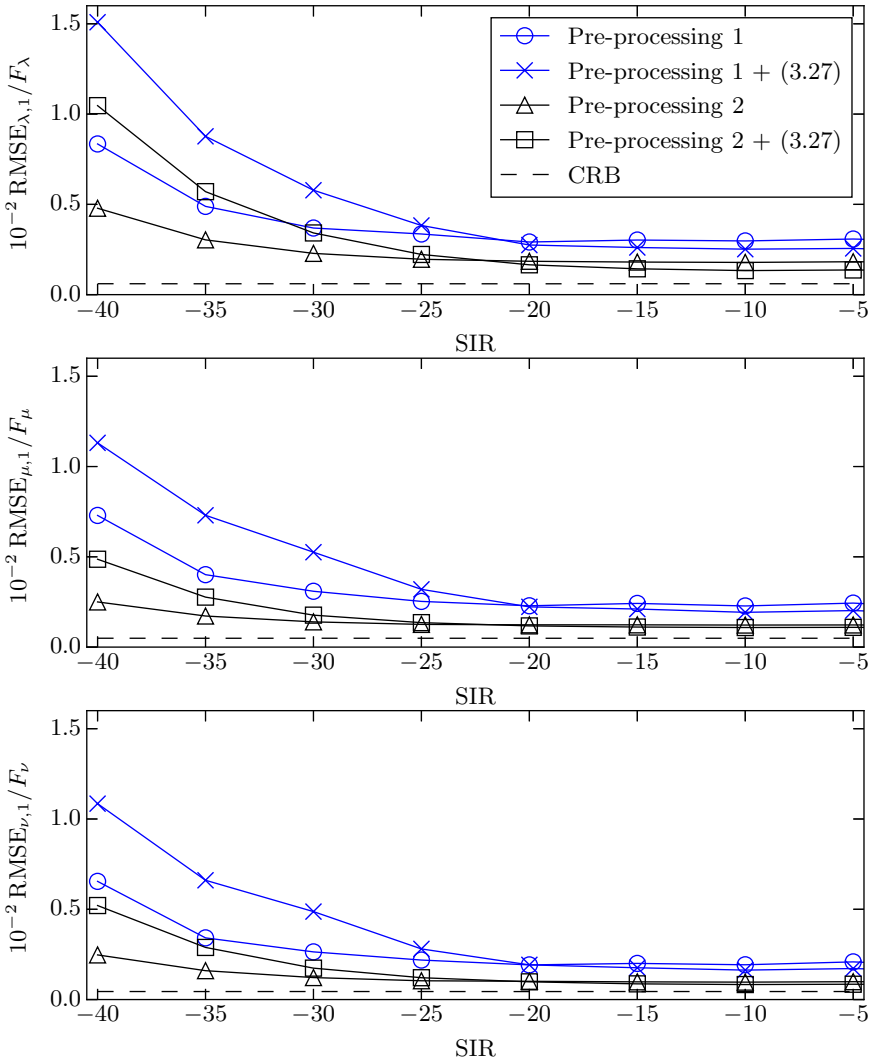
Figure 3.9: RMSE of the proposed decoupled two-cisoid frequency estimation for varying SIR. Compared are the two different pre-processing approaches according to (3.35) and the effects of orthogonalization. For low SIR values the effects of degraded out-of-band interference suppression due to orthogonalization can be observed.

3.A Appendix

3.A.1 Parabolic periodogram peak interpolation

Parabolic interpolation of the periodogram peak position is a popular approach for increasing the accuracy of periodogram-based frequency estimation [JK07]. The correction terms use two neighboring values of the periodogram peak position and are derived in [Ric14, Sec. 5.3.4].

The refined periodogram-based frequency estimates are given by

$$\hat{\lambda}_0 = \Delta_\lambda l_0 \; + \frac{\Delta_\lambda}{2} \frac{P(l_0 - 1, m_0, n_0) - P(l_0 + 1, m_0, n_0)}{P(l_0 + 1, m_0, n_0) + P(l_0 - 1, m_0, n_0) - 2P(l_0, m_0, n_0)},$$

$$\hat{\mu}_0 = \Delta_\mu m_0 + \frac{\Delta_\mu}{2} \frac{P(l_0, m_0 - 1, n_0) - P(l_0, m_0 + 1, n_0)}{P(l_0, m_0 + 1, n_0) + P(l_0, m_0 - 1, n_0) - 2P(l_0, m_0, n_0)},$$

$$\hat{\nu}_0 = \Delta_\nu n_0 \; + \frac{\Delta_\nu}{2} \frac{P(l_0, m_0, n_0 - 1) - P(l_0, m_0, n_0 + 1)}{P(l_0, m_0, n_0 + 1) + P(l_0, m_0, n_0 - 1) - 2P(l_0, m_0, n_0)},$$

where l_0, m_0, and n_0 are the peak indices. Note, that the achievable accuracy of the refined estimates varies for different window functions.

4 Frequency estimation based on a single-cisoid search

The main computational burden of the framework on multidimensional frequency estimation, developed in Chapter 3, is 1-D NLS-based frequency estimation for the two-cisoid model. Here, we present the single-cisoid search method as a computational simpler alternative to NLS-based frequency estimation. We give an overview in Section 4.1 and develop the single-cisoid search method in Section 4.2. We consider an optional bias correction step in Section 4.3 and give an example in Section 4.4. Section 4.5 presents simulation results to show the effectiveness of the proposed approach.

4.1 Overview

Consider the framework on multidimensional frequency estimation developed in Chapter 3. The computational complexity of the processing sequence shown in Figure 3.1 is determined by fitting the two-cisoid model in the resolution dimension, which involves the calculation of NLS-based frequency estimates, as discussed in Section 3.4.1.2. Here, we consider a computationally simpler approach, which we call single-cisoid search. It is based on identifying multiple remaining-dimension frequencies, for which the resolution dimension is well represented by a single-cisoid model. For distinct cisoid frequencies in at least two dimensions, the corresponding frequencies represent estimates of either the first or the second cisoid-frequency in the resolution dimension. The computational efficiency of that approach stems from the fact that the frequencies in the resolution dimension can be estimated by the periodogram.

Figure 4.1 gives an overview how the single-cisoid search approach can be used within the framework on multidimensional frequency estimation. The first processing steps, that is fitting of the single-cisoid models, determining the resolution dimension, and two-cisoid indication, are retained as in the original processing sequence in Figure 3.1. For the two-cisoid model, NLS-based frequency estimation in the resolution dimension is replaced by the single-cisoid search, which is developed in Section 4.2. Model selection and estimation of the frequencies in the remaining dimensions are performed as in the original processing sequence. The final frequency estimates can be refined by a bias correction step, which is presented in Section 4.2.
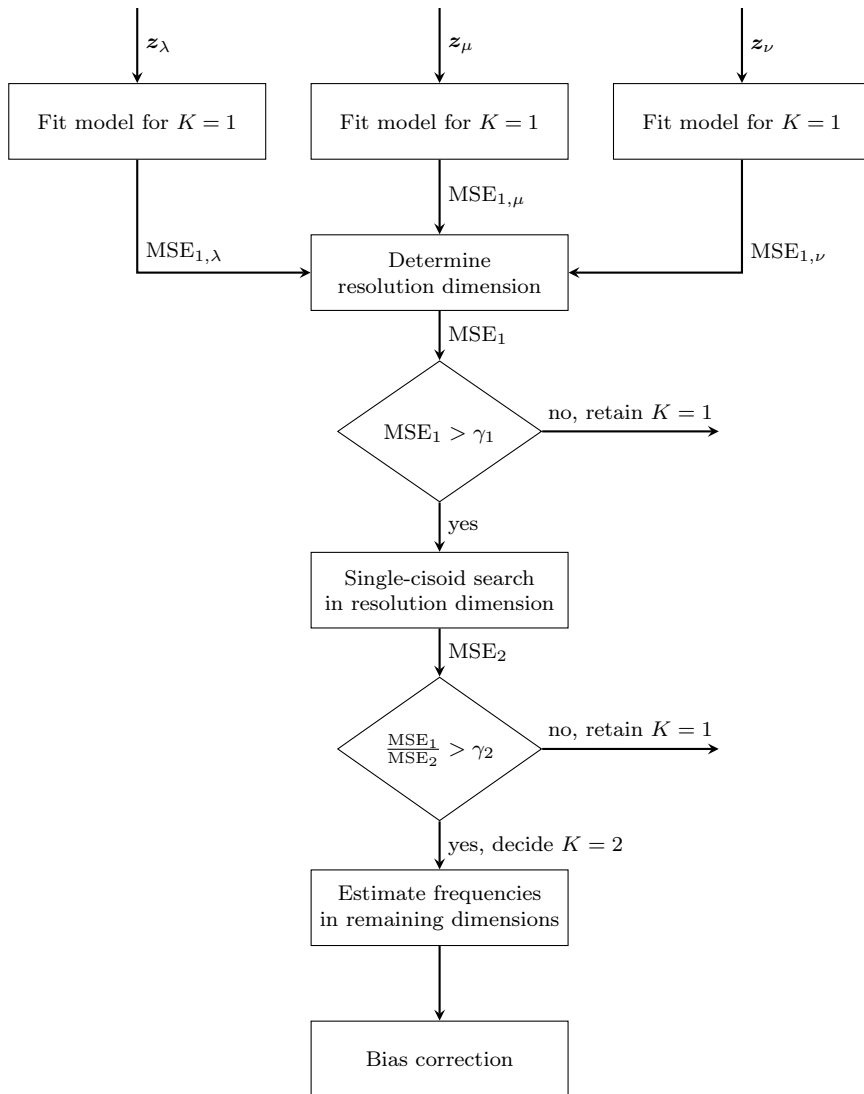
Figure 4.1: Processing sequence employing the single-cisoid search method for frequency estimation in the resolution dimension.

4.2 Proposed approach

Consider the two-cisoid model (3.2), which can be written as

$$X\left(\lambda,\mu,\nu\right) = \alpha_1\left(\lambda,\mu\right)W_\nu\left(\nu-\nu_1\right) + \alpha_2\left(\lambda,\mu\right)W_\nu\left(\nu-\nu_2\right) + \Xi\left(\lambda,\mu,\nu\right), \qquad (4.1)$$

where $\alpha_1(\lambda,\mu)$ and $\alpha_2(\lambda,\mu)$ are defined in (3.9). For distinct cisoid frequencies in the first or the second dimension the magnitudes $|\alpha_1(\lambda,\mu)|$ and $|\alpha_2(\lambda,\mu)|$ vary as functions of λ and μ. We refer to the cisoid with larger magnitude as stronger cisoid and to the one with smaller magnitude as weaker cisoid. To emphasize this, model (4.1) can be written as

$$X\left(\lambda,\mu,\nu\right) = \underbrace{\alpha_s\left(\lambda,\mu\right)W_\nu\left(\nu-\nu_s\right)}_{\text{stronger cisoid}} + \underbrace{\alpha_w\left(\lambda,\mu\right)W_\nu\left(\nu-\nu_w\right)}_{\text{weaker cisoid}} + \Xi\left(\lambda,\mu,\nu\right), \qquad (4.2)$$

where the roles of the stronger and weaker cisoid are complementary, that is for $\alpha_s(\lambda,\mu) = \alpha_1(\lambda,\mu)$ and $\nu_s = \nu_1$ we have $\alpha_w(\lambda,\mu) = \alpha_2(\lambda,\mu)$ and $\nu_w = \nu_2$ and vice versa.

Based on (4.2), the idea behind the proposed approach can be stated as follows: search frequencies λ and μ for which the weaker cisoid can be neglected $|\alpha_w(\lambda,\mu)| \approx 0$ and the stronger cisoids magnitude is sufficiently large $|\alpha_s(\lambda,\mu)| \gg 0$. For such frequencies, approximate (4.2) by a single-cisoid model

$$X\left(\lambda,\mu,\nu\right) \approx \alpha_s\left(\lambda,\mu\right)W_\nu\left(\nu-\nu_s\right) + \Xi\left(\lambda,\mu,\nu\right) \qquad (4.3)$$

and estimate its frequency ν_s by the periodogram maximizer

$$\hat{\nu}_s(\lambda,\mu) = \arg\max_\nu P(\lambda,\mu,\nu). \qquad (4.4)$$

From all frequencies obtained according to (4.4), select one estimate of ν_1 and another one of ν_2. If the last dimension is considered as resolution dimension in a decoupled multidimensional frequency estimation, the remaining dimension frequencies can be obtained as in Section 3.4.2. Note, that in the remainder of this chapter the last dimension is considered as resolution dimension for notational convenience.

To turn this approach in a practical frequency estimator, valid single-cisoid approximations according (4.3) have to be identified. To this end, a criterion is presented in Section 4.2.1. Further, estimates for ν_1 and ν_2 have to be selected from (4.4). Based on that criterion, the single-cisoid search algorithm for estimating the cisoid frequencies in the resolution dimension is developed in Section 4.2.2.

4.2.1 Single-cisoid criterion

A suitable test to decide if the resolution dimension is well represented by a single-cisoid model is

$$\rho(\lambda, \mu) < \gamma_\rho. \tag{4.5}$$

Here, the single-cisoid model is considered appropriate if the power ratio of the weaker and the stronger cisoid

$$\rho(\lambda, \mu) = \frac{|\alpha_w(\lambda, \mu)|^2}{|\alpha_s(\lambda, \mu)|^2} \tag{4.6}$$

falls below threshold γ_ρ. An estimator of (4.6) is derived next and practical threshold setting is considered in Section 4.2.2.1.

The power of the weaker cisoid can be obtained by subtracting the estimated stronger-cisoid model

$$\hat{\alpha}_s(\lambda, \mu) W_\nu(\nu - \hat{\nu}_s(\lambda, \mu))$$

from the model in (4.2), where $\hat{\alpha}_s(\lambda, \mu) = X(\lambda, \mu, \hat{\nu}_s)$. For small estimation errors, the power of the residual is determined by the power of the weaker cisoid

$$\int_{\nu_a}^{\nu_b} |X(\lambda, \mu, \nu) - \hat{\alpha}_s(\lambda, \mu) W_\nu(\nu - \hat{\nu}_s(\lambda, \mu))|^2 \, d\nu$$

$$\approx |\alpha_w(\lambda, \mu)|^2 \int_{\nu_a}^{\nu_b} |W_\nu(\nu - \nu_w)|^2 \, d\nu$$

$$\approx |\alpha_w(\lambda, \mu)|^2 \underbrace{\int_{\nu_a}^{\nu_b} |W_\nu(\nu - (\nu_a + \nu_b)/2)|^2 \, d\nu}_{\Lambda}$$

where the second approximation is valid if the mainlobe of $W_\nu(\nu - \nu_w)$ lies in (ν_a, ν_b). The nominator in (4.6) can thus be obtained by the scaled average power of the residual and the denominator by the amplitude in the estimated stronger-cisoid model, that is by $|\hat{\alpha}_s(\lambda, \mu)|^2$. Using this in (4.6) yields

$$\hat{\rho}(\lambda, \mu) = \underbrace{\frac{1}{|\hat{\alpha}_s(\lambda, \mu)|^2}}_{\text{stronger cisoid}} \underbrace{\frac{1}{\Lambda} \int_{\nu_a}^{\nu_b} |X(\lambda, \mu, \nu) - \hat{\alpha}_s(\lambda, \mu) W_\nu(\nu - \hat{\nu}_s(\lambda, \mu))|^2 d\nu}_{\text{weaker cisoid}}. \tag{4.7}$$

For discrete frequencies, (4.7) can be calculated based on the trapezoidal rule for integral approximation [AS64]

$$\hat{\rho}(l, m) = \frac{\|\mathbf{z}_\nu(l, m) - \hat{\alpha}_s(l, m) \mathbf{w}_\nu(\hat{\nu}_s(l, m))\|^2}{\Lambda |\hat{\alpha}_s(l, m)|^2}, \tag{4.8}$$

where $\mathbf{z}_\nu(l, m)$ is model (3.8) evaluated on the frequency grid, $\mathbf{w}_\nu(\nu)$ is given in (2.20), $\hat{\nu}_s(l, m)$ is the discrete version of the periodogram maximizer (4.4), and

$$\hat{\alpha}_s(l, m) = \mathbf{w}_\nu^+(\hat{\nu}_s(l, m))\mathbf{z}_\nu(l, m). \tag{4.9}$$

The discrete periodogram maximizer can be refined using the LUT approach presented in Section 3.3

$$
\begin{aligned}
&\hat{\nu}_s(l, m) \\
&= \begin{cases}
\Delta_\nu n_s + \mathrm{LUT}_\nu(\lfloor R(l, m)/\Delta_{R,\nu}\rfloor), & P(l, m, n_s + 1) > P(l, m, n_s - 1) \\
\Delta_\nu n_s - \mathrm{LUT}_\nu(\lfloor R(l, m)/\Delta_{R,\nu}\rfloor), & P(l, m, n_s + 1) < P(l, m, n_s - 1)
\end{cases}
\end{aligned} \tag{4.10}
$$

where n_s is the discrete periodogram maximizer in the resolution dimension and

$$R(l, m) = \log \frac{P(l, m, n_s)}{\max\{P(l, m, n_s - 1), P(l, m, n_s + 1)\}}.$$

4.2.2 Single-cisoid search

Here we derive the single-cisoid search algorithm for estimating the resolution dimension frequencies of the two-cisoid model. The algorithm can be outlined as follows: use the estimated power ratio (4.8) in the test (4.5) to identify remaining-dimension frequencies, for which the resolution dimension is well represented by a single-cisoid model. For such frequencies, estimate the frequencies in the resolution dimension by the corresponding periodogram maximizer. Out of the so obtained estimates, select two for estimating ν_1 and ν_2.

Details of the single-cisoid search are given in Algorithm 4.1 and can be subdivided in two main parts. The first comprises pre-processing, which calculates the stronger-cisoid frequencies (4.10) and the power ratios (4.8) in the resolution dimension for all frequencies in the remaining dimensions. This includes the intermediate steps of calculating the corresponding amplitudes as in (4.9) and subtracting the single-cisoid model from the data. The second part constitutes the main single-cisoid search algorithm, which initially sorts the power ratio values and stores the corresponding indices $l_i, m_i, i = 1, \ldots, LM$. This step can be motivated as follows. Recall, that the power ratio serves as goodness-of-fit criterion for the single-cisoid model and can thus be interpreted as a quality criterion for the corresponding frequency estimates in the resolution dimension. Thus, the estimates $\hat{\nu}_s(l_i, m_i)$, $i = 1, \ldots, LM$ are approximately ordered according to estimation error. In particular, $\hat{\nu}(l_1, m_1)$ is expected to have the smallest estimation error. Therefore it is selected as first candidate for a valid single-cisoid estimate and the corresponding power ratio $\hat{\rho}(l_1, m_1)$ is used in the single-cisoid test (4.5). If the single-cisoid hypothesis is rejected no valid single-cisoid model can be identified. Consequently the number of selected cisoids is set to zero and the algorithm terminates. If the single-cisoid hypothesis is accepted,

---

Algorithm 4.1: Single-cisoid search with pre-processing.

Input: Fourier-domain samples $\mathbf{z}_\nu(l, m)$, $l = l_a, \ldots, l_b$, $m = m_a, \ldots, m_b$

Result: Number of selected cisoids $\hat{K}$. Selected frequencies $\hat{\nu}_1$ and $\hat{\nu}_2$.

begin Preprocessing

    for $l = l_a, \ldots, l_b$, $m = m_a, \ldots, m_b$ **do**

        Calculate stronger cisoid frequency $\hat{\nu}_s(l, m)$ according to (4.10).

        Calculate corresponding amplitude $\hat{\alpha}_s(l, m) = \mathbf{w}_\nu^+(\hat{\nu}_s(l, m))\mathbf{z}_\nu(l, m)$.

        Calculate the power ratio

        $\hat{\rho}(l, m) = \|\mathbf{z}_\nu(l, m) - \hat{\alpha}_s(l, m)\mathbf{w}_\nu(\hat{\nu}_s(l, m))\|^2 / (\Lambda |\hat{\alpha}_s(l, m)|^2)$.

begin Single-cisoid search

    Sort according to power ratio, yielding l_i, m_i, $i = 1, \ldots, LM$

    such that $\hat{\rho}(l_i, m_i) > \hat{\rho}(l_{i+1}, m_{i+1})$.

    if $\hat{\rho}(l_1, m_1) > \gamma_\rho$ **then**

        No valid single-cisoid model found. Set $\hat{K} = 0$.

    else

        Single-cisoid model is valid. Set $\hat{\nu}_1 = \hat{\nu}_s(l_1, m_1)$ and $\hat{K} = 1$.

        for $i = 2, \ldots LM$ **and** $\hat{\rho}(l_i, m_i) < \gamma_\rho$ **do**

            if $[\hat{\nu}_s(l_i, m_i) - \hat{\nu}_1]^2 > \gamma_\nu$ **then**

                Current frequency is sufficiently separated from $\hat{\nu}_1$.

                Set $\hat{\nu}_2 = \hat{\nu}_s(l_i, m_i)$ and $\hat{K} = 2$. Terminate algorithm.

---

an estimate of ν_1 is found and the output values are set accordingly. To obtain the frequency of the second cisoid, the remaining frequency estimates are considered and the corresponding power ratios are used in the test (4.5). To avoid yet another estimate of ν_1, a sufficiently large separation to the already selected estimate is required. To this end, consider the following test

$$[\hat{\nu}_s(l, m) - \hat{\nu}_1]^2 > \gamma_\nu, \tag{4.11}$$

where $\hat{\nu}_1$ is the estimate corresponding to the smallest power ratio and γ_ν is a suitable threshold value. If (4.11) holds for the current frequency estimate the second estimate $\hat{\nu}_2$ is found, the output values are set accordingly, and the algorithm terminates. A practical approach to set the threshold γ_ν is presented in Section 4.2.2.1.

4.2.2.1 Practical threshold setting

Algorithm 4.1 comprises two subsequent hypothesis test for varying frequencies represented by l and m. The first, tests if the single-cisoid approximation (4.3) is valid for given l and m. If that test decides for a valid single-cisoid model, the corresponding estimates have to be associated to either ν_1 or ν_2. To this end, a second

test is used, which decides if a given estimate corresponds to the same cisoid frequency as the one selected according to the smallest available power ratio. The employed test statistics are the power ratio $\hat{\rho}_s(l,m)$ and the squared frequency separation $[\hat{\nu}_s(l,m) - \hat{\nu}_1]^2$ for the first and second test, respectively. Suitable threshold values γ_ρ and γ_ν can be determined as follows: obtain the empirical probability of false-alarm for given threshold values by simulations, that is generate a single-cisoid model with arbitrary ν_1 and predefined SNR. Vary the threshold values as long as a desired false-alarm probability is reached. For calculating the second test statistic use the squared estimation error of the single-cisoid frequency estimate. With that approach the probability of false-alarm for the first test is the probability of rejecting the single-cisoid hypothesis. For the second test, it is the probability of rejecting the hypothesis that the estimation error is due to a single-cisoid model plus noise.

The result of the described approach is a set of threshold values for given SNR values. To apply these thresholds in Algorithm 4.1, the effective SNR in the resolution dimension has to be obtained. To this end, the estimated stronger-cisoid amplitude (4.9) can be used together with the effective noise power in the resolution dimension. The latter can be estimated by calculating the average power in the resolution dimension for remaining-dimension frequencies without cisoids.

4.2.3 Adaption of resolution dimension selection

In Chapter 3 the dimension with the largest frequency separation is used as resolution dimension. This is motivated by the subsequent 1-D high- resolution frequency estimation, which benefits from a large frequency separation. In contrast the method proposed in Section 4.2 effectively exploits a frequency separation in the remaining dimensions. To see this, consider the power ratio (4.6), substitute the definition of the cisoid amplitudes (3.11), and distinguish the cases where either the first or the second cisoid dominates

$$
\rho(\lambda,\mu) = \frac{|\alpha_w(\lambda,\mu)|^2}{|\alpha_s(\lambda,\mu)|^2}
$$

$$
= \begin{cases} \dfrac{|a_2|^2\,\Omega_\lambda^2\,(\lambda - \lambda_2)\,\Omega_\mu^2\,(\mu - \mu_2)}{|a_1|^2\,\Omega_\lambda^2\,(\lambda - \lambda_1)\,\Omega_\mu^2\,(\mu - \mu_1)}, & |\alpha_1(\lambda,\mu)|^2 > |\alpha_2(\lambda,\mu)|^2 \\[3mm] \dfrac{|a_1|^2\,\Omega_\lambda^2\,(\lambda - \lambda_1)\,\Omega_\mu^2\,(\mu - \mu_1)}{|a_2|^2\,\Omega_\lambda^2\,(\lambda - \lambda_2)\,\Omega_\mu^2\,(\mu - \mu_2)}, & |\alpha_1(\lambda,\mu)|^2 < |\alpha_2(\lambda,\mu)|^2 \end{cases}
$$

For no frequency separation, that is $\lambda_1 = \lambda_2$ and $\mu_1 = \mu_2$, the power ratio is $|a_1|^2/|a_2|^2$ and thus constant with respect to λ and μ. As a consequence the single-cisoid search approach breaks down as no frequencies λ and μ lead to an effective single-cisoid model according to (4.3). For separation in at least one of the remaining

dimensions, that is $\lambda_1 \neq \lambda_2$ or $\mu_1 \neq \mu_2$, the power ratio is zero at frequencies satisfying

$$
\begin{cases}
\begin{cases}
\Omega_\lambda^2(\lambda - \lambda_2) = 0, & \lambda_1 \neq \lambda_2, \, \mu_1 = \mu_2 \\
\Omega_\mu^2(\mu - \mu_2) = 0, & \lambda_1 = \lambda_2, \, \mu_1 \neq \mu_2 \quad |\alpha_1(\lambda,\mu)|^2 > |\alpha_2(\lambda,\mu)|^2 \\
\Omega_\lambda^2(\lambda - \lambda_2)\Omega_\mu^2(\mu - \mu_2) = 0, & \lambda_1 \neq \lambda_2, \, \mu_1 \neq \mu_2
\end{cases} \\
\begin{cases}
\Omega_\lambda^2(\lambda - \lambda_1) = 0, & \lambda_1 \neq \lambda_2, \, \mu_1 = \mu_2 \\
\Omega_\mu^2(\mu - \mu_1) = 0, & \lambda_1 = \lambda_2, \, \mu_1 \neq \mu_2 \quad |\alpha_1(\lambda,\mu)|^2 < |\alpha_2(\lambda,\mu)|^2 \\
\Omega_\lambda^2(\lambda - \lambda_1)\Omega_\mu^2(\mu - \mu_1) = 0, & \lambda_1 \neq \lambda_2, \, \mu_1 \neq \mu_2
\end{cases}
\end{cases}
$$

For such frequencies, the resolution dimension is represented by a single-cisoid model and Algorithm 4.1 can work successfully. To ensure frequency separation in the remaining dimensions, we adapt the logic for resolution dimension selection presented in Section 4.2.3, such that the resolution dimension is selected according to the smallest value among (3.12), (3.13), and (3.14).

4.3 Bias reduction

For discrete frequencies, Algorithm 4.1 might not find frequencies in the remaining dimensions, for which the power ratio is exactly zero. This introduces a bias for the frequency estimates in the resolution dimension, which are obtained via periodogram maximization. This bias is propagated in a decoupled frequency estimation to the estimates in the remaining dimensions. Here, we propose a method to correct the bias terms in the resolution dimension as well as in the remaining dimensions.

Resolution dimension

Let l_1, m_1, l_2, and m_2, represent the frequencies in the remaining dimensions, which correspond to the frequency estimates in the resolution dimension, $\hat{\nu}_1$ and $\hat{\nu}_2$, obtained with Algorithm 4.1. Recall that the estimates $\hat{\nu}_1$ and $\hat{\nu}_2$ are obtained by periodogram maximization in the resolution dimension, based on a single-cisoid approximation according to (4.3). For discrete frequencies the respective weaker cisoid can have non-zero magnitude and thus perturbed single-cisoid models have to be considered

$$
X(\Delta_\lambda l_1, \Delta_\mu m_1, \nu) = \underbrace{\alpha_1(\Delta_\lambda l_1, \Delta_\mu m_1)}_{\alpha_{s,1}} W_\nu(\nu - \nu_1) + \underbrace{\alpha_2(\Delta_\lambda l_1, \Delta_\mu m_1)}_{\alpha_{w,1}} W_\nu(\nu - \nu_2)
$$

$$
X(\Delta_\lambda l_2, \Delta_\mu m_2, \nu) = \underbrace{\alpha_1(\Delta_\lambda l_2, \Delta_\mu m_2)}_{\alpha_{w,2}} W_\nu(\nu - \nu_1) + \underbrace{\alpha_2(\Delta_\lambda l_2, \Delta_\mu m_2)}_{\alpha_{s,2}} W_\nu(\nu - \nu_2)
$$

where the noise term has been dropped and $|\alpha_{s,1}| \gg |\alpha_{w,1}|$ and $|\alpha_{s,2}| \gg |\alpha_{w,2}|$. However, the magnitudes of the respective weaker cisoids are non-zero and therefore disturb the periodogram maximizer. To see this, consider the periodogram corresponding to the first perturbed resolution-dimension model

$$
\begin{aligned}
P\left(\Delta_\lambda l_1, \Delta_\mu m_1, \nu\right) & \qquad\qquad\qquad\qquad\qquad\qquad (4.12)\\
= & \underbrace{|\alpha_{s,1}|^2 \Omega_\nu^2(\nu - \nu_1)}_{\text{stronger cisoid}} + \underbrace{|\alpha_{w,1}|^2 \Omega_\nu^2(\nu - \nu_2)}_{\text{weaker cisoid}} \\
& + \underbrace{2\cos(\angle\alpha_{w,1}/\alpha_{s,1} + \delta_\nu(N_s - 1)/2)|\alpha_{s,1}||\alpha_{w,1}|\Omega_\nu(\nu - \nu_1)\Omega_\nu(\nu - \nu_2)}_{\text{cross term}},
\end{aligned}
$$

The periodogram can be subdivided into three terms: a stronger cisoid term, a weaker cisoid term, and a cross term. If the weaker cisoids magnitude is exactly zero, only the stronger-cisoid determines the peak position of (4.12), which is in that case at ν_1 and consequently $\hat{\nu}_1$ is unbiased. If the weaker cisoid has a non-zero magnitude, the weaker cisoid term and the cross term influence the peak position of the periodogram and introduce a bias in $\hat{\nu}_1$. The same argument holds for the second resolution-dimension estimate $\hat{\nu}_2$. Estimators of the bias terms in the resolution dimension are derived in Appendix 4.A.1 and are given by

$$
\hat{\beta}_{\nu,1} = \left[\frac{|\hat{\alpha}_{w,1}|^2}{|\hat{\alpha}_{s,1}|^2} + \frac{|\hat{\alpha}_{w,1}|}{|\hat{\alpha}_{s,1}|} \cos(\angle\hat{\alpha}_{w,1}/\hat{\alpha}_{s,1} - \hat{\delta}_\nu(N_s - 1)/2) \right] \frac{\dot{\Omega}_\nu(\hat{\delta}_\nu)}{\ddot{\Omega}_\nu(0)} \qquad (4.13)
$$

$$
\hat{\beta}_{\nu,2} = -\left[\frac{|\hat{\alpha}_{w,2}|^2}{|\hat{\alpha}_{s,2}|^2} + \frac{|\hat{\alpha}_{w,2}|}{|\hat{\alpha}_{s,2}|} \cos(\angle\hat{\alpha}_{w,2}/\hat{\alpha}_{s,2} + \hat{\delta}_\nu(N_s - 1)/2) \right] \frac{\dot{\Omega}_\nu(\hat{\delta}_\nu)}{\ddot{\Omega}_\nu(0)} \qquad (4.14)
$$

where $\hat{\delta}_\nu = \hat{\nu}_2 - \hat{\nu}_1$ and

$$
\begin{aligned}
\hat{\alpha}_{s,1} &= \hat{a}_1\, W_\lambda\left(\Delta_\lambda l_1 - \hat{\lambda}_1\right) W_\mu\left(\Delta_\mu m_1 - \hat{\mu}_1\right) \\
\hat{\alpha}_{w,1} &= \hat{a}_2\, W_\lambda\left(\Delta_\lambda l_1 - \hat{\lambda}_2\right) W_\mu\left(\Delta_\mu m_1 - \hat{\mu}_2\right) \\
\hat{\alpha}_{s,2} &= \hat{a}_2\, W_\lambda\left(\Delta_\lambda l_2 - \hat{\lambda}_2\right) W_\mu\left(\Delta_\mu m_2 - \hat{\mu}_2\right) \\
\hat{\alpha}_{w,2} &= \hat{a}_1\, W_\lambda\left(\Delta_\lambda l_2 - \hat{\lambda}_1\right) W_\mu\left(\Delta_\mu m_2 - \hat{\mu}_1\right)
\end{aligned}
$$

Herein,

$$
\begin{aligned}
\hat{a}_1 &= [\mathbf{w}_\lambda(\hat{\lambda}_1) \otimes \mathbf{w}_\mu(\hat{\mu}_1)]^+ \boldsymbol{\alpha}_1 \\
\hat{a}_2 &= [\mathbf{w}_\lambda(\hat{\lambda}_2) \otimes \mathbf{w}_\mu(\hat{\mu}_2)]^+ \boldsymbol{\alpha}_2
\end{aligned}
$$

where $[\boldsymbol{\alpha}_1]_i = \hat{\alpha}_1(l_a + i/M \mod L, m_a + i \mod M)$ and $[\boldsymbol{\alpha}_2]_i = \hat{\alpha}_2(l_a + i/M \mod L, m_a + i \mod M)$.

Remaining dimensions

To see how the bias of the estimates in the resolution dimension is propagated in the decoupled approach, consider the estimates in the remaining dimensions

$$\hat{\lambda}_1, \hat{\mu}_1 = \arg \max_{\lambda,\mu} |\hat{\alpha}_1(\lambda, \mu)|^2 \tag{4.15}$$

$$\hat{\lambda}_2, \hat{\mu}_2 = \arg \max_{\lambda,\mu} |\hat{\alpha}_2(\lambda, \mu)|^2 \tag{4.16}$$

where $\hat{\alpha}_1(\lambda, \mu)$ and $\hat{\alpha}_2(\lambda, \mu)$ are given in (3.24), which we restate here for reference

$$[\hat{\alpha}_1(\lambda, \mu), \hat{\alpha}_2(\lambda, \mu)]^{\mathrm{T}} = [\mathbf{w}_\nu(\hat{\nu}_1)\,\mathbf{w}_\nu(\hat{\nu}_2)]^+ \mathbf{z}_\nu(\lambda, \mu).$$

Substituting the noiseless decoupled model according to (3.8)

$$\mathbf{z}_\nu(\lambda, \mu) = [\mathbf{w}_\nu(\nu_1)\,\mathbf{w}_\nu(\nu_2)][\alpha_1(\lambda, \mu), \alpha_2(\lambda, \mu)]^{\mathrm{T}}$$

and considering the explicit form of the pseudoinverse for 2×2 matrices, yields

$$[\hat{\alpha}_1(\lambda, \mu), \hat{\alpha}_2(\lambda, \mu)]^{\mathrm{T}} = [\mathbf{w}_\nu(\hat{\nu}_1)\,\mathbf{w}_\nu(\hat{\nu}_2)]^+ [\mathbf{w}_\nu(\nu_1)\,\mathbf{w}_\nu(\nu_2)][\alpha_1(\lambda, \mu), \alpha_2(\lambda, \mu)]^{\mathrm{T}}$$

$$= \frac{1}{d} \begin{bmatrix} s_1 & r_1 \\ r_2 & s_2 \end{bmatrix} [\alpha_1(\lambda, \mu), \alpha_2(\lambda, \mu)]^{\mathrm{T}}$$

where

$$s_1 = [\mathbf{w}_\nu^{\mathrm{H}}(\hat{\nu}_2)\mathbf{w}_\nu(\hat{\nu}_2)\mathbf{w}_\nu^{\mathrm{H}}(\hat{\nu}_1) - \mathbf{w}_\nu^{\mathrm{H}}(\hat{\nu}_1)\mathbf{w}_\nu(\hat{\nu}_2)\mathbf{w}_\nu^{\mathrm{H}}(\hat{\nu}_2)]\mathbf{w}_\nu(\nu_1), \tag{4.17}$$

$$r_1 = [\mathbf{w}_\nu^{\mathrm{H}}(\hat{\nu}_2)\mathbf{w}_\nu(\hat{\nu}_2)\mathbf{w}_\nu^{\mathrm{H}}(\hat{\nu}_1) - \mathbf{w}_\nu^{\mathrm{H}}(\hat{\nu}_1)\mathbf{w}_\nu(\hat{\nu}_2)\mathbf{w}_\nu^{\mathrm{H}}(\hat{\nu}_2)]\mathbf{w}_\nu(\nu_2), \tag{4.18}$$

$$s_2 = [\mathbf{w}_\nu^{\mathrm{H}}(\hat{\nu}_1)\mathbf{w}_\nu(\hat{\nu}_1)\mathbf{w}_\nu^{\mathrm{H}}(\hat{\nu}_2) - \mathbf{w}_\nu^{\mathrm{H}}(\hat{\nu}_2)\mathbf{w}_\nu(\hat{\nu}_1)\mathbf{w}_\nu^{\mathrm{H}}(\hat{\nu}_1)]\mathbf{w}_\nu(\nu_2), \tag{4.19}$$

$$r_2 = [\mathbf{w}_\nu^{\mathrm{H}}(\hat{\nu}_1)\mathbf{w}_\nu(\hat{\nu}_1)\mathbf{w}_\nu^{\mathrm{H}}(\hat{\nu}_2) - \mathbf{w}_\nu^{\mathrm{H}}(\hat{\nu}_2)\mathbf{w}_\nu(\hat{\nu}_1)\mathbf{w}_\nu^{\mathrm{H}}(\hat{\nu}_1)]\mathbf{w}_\nu(\nu_1), \tag{4.20}$$

and d is a non-zero scalar, which depends on $\hat{\nu}_1$ and $\hat{\nu}_2$ and is here of no further interest. Consider the estimates in the remaining dimensions (4.15) corresponding to the first estimate in the resolution dimension $\hat{\nu}_1$, which are obtained by maximizing

$$|\hat{\alpha}_1(\lambda, \mu)|^2 = \tag{4.21}$$
$$\underbrace{\frac{|s_1|^2}{|d|^2}|\alpha_1(\lambda, \mu)|^2}_{\text{wanted}} + \underbrace{\frac{|r_1|^2}{|d|^2}|\alpha_2(\lambda, \mu)|^2 + 2\cos(\phi_1)\frac{|s_1||r_1|}{|d|^2}|\alpha_1(\lambda, \mu)||\alpha_2(\lambda, \mu)|}_{\text{error term}},$$

where $\phi_1 = \angle r_1/s_1 + \varphi + \delta_\lambda(L_s - 1)/2 + \delta_\mu(M_s - 1)/2$. The first term in (4.21), has its maximal peak at λ_1 and μ_1, that is at the actual cisoid frequencies. The second, error term in (4.21) scales with $|r_1|$ and leads to a peak shift. In this way, the bias in the resolution dimension is propagated to the remaining dimensions, as r_1 depends on the resolution dimension bias. The same argument holds for $|\alpha_2(\lambda, \mu)|^2$. Estimators

of the bias terms in the remaining dimensions are derived in Appendix 4.A.1 and are given by

$$\hat{\beta}_{\lambda,1} = \left[\frac{|\hat{r}_1|^2}{|\hat{s}_1|^2} \frac{|\hat{a}_2|^2}{|\hat{a}_1|^2} \Omega_\mu^2(\hat{\delta}_\mu) + \frac{|\hat{r}_1|}{|\hat{s}_1|} \frac{|\hat{a}_2|}{|\hat{a}_1|} \Omega_\mu(\hat{\delta}_\mu) \cos(\hat{\phi}_1) \right] \frac{\dot{\Omega}_\lambda(\hat{\delta}_\lambda)}{\ddot{\Omega}_\lambda(0)}, \quad (4.22)$$

$$\hat{\beta}_{\lambda,2} = -\left[\frac{|\hat{r}_2|^2}{|\hat{s}_2|^2} \frac{|\hat{a}_1|^2}{|\hat{a}_2|^2} \Omega_\mu^2(\hat{\delta}_\mu) + \frac{|\hat{r}_2|}{|\hat{s}_2|} \frac{|\hat{a}_1|}{|\hat{a}_2|} \Omega_\mu(\hat{\delta}_\mu) \cos(\hat{\phi}_2) \right] \frac{\dot{\Omega}_\lambda(\hat{\delta}_\lambda)}{\ddot{\Omega}_\lambda(0)}, \quad (4.23)$$

$$\hat{\beta}_{\mu,1} = \left[\frac{|\hat{r}_1|^2}{|\hat{s}_1|^2} \frac{|\hat{a}_2|^2}{|\hat{a}_1|^2} \Omega_\lambda^2(\hat{\delta}_\lambda) + \frac{|\hat{r}_1|}{|\hat{s}_1|} \frac{|\hat{a}_2|}{|\hat{a}_1|} \Omega_\lambda(\hat{\delta}_\lambda) \cos(\hat{\phi}_1) \right] \frac{\dot{\Omega}_\mu(\hat{\delta}_\mu)}{\ddot{\Omega}_\mu(0)}, \quad (4.24)$$

$$\hat{\beta}_{\mu,2} = -\left[\frac{|\hat{r}_2|^2}{|\hat{s}_2|^2} \frac{|\hat{a}_1|^2}{|\hat{a}_2|^2} \Omega_\lambda^2(\hat{\delta}_\lambda) + \frac{|\hat{r}_2|}{|\hat{s}_2|} \frac{|\hat{a}_1|}{|\hat{a}_2|} \Omega_\lambda(\hat{\delta}_\lambda) \cos(\hat{\phi}_2) \right] \frac{\dot{\Omega}_\mu(\hat{\delta}_\mu)}{\ddot{\Omega}_\mu(0)}, \quad (4.25)$$

where $\hat{\delta}_\lambda = \hat{\lambda}_2 - \hat{\lambda}_1$, $\hat{\delta}_\mu = \hat{\mu}_2 - \hat{\mu}_1$,

$$\hat{\phi}_1 = \angle \hat{r}_1/\hat{s}_1 + \angle \hat{a}_2/\hat{a}_1 + \hat{\delta}_\mu(M_s - 1)/2 + \hat{\delta}_\lambda(L_s - 1)/2,$$
$$\hat{\phi}_2 = \angle \hat{r}_2/\hat{s}_2 + \angle \hat{a}_2/\hat{a}_1 - \hat{\delta}_\mu(M_s - 1)/2 - \hat{\delta}_\lambda(L_s - 1)/2,$$

and $\hat{s}_1$, $\hat{r}_1$, $\hat{s}_2$, and $\hat{r}_2$, are obtained by substituting $\nu_1 = \hat{\nu}_1 - \hat{\beta}_{\nu,1}$ and $\nu_2 = \hat{\nu}_2 - \hat{\beta}_{\nu,2}$ in (4.17), (4.18), (4.19), and (4.20), respectively.

4.3.1 Window functions with broad zeros

Another approach for bias reduction are special window functions. To derive such window functions reconsider that the resolution-dimension estimates are biased because the peak position of the periodogram is influenced by a weaker-cisoid and a cross term, as in (4.12). Both terms scale with

$$|\alpha_{w,1}|^2 = |\alpha_2(\Delta_\lambda l_1, \Delta_\mu m_1)|^2 = |a_2|^2 \, \Omega_\lambda^2(\Delta_\lambda l_1 - \lambda_2) \, \Omega_\mu^2(\Delta_\mu m_1 - \mu_2),$$
$$|\alpha_{w,1}| = |\alpha_2(\Delta_\lambda l_1, \Delta_\mu m_1)| = |a_2| \, |\Omega_\lambda(\Delta_\lambda l_1 - \lambda_2)||\Omega_\mu(\Delta_\mu m_1 - \mu_2)|,$$

respectively. Due to the frequency discretization, $\Omega_\lambda(\Delta_\lambda l_1 - \lambda_2) \neq 0$ and $\Omega_\mu(\Delta_\mu m_1 - \mu_2) \neq 0$, and $\Delta_\lambda l_1$ and $\Delta_\mu m_1$ are rather close to frequencies λ_z and μ_z, for which $\Omega_\lambda(\lambda_z - \lambda_2) = 0$ and $\Omega_\mu(\mu_z - \mu_2) = 0$. The values of $|\alpha_{w,1}|^2$ and $|\alpha_{w,1}|$ are therefore determined by $\Omega_\lambda^2(\lambda - \lambda_2)$, $\Omega_\mu^2(\mu - \mu_2)$, $|\Omega_\lambda(\lambda - \lambda_2)|$, and $|\Omega_\mu(\mu - \mu_2)|$ in the vicinity of λ_z and μ_z, respectively. From the Taylor expansions around λ_z and μ_z

$$\Omega_\lambda^2(\lambda) = \dot{\Omega}_\lambda^2(\lambda_z)[\lambda - \lambda_z]^2 + O(|\lambda - \lambda_z|^3)$$
$$\Omega_\mu^2(\mu) = \dot{\Omega}_\mu^2(\mu_z)[\mu - \mu_z]^2 + O(|\mu - \mu_z|^3)$$
$$|\Omega_\lambda(\lambda)| = 2\dot{\Omega}_\lambda(\lambda_z)[\lambda - \lambda_z] + O(|\lambda - \lambda_z|^2)$$
$$|\Omega_\mu(\mu)| = 2\dot{\Omega}_\mu(\mu_z)[\mu - \mu_z] + O(|\mu - \mu_z|^2)$$

we see that the magnitude of the weaker cisoid term and the cross term in (4.12) can be reduced by altering the window functions such that $\dot{\Omega}_\lambda (\lambda_z) = 0$ and $\dot{\Omega}_\mu (\mu_z) = 0$. To obtain such window functions, consider the first frequency dimension and write

$$\Omega_\lambda (\lambda) = \mathbf{w}_s^{\mathrm{T}} \mathbf{a} (\lambda), \quad \dot{\Omega}_\lambda (\lambda) = \mathbf{w}_s^{\mathrm{T}} \dot{\mathbf{a}} (\lambda),$$

where $\mathbf{w}_s$, $\mathbf{a} (\lambda)$, and $\dot{\mathbf{a}} (\lambda)$, are $\mathbb{R}^L$ vectors with elements given by

$$[\mathbf{w}_s]_l = w_\lambda (l),$$
$$[\mathbf{a} (\lambda)]_l = \cos\left(\lambda \left[l - \frac{L_s - 1}{2} \right] \right),$$
$$[\dot{\mathbf{a}} (\lambda)]_l = \sin\left(\lambda \left[l - \frac{L_s - 1}{2} \right] \right), \left[\frac{L_s - 1}{2} - l \right]$$

respectively. Let $\mathbf{w}_s$ denote the original window sequence and $\mathbf{w}_z$ the desired sequence for which $\dot{\Omega}_\lambda (\lambda_z) = 0$. The following optimization problem can be formulated: minimize the squared error of the amplitude functions

$$\int \left| \mathbf{w}_s^{\mathrm{T}} \mathbf{a} (\lambda) - \mathbf{w}_z^{\mathrm{T}} \mathbf{a} (\lambda) \right|^2 d\lambda,$$

subject to

$$\mathbf{w}_s^{\mathrm{T}} [\mathbf{a} (\lambda_z), \dot{\mathbf{a}} (\lambda_z)] = \mathbf{0}.$$

The solution is [vT02, Ch. 3.7]

$$\mathbf{w}_z^{\mathrm{T}} = \mathbf{w}_s^{\mathrm{T}} \left[\mathbf{I}_L - [\mathbf{a} (\lambda_z), \dot{\mathbf{a}} (\lambda_z)] [\mathbf{a} (\lambda_z), \dot{\mathbf{a}} (\lambda_z)]^+ \right].$$

For a practical approach, λ_z has to be determined. To this end, note that for frequency separations below the resolution limit, λ_z coincides with one of the two zeros closest to λ_2 and therefore $\lambda_z = \lambda_2 \pm \mathrm{MLW}_\lambda$. Substituting MLW_λ for λ_z yields the desired window sequence for the first frequency dimension

$$\mathbf{w}_z^{\mathrm{T}} = \mathbf{w}_s^{\mathrm{T}} \left[\mathbf{I}_L - [\mathbf{a} (\mathrm{MLW}_\lambda), \dot{\mathbf{a}} (\mathrm{MLW}_\lambda)] [\mathbf{a} (\mathrm{MLW}_\lambda), \dot{\mathbf{a}} (\mathrm{MLW}_\lambda)]^+ \right].$$

The same approach can be straightforwardly extended to the second and third frequency dimension.

4.4 Example

Here we present an example of frequency estimation based on the single-cisoid search as described in Algorithm 4.1. We consider two cisoids with the following parameters

$$a_1 = e^{j5.851}, \quad \lambda_1 = \pi - 0.5\delta_\lambda, \quad \mu_1 = \pi - 0.5\delta_\mu, \quad \nu_1 = \pi - 0.5\delta_\nu,$$
$$a_2 = e^{j2.004}, \quad \lambda_2 = \pi + 0.5\delta_\lambda, \quad \mu_2 = \pi + 0.5\delta_\mu, \quad \nu_2 = \pi + 0.5\delta_\nu,$$

where the frequency separation is $\delta_\lambda = 0.5\,F_\lambda$, $\delta_\mu = 0.75\,F_\mu$, $\delta_\nu = 0.5\,F_\nu$ and $\text{SNR}_1 = \text{SNR}_2 = 0\,\text{dB}$. The sample support is $L_s = 256$, $M_s = 256$, $N_s = 4$, respectively, and the sizes for calculating the DFT are $L_{\text{DFT}} = 256$, $M_{\text{DFT}} = 256$, $N_{\text{DFT}} = 8$. In the first two dimensions a $40\,\text{dB}$ Chebyshev window is used and in the last dimension a rectangular window. The frequency sub-band is set to

$$(\pi - F_\lambda, \pi + F_\lambda) \times (\pi - F_\mu, \pi + F_\mu) \times (\pi - 2F_\nu, \pi + 2F_\nu).$$

The focus is on Algorithm 4.1 and the bias correction presented in Section 4.2.1. We assume that the last dimension was selected as resolution dimension and that the first test in the flowchart shown in Figure 4.1 correctly rejects the single-cisoid model and that the second test correctly decides for the two-cisoid model.

Algorithm 4.1 begins with the calculation of the frequency estimates in the resolution dimension, the corresponding amplitude, and the power ratio for each frequency in the selected sub-band. Figure 4.2 (a, left) shows the calculated power ratio, where only values within the considered frequency sub-band are color-coded. Figure 4.2 (a, right) shows the calculated power ratio values, which fall below the threshold γ_ρ in the test (4.5). Note that we used a false-alarm probability of $90\,\%$ to set the threshold $\gamma_\rho = 0.33/\text{SNR}_r$, where SNR_r is the effective SNR in the resolution dimension. Figure 4.2 (b) shows the frequency estimates obtained via (4.10), which correspond to the power ratio values shown in Figure 4.2 (a). The true cisoid frequencies are shown as vertical lines for reference. Note that only estimates for which the corresponding power ratio is below γ_ρ are considered in Algorithm 4.1. Consequently, the estimates corresponding to the two smallest power ratio values are used in the test (4.11), where we used a false-alarm probability of $99\,\%$ to set the threshold $\gamma_\nu = 0.66/\text{SNR}_r$. As the separation of both estimates exceeds γ_ν, they are finally selected as estimates for ν_1 and ν_2.

Based on the selected frequency estimates in the resolution dimension the frequencies in the remaining dimensions are obtained as presented in Section 3.4.2. The estimation errors for all frequency dimensions are gathered in Table 4.1. Using the bias correction approach, presented in Section 4.2.1, the estimation errors can be reduced by one order of magnitude.

4.5 Simulation Results

In this section, the influence of SNR, frequency separation, and interfering out-of-band cisoids are assessed via MC simulations and compared to the CRB. We use the same parametrization as in Section 3.6, that is the two cisoids are modeled via the correlation phase φ, the mid frequencies λ_m, μ_m, and ν_m, and the frequency
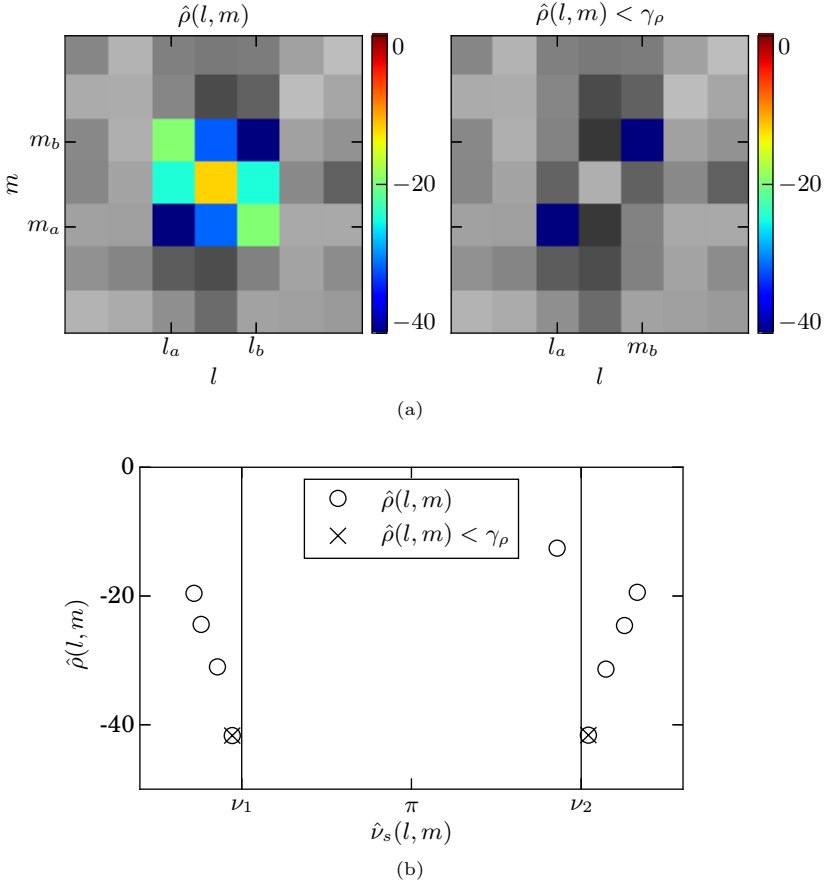
Figure 4.2: (a) Estimated power ratio in the selected frequency sub-band (left) and the selected remaining dimension frequencies obtained by Algorithm 4.1 (right). (b) Estimated frequencies in the resolution dimension and corresponding power ratios for the selected frequency sub-band. The value pairs selected by Algorithm 4.1 are marked.

separations δ_λ, δ_μ, and δ_ν as in (3.45) and (3.46), respectively. An optional out-of-band cisoid is modelled via (3.48). The data sizes are

$$L_s = 256, \quad M_s = 256, \quad N_s = 4, \quad L_{\mathrm{DFT}} = 256, \quad M_{\mathrm{DFT}} = 256, \quad N_{\mathrm{DFT}} = 8,$$

and the employed window functions are 40 dB Chebyshev windows in the first two dimensions and a rectangular window in the last dimension. The considered frequency

Table 4.1: Example: frequency estimation errors.

Estimation error	Algorithm 4.1	+ bias correction
$|\hat{\lambda}_1 - \lambda_1|/F_\lambda$	0.0043	0.0002
$|\hat{\mu}_1 - \mu_1|/F_\mu$	0.0054	0.0002
$|\hat{\nu}_1 - \nu_1|/F_\mu$	0.0139	0.0035
$|\hat{\lambda}_2 - \lambda_2|/F_\lambda$	0.0037	0.0006
$|\hat{\mu}_2 - \mu_2|/F_\mu$	0.0054	0.0002
$|\hat{\nu}_2 - \nu_2|/F_\nu$	0.0106	0.0002

sub-band is

$$(\pi - 2F_\lambda, \pi + 2F_\lambda) \times (\pi - 3F_\mu, \pi + 3F_\mu) \times (\pi - 2F_\nu, \pi + 2F_\nu).$$

In each MC run the correlation phase φ is drawn uniformly from $(0, 2\pi)$. To allow for a fair assessment of frequency grid effects, the mid frequencies are also uniformly drawn from

$$(\pi - \Delta_\lambda/2, \pi + \Delta_\lambda/2), \quad (\pi - \Delta_\mu/2, \pi + \Delta_\mu/2), \quad (\pi - \Delta_\nu/2, \pi + \Delta_\nu/2),$$

respectively. The RMSE values according to (3.49), (3.50), and (3.51) are used as performance metric. Additionally the empirical probability of resolution p_r according to (3.52) is calculated and used to exclude simulation points for which $p_r > 90\%$ from the results. To asses the estimation performance we compare the RMSEs to the corresponding CRBs (3.53), (3.54), and (3.55).

We used false-alarm probabilities of 90 % and 99 % to set the threshold values to $\gamma_\rho = 0.33/\text{SNR}_r$ and $\gamma_\nu = 0.66/\text{SNR}_r$, respectively, where SNR_r is the effective SNR in the resolution dimension. In the simulations we calculate SNR_r based on the estimated power of the stronger cisoid and on the effective noise variance in the resolution dimension according to (2.9)

$$\sigma^2 \, C_\lambda(0) \, C_\mu(0).$$

Note, that in practice, the effective noise variance has to be estimated.

For comparison the conventional periodogram estimator is calculated according to Section 2.2.2. To this end, the two largest periodogram peaks in the sub-band are considered and the LUT-based approach presented in Section 3.3 is used for both peaks.
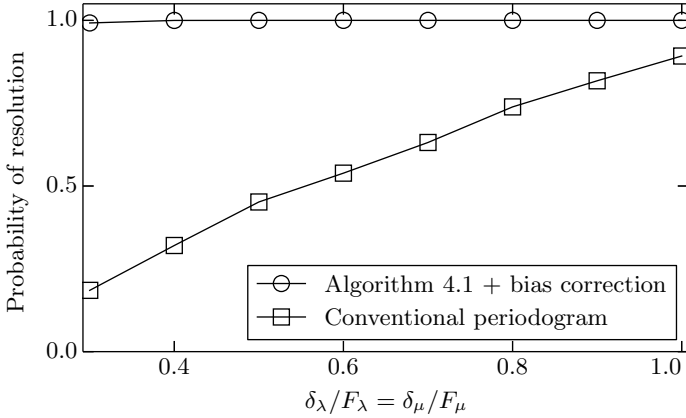
Figure 4.3: Probability of resolution of the single-cisoid search algorithm and the conventional periodogram for varying frequency separation in the remaining dimensions.

4.5.1 Noise influence

To assess the SNR influence on the single-cisoid search algorithm fix the frequency separation to

$$\delta_\lambda = 0.5\, F_\lambda, \quad \delta_\mu = 0.75\, F_\mu, \quad \delta_\nu = 0.5\, F_\nu$$

and vary SNR $=$ SNR$_1$ $=$ SNR$_2$ according to (3.44) per MC run. Further let $a_3 = 0$, that means no out-of-band interference is considered. Figure 4.4 shows the RMSE per frequency dimension for Algorithm 4.1. Additionally the result of the bias correction step developed Section 4.3 and the respective CRB is shown. Note that the RMSE values as well as the CRBs are normalized to the corresponding resolution limit. Observe a performance close to the CRB and a slightly lower RMSE for the additional bias correction. Note that the conventional periodogram method was only able to resolve the two cisoids in under 50 % of the MC runs and thus no simulation points are shown in Figure 4.4.

4.5.2 Frequency separation

To asses the influence of frequency separation on the single-cisoid search approach, consider a high SNR case with no out-of-band interference, that is SNR $=$ SNR$_1$ $=$ SNR$_2$ $= 10$ dB and $a_3 = 0$.

In a first simulation we consider frequency separation in the remaining dimensions. To this end, the separation in the resolution dimension is fixed to 50 % of the respective resolution limit and the separations in the remaining dimensions, normalized to the respective resolution limit, are varied equally, that is $\delta_\lambda/F_\lambda = \delta_\mu/F_\mu$. Figure 4.5 shows the normalized RMSE of Algorithm 4.1 and of additional bias correction according to Section 4.3. In addition, the respective RMSEs are shown if the Chebychev windows employed in the remaining dimensions are modified as proposed in Section 4.3.1. The first observation is that the RMSE decreases with separation in the remaining dimensions, which was expected from the discussion in Section 4.2.3. Observe further a clear improvement due to bias correction and also a strong improvement due to the modified window functions. Note that the empirical resolution probabilities of the conventional periodogram estimator was below 90 % for all separations and consequently the corresponding RMSE is omitted in Figure 4.5. Therefore we show the empirical resolution probabilities of Algorithm 4.1 and the conventional periodogram method in Figure 4.3. Observe that the resolution probability is below 90 % for all separations, whereas it is almost 100 % for Algorithm 4.1.

In another simulation, the influence of frequency separation in the resolution dimension is analyzed. To this end, the separations in the remaining dimensions are fixed to 50 % of the respective resolution limit and the separation in the resolution dimension is varied. As in the first simulation we let $\text{SNR} = \text{SNR}_1 = \text{SNR}_2 = 10\,\text{dB}$ and $a_3 = 0$. The RMSE of Algorithm 4.1 and the additional bias correction did not change with respect to the values found in Section 4.5.1. Therefore we conclude that the separation in the resolution influence has only a minor influence on Algorithm 4.1.

4.5.3 Interfering cisoids

To assess the influence of out-of-band interference on the single-cisoid search approach we consider an additional out-of-band cisoid with frequencies

$$\lambda_i = \lambda_m + 5F_\lambda, \quad \mu_i = \mu_m + 5F_\mu, \quad \nu_i = \nu_m + 3F_\nu.$$

In the simulations, the frequency separation of the two cisoids of interest are set to $\delta_\lambda = 0.5\,F_\lambda$, $\delta_\mu = 0.75\,F_\mu$, and $\delta_\nu = 0.5\,F_\nu$, respectively. Further the SNR is fixed to 10 dB and the SIR as in (3.48) is varied. The RMSE of Algorithm 4.1 and the additional bias correction are shown in Figure 4.6. Comparing the values to the ones obtained without interfering cisoid in Figure 4.4 we conclude that out-of-band interference has only a minor influence on Algorithm 4.1.
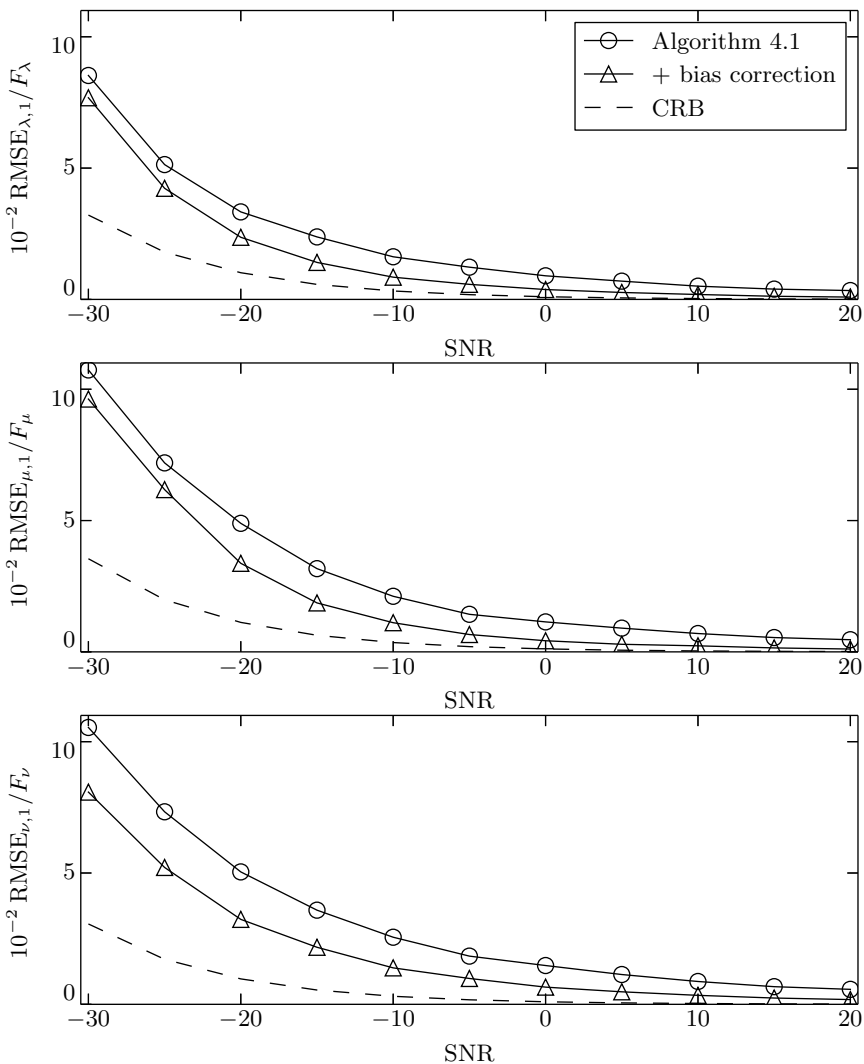
Figure 4.4: RMSE of the proposed single-cisoid search approach and bias correction for varying SNR.
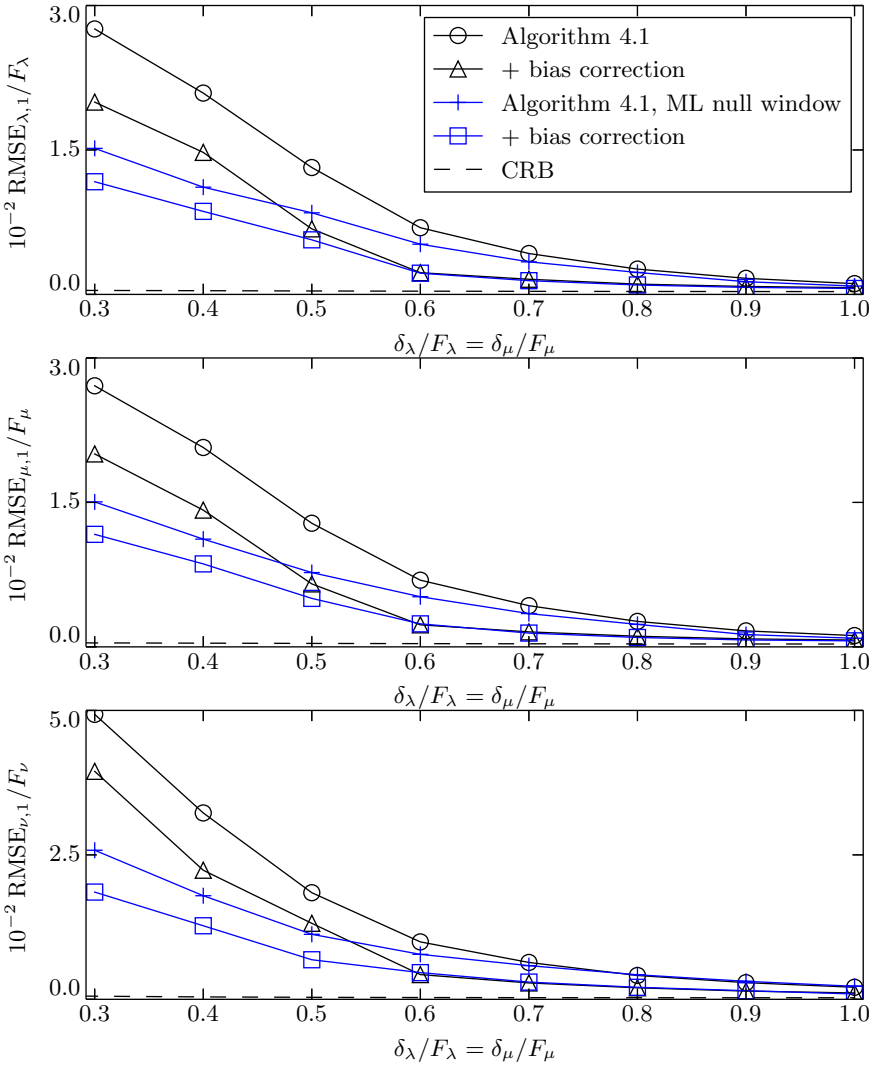
Figure 4.5: RMSE of the proposed single-cisoid search approach and bias correction for varying frequency separation in the remaining dimensions.
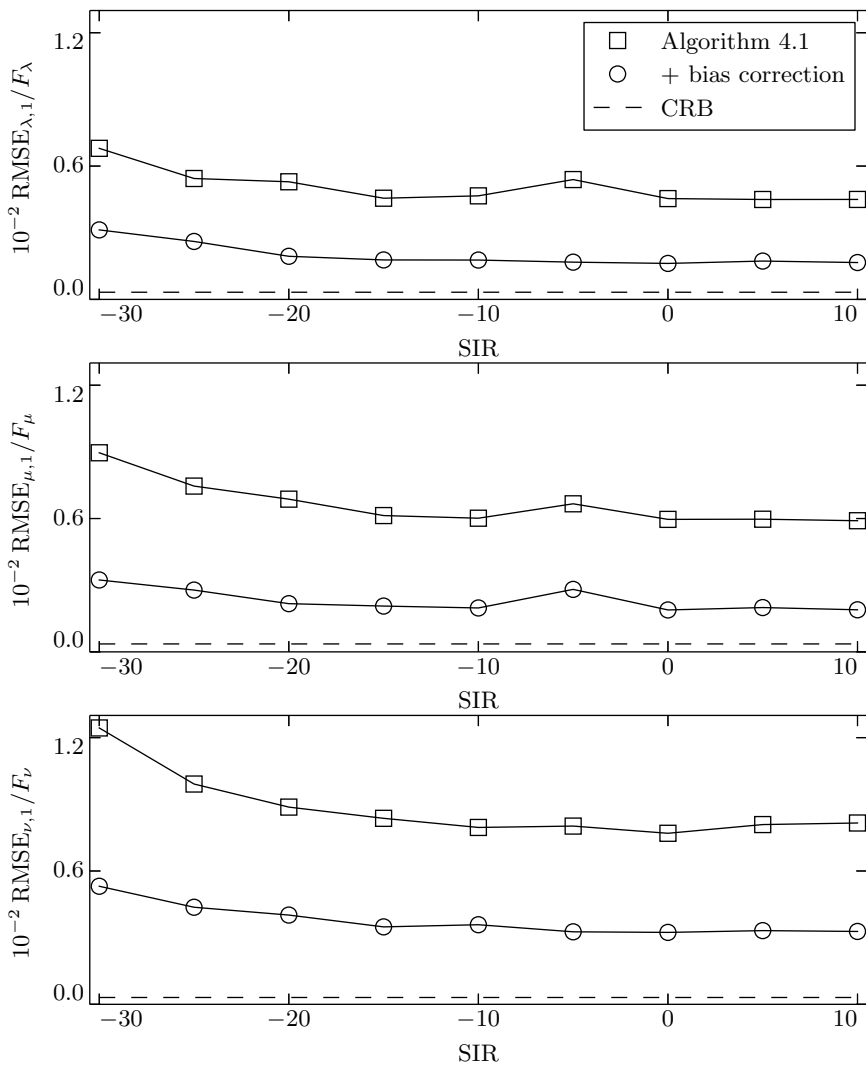
Figure 4.6: RMSE of the proposed single-cisoid search approach and bias correction-
for varying SIR.

4.A Appendix

4.A.1 Derivation of bias correction terms

Resolution dimension

We derive a small error approximation of the bias for the resolution dimension estimates. To this end, consider the derivative of (4.12) with respect to ν

$$\frac{\partial}{\partial\nu} P\left(\Delta_\lambda l_1, \Delta_\mu m_1, \nu\right) = \frac{\partial}{\partial\nu} |\alpha_{s,1}|^2 \Omega_\nu^2 \left(\nu - \nu_1\right) + e\left(\nu\right) \tag{4.26}$$

where

$$e\left(\nu\right) = 2|\alpha_{w,1}|^2 \dot{\Omega}_\nu \left(\nu - \nu_2\right) + 2\cos(\angle\alpha_{w,1}/\alpha_{s,1} + \delta_\nu (N_s - 1)/2)|\alpha_{s,1}||\alpha_{w,1}|$$
$$\cdot \left[\dot{\Omega}_\nu \left(\nu - \nu_1\right)\Omega_\nu \left(\nu - \nu_2\right) + \Omega_\nu \left(\nu - \nu_1\right)\dot{\Omega}_\nu \left(\nu - \nu_2\right)\right]$$

denotes an error term. For $|\alpha_{s,1}| \gg |\alpha_{w,1}|$, the error term and the derivative of $|\alpha_{s,1}|^2 \Omega_\nu^2 \left(\nu - \nu_1\right)$ can be approximated by a zeroth-order Taylor expansion

$$e\left(\nu\right) \approx -2\left[|\alpha_{w,1}|^2 + \cos(\angle\alpha_{w,1}/\alpha_{s,1} + \delta_\nu (N_s - 1)/2)|\alpha_{s,1}||\alpha_{w,1}|\right]\dot{\Omega}_\nu \left(\delta_\nu\right) \tag{4.27}$$

and a first-order Taylor expansion

$$\frac{\partial}{\partial\nu} |\alpha_{s,1}|^2 \Omega_\nu^2 \left(\nu - \nu_1\right) \approx 2|\alpha_{s,1}|^2 \ddot{\Omega}_\nu \left(0\right)\left(\nu - \nu_1\right) \tag{4.28}$$

around ν_1, respectively. Substituting (4.28) and (4.27) in (4.26) and letting $\nu = \hat{\nu}_1$ yields

$$\hat{\nu}_1 - \nu_1 = \left[\frac{|\alpha_{w,1}|^2}{|\alpha_{s,1}|^2} + \cos(\angle\alpha_{w,1}/\alpha_{s,1} + \delta_\nu (N_s - 1)/2)\frac{|\alpha_{w,1}|}{|\alpha_{s,1}|}\right]\frac{\dot{\Omega}_\nu \left(\delta_\nu\right)}{\ddot{\Omega}_\nu \left(0\right)}, \tag{4.29}$$

as the derivative of the periodogram is zero at its maximizing frequency $\hat{\nu}_1$. The same approach can be used for the second resolution dimension estimate, which yields

$$\hat{\nu}_2 - \nu_2 = -\left[\frac{|\alpha_{w,2}|^2}{|\alpha_{s,2}|^2} + \cos(\angle\alpha_{w,2}/\alpha_{s,2} - \delta_\nu (N_s - 1)/2)\frac{|\alpha_{w,2}|}{|\alpha_{s,2}|}\right]\frac{\dot{\Omega}_\nu \left(\delta_\nu\right)}{\ddot{\Omega}_\nu \left(0\right)}. \tag{4.30}$$

Substituting

$$\hat{\alpha}_{s,1} = \hat{a}_1\, W_\lambda\left(\Delta_\lambda l_1 - \hat{\lambda}_1\right) W_\mu\left(\Delta_\mu m_1 - \hat{\mu}_1\right),$$
$$\hat{\alpha}_{w,1} = \hat{a}_2\, W_\lambda\left(\Delta_\lambda l_1 - \hat{\lambda}_2\right) W_\mu\left(\Delta_\mu m_1 - \hat{\mu}_2\right),$$
$$\hat{\alpha}_{s,2} = \hat{a}_2\, W_\lambda\left(\Delta_\lambda l_2 - \hat{\lambda}_2\right) W_\mu\left(\Delta_\mu m_2 - \hat{\mu}_2\right),$$
$$\hat{\alpha}_{w,2} = \hat{a}_1\, W_\lambda\left(\Delta_\lambda l_2 - \hat{\lambda}_1\right) W_\mu\left(\Delta_\mu m_2 - \hat{\mu}_1\right),$$

$\hat{\lambda}_1$, $\hat{\lambda}_2$, $\hat{\mu}_1$, $\hat{\mu}_2$, $\hat{\delta}_\nu = \hat{\nu}_2 - \hat{\nu}_1$, $\hat{a}_1$, and $\hat{a}_2$ for the true values, yields estimators of the bias terms.

Remaining dimensions

Here, small-error approximations of the bias in the remaining dimensions are derived. To this end, consider the partial derivatives of (4.21) with respect to λ and μ

$$\frac{\partial}{\partial\lambda}|\hat{\alpha}_1(\lambda,\mu)|^2 = \frac{1}{|d|^2}\left[|s_1|^2\frac{\partial}{\partial\lambda}|\alpha_1(\lambda,\mu)|^2 + e_\lambda(\lambda,\mu)\right], \qquad (4.31)$$

$$\frac{\partial}{\partial\mu}|\hat{\alpha}_1(\lambda,\mu)|^2 = \frac{1}{|d|^2}\left[|s_1|^2\frac{\partial}{\partial\mu}|\alpha_1(\lambda,\mu)|^2 + e_\mu(\lambda,\mu)\right], \qquad (4.32)$$

where

$$\begin{aligned}
e_\lambda(\lambda,\mu) &= |r_1|^2|a_2|^2\dot{\Omega}_\lambda^2(\lambda-\lambda_2)\,\Omega_\mu^2(\mu-\mu_2)\\
&\quad + 2|a_1||a_2||s_1||r_1|\cos(\phi_1)\,\Omega_\mu(\mu-\mu_1)\,\Omega_\mu(\mu-\mu_2)\\
&\quad \cdot\left[\dot{\Omega}_\lambda(\lambda-\lambda_1)\,\Omega_\lambda(\lambda-\lambda_2) + \Omega_\lambda(\lambda-\lambda_1)\,\dot{\Omega}_\lambda(\lambda-\lambda_2)\right],\\
e_\mu(\lambda,\mu) &= |r_1|^2|a_2|^2\Omega_\lambda^2(\lambda-\lambda_2)\,\dot{\Omega}_\mu^2(\mu-\mu_2)\\
&\quad + 2|a_1||a_2||s_1||r_1|\cos(\phi_1)\,\Omega_\lambda(\lambda-\lambda_1)\,\Omega_\lambda(\lambda-\lambda_2)\\
&\quad \cdot\left[\dot{\Omega}_\mu(\mu-\mu_1)\,\Omega_\mu(\mu-\mu_2) + \Omega_\mu(\mu-\mu_1)\,\dot{\Omega}_\mu(\mu-\mu_2)\right],
\end{aligned}$$

denote respective error terms. For $|s_1| \gg |r_1|$, the error terms and the partial derivatives of $|\alpha_1(\lambda,\mu)|^2$ can be approximated by a zeroth-order Taylor expansion around λ_1, μ_1

$$e_\lambda(\lambda,\mu) \approx -2\left[|r_1|^2|a_2|^2\Omega_\mu^2(\delta_\mu) + |a_1||a_2||s_1||r_1|\Omega_\mu(\delta_\mu)\cos(\phi_1)\right]\dot{\Omega}_\lambda(\delta_\lambda), \quad (4.33)$$

$$e_\mu(\lambda,\mu) \approx -2\left[|r_1|^2|a_2|^2\Omega_\lambda^2(\delta_\lambda) + |a_1||a_2||s_1||r_1|\Omega_\lambda(\delta_\lambda)\cos(\phi_1)\right]\dot{\Omega}_\mu(\delta_\mu), \quad (4.34)$$

and by a first-order Taylor expansion around λ_1, μ_1

$$\frac{\partial}{\partial\lambda}|\alpha_1(\lambda,\mu)|^2 \approx 2|a_1|^2\ddot{\Omega}_\lambda(0)(\lambda-\lambda_1), \qquad (4.35)$$

$$\frac{\partial}{\partial\mu}|\alpha_1(\lambda,\mu)|^2 \approx 2|a_1|^2\ddot{\Omega}_\mu(0)(\mu-\mu_1), \qquad (4.36)$$

respectively. Substituting (4.33), (4.35) and (4.34), (4.36) in (4.31), (4.32), respectively, and considering that the periodograms partial derivatives of $|\hat{\alpha}_1(\lambda,\mu)|^2$ are zero at $\hat{\lambda}_1$ and $\hat{\mu}_1$, respectively, yields

$$\underbrace{\hat{\lambda}_1 - \lambda_1}_{\beta_{\lambda,1}} = \left[\frac{|r_1|^2}{|s_1|^2}\frac{|a_2|^2}{|a_1|^2}\Omega_\mu^2(\delta_\mu) + \frac{|r_1|}{|s_1|}\frac{|a_2|}{|a_1|}\Omega_\mu(\delta_\mu)\cos(\phi_1)\right]\frac{\dot{\Omega}_\lambda(\delta_\lambda)}{\ddot{\Omega}_\lambda(0)}, \quad (4.37)$$

$$\underbrace{\hat{\mu}_1 - \mu_1}_{\beta_{\mu,1}} = \left[\frac{|r_1|^2}{|s_1|^2}\frac{|a_2|^2}{|a_1|^2}\Omega_\lambda^2(\delta_\lambda) + \frac{|r_1|}{|s_1|}\frac{|a_2|}{|a_1|}\Omega_\lambda(\delta_\lambda)\cos(\phi_1)\right]\frac{\dot{\Omega}_\mu(\delta_\mu)}{\ddot{\Omega}_\mu(0)}. \quad (4.38)$$

Bias terms for the second cisoid are obtained analogously

$$\underbrace{\hat{\lambda}_2 - \lambda_2}_{\beta_{\lambda,2}} = -\left[\frac{|r_2|^2}{|s_2|^2}\frac{|a_1|^2}{|a_2|^2}\,\Omega_\mu^2\left(\delta_\mu\right) + \frac{|r_2|}{|s_2|}\frac{|a_1|}{|a_2|}\Omega_\mu\left(\delta_\mu\right)\cos\left(\phi_2\right)\right]\frac{\dot{\Omega}_\lambda\left(\delta_\lambda\right)}{\ddot{\Omega}_\lambda\left(0\right)}, \quad (4.39)$$

$$\underbrace{\hat{\mu}_2 - \mu_2}_{\beta_{\mu,2}} = -\left[\frac{|r_2|^2}{|s_2|^2}\frac{|a_1|^2}{|a_2|^2}\,\Omega_\lambda^2\left(\delta_\lambda\right) + \frac{|r_2|}{|s_2|}\frac{|a_1|}{|a_2|}\Omega_\lambda\left(\delta_\lambda\right)\cos\left(\phi_2\right)\right]\frac{\dot{\Omega}_\mu\left(\delta_\mu\right)}{\ddot{\Omega}_\mu\left(0\right)}. \quad (4.40)$$

where $\phi_2 = \angle r_2 - \angle s_2 - \varphi - \delta_\lambda(L_s - 1)/2 - \delta_\mu(M_s - 1)/2$. Substituting

$$\nu_1 = \hat{\nu}_1 - \hat{\beta}_{\nu,1}, \quad \nu_2 = \hat{\nu}_2 - \hat{\beta}_{\nu,2},$$

in (4.17), (4.18), (4.19), (4.20), yields estimates of s_1, r_1, s_2, and r_2, respectively. Substituting these and estimates of a_1, a_2, δ_ρ, and δ_μ in (4.37), (4.38), (4.39), and (4.40), respectively, yields estimators of the bias terms.

5 Automotive radar

In this chapter, we consider applications of multidimensional frequency estimation in automotive radar and focus on computational efficiency, memory efficiency, and high-resolution capability. The framework on multidimensional frequency estimation, developed in Chapter 3, is applied and the single-cisoid search frequency estimation, presented in Chapter 4, is used to reduce computational complexity. The effectiveness of this approach is demonstrated using measurements obtained with a series-production automotive radar.

The remainder of this chapter is organized as follows. In Section 5.1, an overview of automotive radar applications is given, classical radar processing steps are sketched, state-of-the-art automotive radar sensors are discussed, and a corresponding data model is derived. In Section 5.2, conventional automotive signal processing is considered, which achieves computational and memory efficiency but lacks high-resolution capability. Radar system design aspects are discussed in Section 5.3, where the focus is on trading off resolution for ambiguity. Section 5.4 constitutes the main contribution of this chapter, that is adding high-resolution capability to the conventional processing considered in Section 5.2.

5.1 Preliminaries

5.1.1 Automotive radar background

Radar is one of the main technologies for target localization in ADAS [BDF+14] and has some unique advantages compared to lidar and camera technologies. Radar works reliably in bad weather and lighting conditions, provides direct measurements of range, radial velocity, and direction of multiple targets, and has a high range coverage of more than 200 m. Current radar-based ADAS are adaptive cruise control (ACC) [Win12], lane change assist (LCA) [BMS12], forward collision avoidance (FCA) [Mau12], and evasion assist [DDF+12]. One of the most dynamic topics in the automotive industry is the development of ADAS towards HAD, for which radar is considered as one of the key technologies [DAB+14, DAK+15, WM14].

Classical radar pre-processing consists of matched filtering, Doppler processing, and digital beamforming. State-of-the-art automotive radars employ stretch processing and uniform linear arrays (ULA), so that classical pre-processing can be replaced

by a 3-D Fourier transformation. Further processing steps are power detection, parameter estimation, clustering of detections, target tracking, and, optionally, target classification, road estimation, or occupancy-grid-map methods to determine the stationary environment of the radar. The focus here is on target parameter estimation in particular with high-resolution capability. The remaining processing steps are discussed extensively in the literature. Target tracking and clustering is discussed in [Büh08, GSDB07, HSSS12, HLS12], target classification in [Heu13], road estimation in [GHFS14], and occupancy grid map methods in [LHG11, LSG12].

Current limitations with respect to requirements of the automotive industry are limited spatial and radial velocity resolution in particular for HAD [MBF+13, DKH+15]. Range resolution is typically limited by bandwidth, radial velocity resolution by coherent processing time, and angular resolution by antenna aperture and number of receive (Rx) channels. For ADAS and HAD, increasing bandwidth, coherent processing time, antenna aperture and number of Rx channels is often not practical due to cost, size, and processing time constraints. To nevertheless meet resolution requirements, high-resolution frequency estimation can be used. Existing approaches for automotive radar consider high-resolution techniques in the spatial dimension, that is the original domain of the angular dimension. In [Sch10] a comparative study of such techniques is provided for frequency modulated continues wave (FMCW) radars, whereas in [Hei12] computationally efficient high-resolution methods for state-of-the-art chirp-sequence radars are considered.

5.1.2 Radar principles

Radars transmit electromagnetic (EM) waves via a transmit (Tx) antenna and receive target echoes back via an Rx antenna to determine relevant targets. The temporal variation of the transmitted wave is called waveform and is generated by exciting a Tx antenna with a time varying current or voltage, which is here collectively referred to as signal. Tx signals used in radar are bandpass signals, which are effectively bandlimited around a carrier frequency f_c and can be expressed as

$$s(t) = a_e(t) \cos[2\pi\varphi(t)],$$

where $a_e(t) > 0$ is the envelope, $\varphi(t) = f_c t + \varphi_m(t)$ the instantaneous phase, and $\varphi_m(t)$ the instantaneous phase modulation. An important signal representation is

$$s(t) = \text{Re}\{\tilde{s}(t)e^{j2\pi f_c t}\}, \quad \tilde{s}(t) = a_e(t)e^{j2\pi\varphi_m(t)}$$

where $\tilde{s}(t)$ is the complex envelope of the Tx signal. Examples of bandpass signals are continuous wave signals $\cos[2\pi f_c t]$ and unmodulated pulses $\Pi[t/t_p] \cos[2\pi f_c t]$, where t_p is the pulse duration and $\Pi[\cdot]$ is the rectangular function.

Exciting an antenna with a bandpass signal creates a propagating EM wave. If the antenna characteristics do not change significantly around the carrier frequency, the

corresponding waveform is determined by the bandpass signal. Consider, that the Tx wave hits a point target at position $\mathbf{p}$, which scatters the waves energy spherically. If the scattering process is frequency independent around the carrier frequency, the waveform of the scattered wave is the Tx signal shifted by the so-called propagation delay $|\mathbf{p} - \mathbf{p}_{\mathrm{Tx}}|/c$, where $\mathbf{p}_{\mathrm{Tx}}$ is the Tx antenna position and c the propagation velocity. The amplitude and polarization of the scattered wave are on the one hand determined by the incoming wave, that is by the gain, directivity, and polarization of the Tx antenna and a spherical spreading factor $1/|\mathbf{p} - \mathbf{p}_{\mathrm{Tx}}|$. On the other hand, by the scattering characteristics of the point target, which are described by the polarization scattering matrix [KST93].

The scattered wave can be received by the Rx antenna of the radar. The field at the Rx antenna position $\mathbf{p}_{\mathrm{Rx}}$ is the scattered field at the point target position with an additional propagation delay $|\mathbf{p} - \mathbf{p}_{\mathrm{Rx}}|/c$ and spherical spreading $1/|\mathbf{p} - \mathbf{p}_{\mathrm{Rx}}|$. The Rx antenna transforms that field back to a signal

$$s_{\mathrm{Rx}}(t) = \frac{A_s}{|\mathbf{p} - \mathbf{p}_{\mathrm{Tx}}||\mathbf{p} - \mathbf{p}_{\mathrm{Rx}}|} \, s\left(t - \frac{|\mathbf{p} - \mathbf{p}_{\mathrm{Tx}}|}{c} - \frac{|\mathbf{p} - \mathbf{p}_{\mathrm{Rx}}|}{c} - \frac{\phi_s}{2\pi f_c}\right), \qquad (5.1)$$

where the amplitude A_s and phase ϕ_s depend on the scattering characteristics of the point target and on the gain, directivity, and polarization of the Tx and Rx antennas. For $r = |\mathbf{p}| \gg |\mathbf{p}_{\mathrm{Tx}}|$ and $r \gg |\mathbf{p}_{\mathrm{Rx}}|$, (5.1) can be simplified by using the so-called far-field approximation

$$|\mathbf{p} - \mathbf{p}_{\mathrm{Tx}}| = r - \mathbf{d}^{\mathrm{T}}\mathbf{p}_{\mathrm{Tx}} + O\left(\frac{|\mathbf{p}_{\mathrm{Tx}}|}{r}\right)$$

$$\approx \begin{cases} r, & \text{for amplitude terms} \\ r - \mathbf{d}^{\mathrm{T}}\mathbf{p}_{\mathrm{Tx}}, & \text{for delay terms} \end{cases} \qquad (5.2)$$

$$|\mathbf{p} - \mathbf{p}_{\mathrm{Rx}}| = r - \mathbf{d}^{\mathrm{T}}\mathbf{p}_{\mathrm{Rx}} + O\left(\frac{|\mathbf{p}_{\mathrm{Rx}}|}{r}\right)$$

$$\approx \begin{cases} r, & \text{for amplitude terms} \\ r - \mathbf{d}^{\mathrm{T}}\mathbf{p}_{\mathrm{Rx}}, & \text{for delay terms} \end{cases} \qquad (5.3)$$

Substituting (5.2) and (5.3) in (5.1) yields

$$s_{\mathrm{Rx}}(t) = A \, s(t - \tau),$$

where $\tau = (2r - \mathbf{d}^{\mathrm{T}}\mathbf{p}_{\mathrm{Rx}})/c$ and $A = A_s/r^2$. Note that we neglected delay terms, which are much smaller than $2r/c$ and not needed for the further discussion. For the practically relevant case of relative motion between target and radar, consider a purely radial target motion $r(t) = r + vt$. Depending on the sign of v, this leads to a stretched or compressed Rx signal

$$s_{\mathrm{Rx}}(t) = \frac{A_s}{(r + vt)^2} \, s\left(\underbrace{\left[1 - \frac{2v}{c}\right]}_{\beta}\left[t - \frac{1}{c - 2v}(2r - \mathbf{d}^{\mathrm{T}}\mathbf{p}_{\mathrm{Rx}})\right]\right) \approx A \, s(\beta[t - \tau]).$$

To extract range r, radial velocity v, and direction $\mathbf{d}$ from that Rx signal, consider multiple, spatially distributed Rx antennas, which are collectively referred to as Rx antenna array. Each Rx antenna signal is processed in a separate IQ demodulator, which yields the complex envelope of the Rx signal of antenna n

$$A\,\tilde{s}(t - 2r/c)\,e^{-j4\pi\kappa vt}\,e^{j2\pi\kappa \mathbf{d}^{\mathrm{T}}\mathbf{p}_n}, \tag{5.4}$$

where $\mathbf{p}_n$ is the antenna position, $\kappa = f_c/c$ is the wavenumber, and a factor $e^{-j4\pi\kappa r}$ is included in A. Due to the structure of (5.4), range r and radial velocity v can be obtained by feeding (5.4) in a matched filter bank per Rx channel [LE04]. Based on the matched filter bank outputs, target direction $\mathbf{d}$ can be obtained via spatial filtering [VVB88]. This is also known as beamforming, which consists of finding the unknown target direction as the maximizer of

$$\frac{1}{N_s}\left|\sum_{n=0}^{N_s-1} x(n)e^{-j2\pi\kappa \mathbf{d}^{\mathrm{T}}\mathbf{p}_n}\right|^2, \tag{5.5}$$

where $x(n)$ is the output of matched filter bank n. A practically important array geometry is the ULA, which consists of equally spaced and linearly aligned Rx antennas. Considering the coordinate system in Figure 5.1, the position of ULA antenna n is $\mathbf{p}_n = [0, dn, 0]^{\mathrm{T}}$, where d is the antenna spacing. For target positions approximately in the xy-plane, the target direction can be approximated as $\mathbf{d} \approx [0, \sin(\phi), 0]^{\mathrm{T}}$, which yields $\mathbf{d}^{\mathrm{T}}\mathbf{p}_n = \sin(\phi)dn$ for the ULA. Substituting this in (5.5), shows that the beamformer criterion is the periodogram evaluated for the spatial frequency ν

$$\frac{1}{N_s}\left|\sum_{n=0}^{N_s-1} x(n)e^{-j\nu n}\right|^2, \quad \nu = 2\pi\kappa d\sin(\phi). \tag{5.6}$$

More generally, direction finding is equivalent to spatial frequency estimation if an ULA is employed [vT02].

Resolution for beamforming is determined by the mainlobe width of the so-called beampattern, which is obtained by substituting $x(n) = 1$ in (5.5) and evaluating it for all possible directions. Higher directional resolution can be achieved by advanced array processing [KV96]. Range and radial velocity resolution obtained with matched filtering is determined by the employed Tx signal [LE04]. For the basic unmodulated pulse the range resolution is $ct_p/2$ and the radial velocity resolution $1/(2\kappa t_p)$. Key concepts for increasing range and radial velocity resolution with respect to the unmodulated pulse, are pulse compression and coherent pulse trains, respectively [Rih69]. Pulse compression increases range resolution by modulating the instantaneous signal phase while keeping the pulse duration fixed. An important example is the linear frequency modulated (LFM) pulse, for which the instantaneous frequency is varied linearly during the pulse duration, where the bandwidth B is covered. For large time-bandwidth products $Bt_p \gg 1$, the achievable range resolution
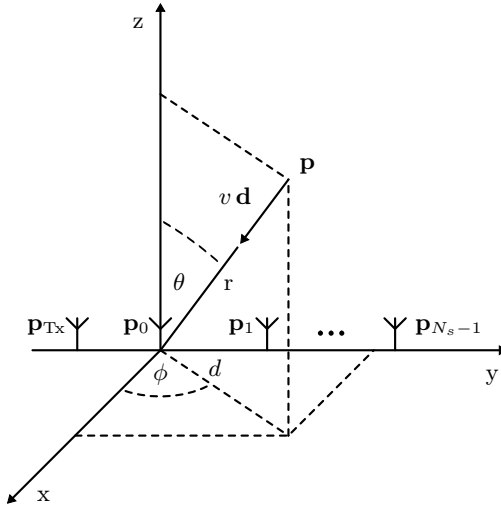
Figure 5.1: Coordinate system with ULA antennas and point target parameters.

for a LFM pulse is $c/(2B)$. Coherent pulse trains comprise M_s identical pulses transmitted at multiples of the pulse repetition time $t_r > t_p$ and thus achieve a radial velocity resolution of $1/(2\kappa M_s t_r)$ A common approach for implementing a matched filter bank for a coherent pulse train, is a zero-velocity filter per pulse, followed by an FFT over all filter outputs [LE04].

The combination of LFM pulse compression with coherent pulse trains

$$\sum_{m=0}^{M_s-1} \Pi \left[\frac{t - t_r m}{t_p} \right] \cos \left[2\pi \varphi \left(t - t_r m \right) \right], \quad \varphi \left(t \right) = f_c t + \frac{B}{2t_p} t^2, \tag{5.7}$$

constitutes one of the most popular waveforms in airborne radar [LE04] and is also known as chirp sequence in automotive radar [Kro14]. The Rx signal for the chirp sequence is

$$s_{\mathrm{Rx}}^{(n)}(t) = \sum_{m=0}^{M_s-1} \Pi \left[\beta \frac{t - t_r m - \tau_{m,n}}{t_p} \right] \cos \left[2\pi \varphi \left(\beta [t - t_r m - \tau_{m,n}] \right) \right], \tag{5.8}$$

where the instantaneous phase $\varphi(t)$ is given in (5.7),

$$\tau_{m,n} = (2r + 2vt_r m - \mathbf{d}^{\mathrm{T}} \mathbf{p}_n)/c \tag{5.9}$$

and $\beta = 1 - 2v/c$.

5.1.3 State-of-the-art automotive radar

State-of-the-art automotive radars use ULAs and chirp-sequence modulation [RA13, Kro14, Win15] to determine relevant targets and provide range, radial velocity, and direction resolution capability. A popular and much simpler alternative to chirp-sequence modulation is FMCW modulation. However, due to strongly coupled range and radial velocity measurements, FMCW modulation provides only range resolution capability [Win07] and is thus not considered here.

Chirp-sequence receivers used in automotive radar differ from the classical matched-filter receiver discussed in the previous section [Win15]. To understand this, recall that matched-filter range resolution is inversely proportional to bandwidth for a chirp or LFM pulse. To meet range-resolution requirements, bandwidth values from 200 MHz up to 2 GHz are used in automotive radar. The corresponding sampling rates lead to a dynamic range, power consumption, and cost of employed analog-to-digital converters, which are not practical. To cope with high-bandwidth values, stretch processing directly mixes the Rx antenna signal with the Tx signal in the high-frequency domain. After filtering, the resulting baseband signal has a constant frequency, proportional to range, which can be extracted via frequency estimation techniques. The required sampling rate is thus drastically reduced, while the available range resolution is the same as for matched filtering [KB13]. Stretch processing was first proposed in [Cap71] and is since then popular for high-range-resolution applications such as synthetic aperture radar, where it is also known as dechirp-on-receive processing.

5.1.3.1 Data model

Here, the data model for a multi-channel, chirp-sequence stretch receiver shown in Figure 5.2 is derived. The chirp sequence in (5.7) is generated by a controlled high-frequency oscillator and transmitted via the Tx antenna. The signal at Rx antenna n is given in (5.8) and is mixed with the Tx signal. The resulting baseband signal has a constant frequency and is sampled synchronized to the Tx signal. Gathering the samples for all Rx channels and chirps yields a 3-D data set for which a model is derived next.

Consider the mixer output signal first, that is the product of the Rx and Tx signal. It can be split in the baseband signal

$$s_{\mathrm{B}}^{(n)}(t) = \sum_{m=0}^{M_s-1} \Pi\left[\frac{t - t_r m - \tau_0}{t_p - \tau_0}\right] A\cos\left[2\pi\varphi\left(\beta\left[t - t_r m - \tau_{m,n}\right]\right) - 2\pi\varphi\left(t - t_r m\right)\right]$$

$$(5.10)$$

and a high frequency signal which is removed by filtering, as shown in Figure 5.2. Note that a delay τ_0 is introduced to ensure a complete overlap of the Tx and Rx
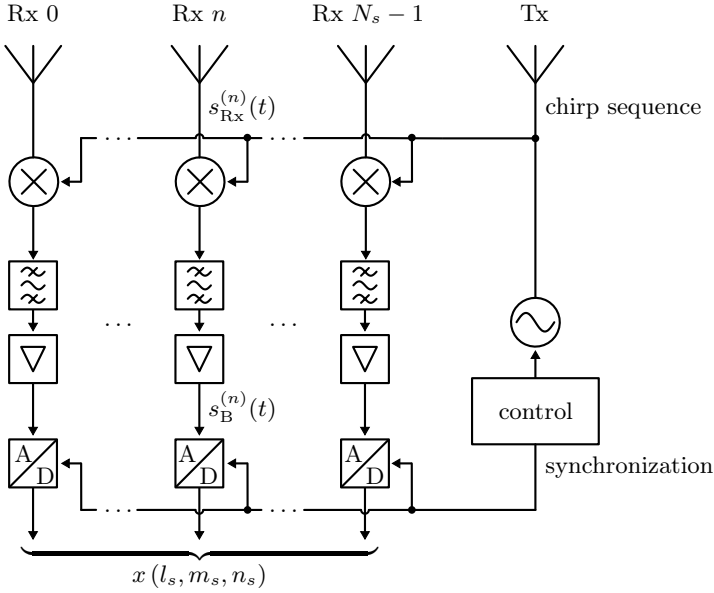
Figure 5.2: Multi-channel stretch receiver for a chirp sequence radar. Each Rx channel consists of a mixer, a filter, and an amplifier. Sampling the so obtained baseband signal synchronized to the Tx chirp sequence yields a 3-D set of samples.

signal and that the gain of the amplifiers and a factor of $1/2$ are absorbed in A. The phase of the baseband signal is

$$
\begin{aligned}
&\varphi\left(\beta\left[t - t_r m - \tau_{m,n}\right]\right) - \varphi\left(t - t_r m\right)\\
&= \frac{B}{2t_p}\left(\beta^2 - 1\right)\left(t - t_r m\right)^2 - \left[\frac{2v}{c}f_c + \frac{B\beta}{t_p}\tau_{m,n}\right]\left(t - t_r m\right) - f_c\tau_{m,n} + \frac{B}{2t_p}\tau_{m,n}^2\\
&\approx -\frac{B}{t_p}\tau_{m,n}(t - t_r m) - f_c\tau_{m,n} + \frac{B}{2t_p}\tau_{m,n}^2\\
&\approx -\frac{B}{t_p}\tau_{m,n}(t - t_r m) - f_c\tau_{m,n}\\
&\approx -\frac{B}{t_p}\frac{2r}{c}t - 2\kappa v t_r m - \kappa \mathbf{d}^{\mathrm{T}}\mathbf{p}_n - 2\kappa r
\end{aligned}
$$

Herein the first approximation is justified due to $c \gg v$ or equivalently $\beta \approx 1$, the second is based on $\tau_{m,n}f_c \gg \tau_{m,n}^2 B/(2t_p)$, and the last on $2r \gg 2vt_r m$ and the far-field assumption. Substituting this in (5.10) and considering $\mathbf{d}^{\mathrm{T}}\mathbf{p}_n = \sin(\phi)dn$

for the ULA yields

$$s_{\mathrm{B}}^{(n)}(t) \approx \sum_{m=0}^{M_s-1} \Pi \left[\frac{t - t_r m - \tau_0}{t_p - \tau_0} \right] A \cos \left[\frac{4\pi B}{t_p c} r(t - t_r m) + \mu m + \nu n + \varphi \right],$$

where $\mu = 4\pi \kappa t_r v$ is the normalized frequency associated with radial velocity, ν is the spatial frequency given in (5.6), and $\varphi = 4\pi \kappa r$ is a range dependent phase term. Sampling the baseband signal per pulse and arranging the samples in a 3-D array yields

$$\begin{aligned} x(l_s, m_s, n_s) &= s_{\mathrm{B}}^{(n_s)}(t_s l_s + t_r m_s + \tau_0) \\ &= A \cos(\lambda l_s + \mu m_s + \nu n_s + \varphi), \end{aligned} \tag{5.11}$$

where $l_s = 0, \dots L_s - 1$, $m_s = 0, \dots M_s - 1$, $n_s = 0, \dots N_s - 1$, t_s is the sampling time per pulse, $\lambda = 4\pi B_e r/(cL_s)$ is the normalized frequency corresponding to range,

$$B_e = B \left[1 - \frac{\tau_0}{t_p} \right] \tag{5.12}$$

is the effective bandwidth during the sampling interval $t_p - \tau_0 = L_s t_s$, and a factor $4\pi B r \tau_0/(t_p c)$ has been absorbed in φ. The model in (5.11) represents a 3-D sinusoid, whose frequencies λ, μ, and ν are determined by range, radial velocity, and direction, respectively, where the latter is represented by the sine of the azimuth angle ϕ.

The model in (5.11) can be generalized by considering multiple targets and additive noise introduced in the radar receiver [Yeo08]

$$x(l_s, m_s, n_s) = \sum_{k=1}^{K_c} A_k \cos(\lambda_k l_s + \mu_k m_s + \nu_k n_s + \varphi_k) + \xi_r(l_s, m_s, n_s). \tag{5.13}$$

Herein, K_c is the number of point targets, A_k is the amplitude, $\varphi_k = 4\pi \kappa r_k + 4\pi B \tau_0 r_k/(t_p c)$ the phase, and

$$\lambda_k = \frac{4\pi B_e}{cL_s} r_k, \quad \mu_k = 4\pi \kappa t_r v_k, \quad \nu_k = 2\pi \kappa d \sin(\phi_k), \tag{5.14}$$

are the normalized frequencies associated with range r_k, radial velocity v_k, and angle ϕ_k of point target k. The noise term $\xi_r(l_s, m_s, n_s)$ is real valued and modelled as white and Gaussian distributed.

The model in (5.13) shows that range, radial velocity, and direction of multiple point targets can be obtained via 3-D frequency estimation, that is by estimating the frequencies in (5.14) from the 3-D samples in (5.13).

5.2 Processing sequence

This section discusses how range, radial velocity, and direction of multiple point targets can be obtained from the data samples (5.13) via 3-D frequency estimation. We present a practical processing sequence, which is in particular advantageous with respect to computational complexity and storage space, two key requirements in automotive radar.

Preprocessing is based on 3-D discrete-time Fourier transformation

$$
\begin{aligned}
&X\left(\lambda, \mu, \nu\right)\\
&= \sum_{l_s=0}^{L_s-1} \sum_{m_s=0}^{M_s-1} \sum_{n_s=0}^{N_s-1} w_\lambda(l_s)\, w_\mu(m_s)\, w_\nu(n_s)\, x\left(l_s, m_s, n_s\right)\, e^{-j(\lambda\, l_s + \mu\, m_s + \nu\, n_s)},
\end{aligned}\quad (5.15)
$$

where $w_\lambda(l_s)$, $w_\mu(m_s)$, $w_\nu(n_s)$ are window functions in the range, radial velocity, and angular dimension, respectively. A frequency discretization is given by the DFT, which is obtained by letting $\lambda = 2\pi/L_s$, $l = 0, \ldots, L_s - 1$, $\mu = 2\pi/M_s$, $m = 0, \ldots, m_s - 1$, $\nu = 2\pi/N_s$, $n = 0, \ldots, N_s - 1$, in (5.15), respectively. In practice, DFT calculation can be carried out by hardware-accelerated processors, which provide computationally efficient FFT implementations [SW14, NRY15, MSKB15]. To reduce the required storage space, relevant processing cells are selected via peak searching in the DFT-grid periodogram

$$
P(l, m, n) = \left| X\left(\frac{2\pi}{L_s} l, \frac{2\pi}{M_s} m, \frac{2\pi}{N_s} n \right) \right|^2 \quad (5.16)
$$

and stored for further processing. Note that compared to storing the complete FFT data set, the memory requirements are thus substantially reduced. Relevant processing cells are subsequently used for frequency estimation, which yields the corresponding target parameters, range, radial velocity, and angle, via (5.14)

$$
\hat{r}_k = \frac{c L_s \hat{\lambda}_k}{4\pi B_e}, \qquad \hat{v}_k = \frac{\hat{\mu}_k}{4\pi t_r \kappa}, \qquad \hat{\phi}_k = \arcsin\left(\frac{\hat{\nu}_k}{2\pi d\kappa} \right), \quad (5.17)
$$

where $\hat{\lambda}_k$, $\hat{\mu}_k$, and $\hat{\nu}_k$, are the frequencies estimated from peak k. In practice, frequency estimation and all subsequent processing steps, such as clustering and target tracking, can be implemented on a general-purpose (GP) processor. In this way, the next sample acquisition, 3-D FFT calculation, and peak detection can be carried out in parallel to processing the currently detected peaks.

Figure 5.3 summarizes the main steps of the presented processing sequence and shows their distribution on the FFT and GP processor. In the following, peak detection and conventional, periodogram-based frequency estimation are discussed in detail in Section 5.2.1 and Section 5.2.2, respectively.
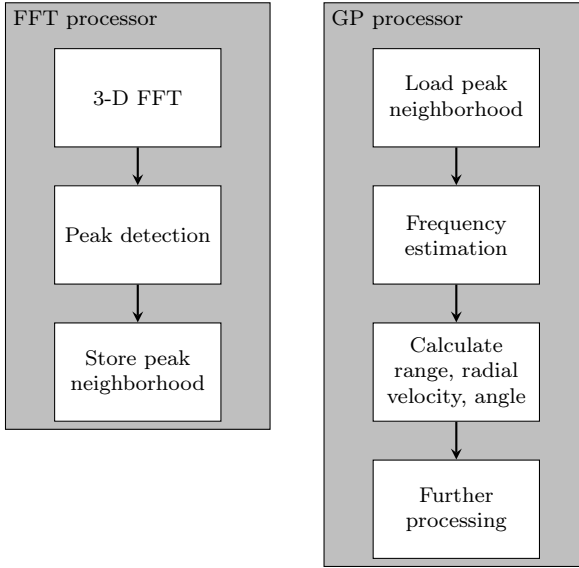
Figure 5.3: Practical processing sequence for state-of-the-art radars. Computational efficiency is achieved by using hardware-accelerated FFT processors and memory efficiency by storing only the neighborhood of detected peaks.

5.2.1 Peak detection

Periodogram peaks are obtained by searching local maxima of (5.16), that is values larger than their directly adjacent values. Computationally efficient implementation are again achieved via FFT processors, which also provide hardware-accelerated instructions for local maxima extraction [NRY15]. Relevant peaks are selected via power detection, that is by testing peak power values for being significantly larger than the noise power. To this end, an optimal threshold is $\ln(P_F)\,\sigma^2$, where $\ln(\cdot)$ is the natural logarithm, P_F is a desired false alarm probability and σ^2 is the noise power after Fourier transformation. For a derivation of that threshold see Appendix 5.A.1. To avoid false detections due to sidelobes of particularly strong peaks, a modified threshold value can be used

$$\max\left\{\ln(P_F)\,\sigma^2,\ \max_l \frac{P(l,m_k,n_k)}{\mathrm{SLL}_\lambda},\ \max_m \frac{P(l_k,m,n_k)}{\mathrm{SLL}_\mu},\ \max_n \frac{P(l_k,m_k,n)}{\mathrm{SLL}_\nu}\right\},$$

where l_k, m_k, n_k denote peak indices and SLL_λ, SLL_μ, and SLL_ν are defined in Appendix 2.A.1. To cope with time varying noise statistics, constant false alarm

rate (CFAR) techniques can be used, which estimate the noise power from the periodogram. An overview of different CFAR techniques is given in [RSH10, Ch. 16]. In particular, order-statistic CFAR techniques [Roh83] can be efficiently implemented [Win06]. To allow for local-interpolation refined periodogram methods, as discussed in Section 5.2.2, and for high-resolution frequency estimation, as presented in Section 5.4, not only the peak processing cells, but additional neighboring cells are stored.

5.2.2 Conventional parameter estimation

Conventionally, target parameters are obtained as the frequencies of detected peaks in (5.17), which is equivalent to the periodogram frequency estimator discussed in Section 2.2.2. Coarse frequency grids used in automotive radar lead to large estimation errors whenever the true frequencies do not coincide with a grid value. Local interpolation techniques, e.g. the popular parabolic interpolation discussed in Appendix 3.A.1 or the novel LUT approach developed in Section 3.3, use periodogram values in the peak neighborhood to reduce these errors.

The main advantage of periodogram-based target parameter estimation is low computational complexity, while its main drawback is limited resolution. The periodogram resolution limits (2.26) are straightforwardly translated to corresponding range, radial velocity, and angle resolution limits $\frac{c}{2B_e}$, $\frac{1}{2M_s t_r \kappa}$, arcsin $\frac{1}{N_s d \kappa}$, respectively. Note that range resolution is determined by the effective bandwidth B_e, radial velocity resolution by the coherent processing time $M_s t_r$, that is the overall duration of the chirp sequence, and angular resolution by the array aperture $N_s d$.

Practical system design, discussed in Section 5.3, chooses the effective bandwidth B_e, the number of chirps M_s, the pulse repetition time t_r, the number of Rx channels N_s, and the ULA antenna spacing d such that in most practical use-cases targets are separated by more than the resolution limit in either range, radial velocity, or angle. As an example consider stationary targets, e.g. guardrail poles or traffic signs, in a highway scene as shown at the left-hand side of Figure 5.4. Here, the majority of relevant targets can be resolved with conventional periodogram-based processing, when practical system parameters as in Table 5.2 are considered. For example, typical guardrail pole spacings exceed the range resolution limit of 0.75 m given in Table 5.2. On the right-hand side of Figure 5.4, the range and radial velocity frequencies of detected peaks are shown. Even for such a light traffic scenario, the number of peaks is large, more than 400, which supports the focus on computational efficiency in signal processing for automotive radars.

(a) Video image   (b) Detected peaks
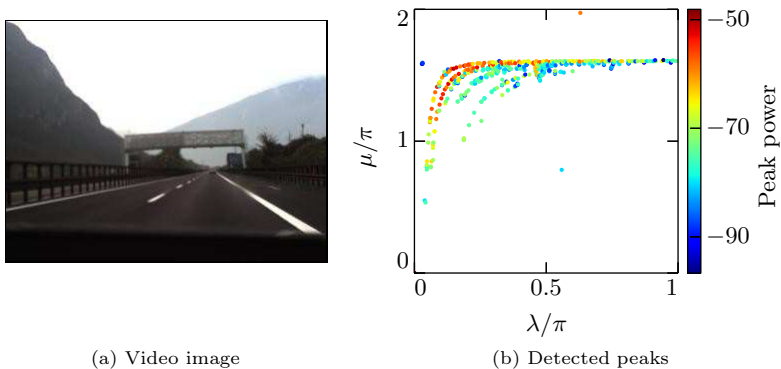
Figure 5.4: Data example obtained with a series production automotive radar in a light traffic scene (a). The large number of peaks (b) which have to be processed, support the focus on computational efficiency in automotive radar signal processing.

5.3 Practical system design

The main objectives in radar system design are high sensitivity and high resolution, where the focus here is on the latter. Recall that range resolution is determined by bandwidth B_e, radial velocity resolution by coherent processing time $M_s t_r$, and angular resolution by aperture $N_s d$. The number of pulses M_s and Rx channels N_s is in practice determined by memory limitations and hardware cost, respectively. Therefore, bandwidth B_e, pulse repetition time t_r, and antenna spacing d remain as actual design parameters. Choosing B_e, t_r, and d is a trade-off between resolution and ambiguities due to the mapping of range, radial velocity, and angle to normalized frequencies in (5.11). This can be seen in Table 5.1, where the resolution limits are shown together with the corresponding unambiguous intervals, obtained by substituting 2π for λ and $\pm\pi$ for μ and ν in (5.14). Observe that increasing B_e, t_r, and d increases resolution but decreases the unambiguous intervals.

Strategies to handle velocity ambiguity include variation of pulse repetition time between subsequent coherent processing intervals (CPI) [LE04, Sec. 8.3] and tracking of multiple velocity hypothesis [LHT+13]. Angular ambiguity can be resolved by adding an additional antenna pair with half wavelength spacing. The unambiguous angle obtained from the phase difference of such an antenna pair is then used to determine the correct angular hypothesis of the ULA based measurement. This is a common approach in multiple baseline interferometry [JR81].

Table 5.1: Resolution limits and unambiguous intervals.

	range	radial velocity	angle
Resolution limit	$\frac{c}{2B_e}$	$\frac{1}{2M_s t_r \kappa}$	$\arcsin \frac{1}{N_s d\kappa}$
Unambiguous interval	$\left(0, \frac{cL_s}{2B_e}\right)$	$\left(\frac{-1}{4\kappa t_r}, \frac{1}{4\kappa t_r}\right)$	$\left(\arcsin \frac{-1}{2\kappa d}, \arcsin \frac{1}{2\kappa d}\right)$

5.3.1 Series-production radar sensor

Here, a series-production automotive radar designed for ADAS applications such as FCA or ACC is considered. It employs state-of-the-art concepts, as discussed in Section 5.1.3, that is chirp-sequence modulation, stretch processing, and an ULA. Table 5.2 gathers relevant system parameters, resolution limits, as well as unambiguous parameter intervals. In the range and radial velocity dimensions, window functions with low SLL are used to prevent target masking. This will degrade the resolution capability predicted by the limits shown in Table 5.2 [Har78]. The unambiguous range of 384 m is larger than the maximal range of 250 m required for ADAS applications and therefore range ambiguities constitute no practical problem. In contrast, the unambiguous radial velocity and angle intervals are too small for typical ADAS use-cases, e.g. detection of stationary targets when the ego-vehicle is travelling with more than 30 m/s or detection of crossing targets at large angles.

To cope with velocity ambiguities, the pulse repetition time is varied on a CPI basis. Detections from subsequent CPIs are associated in range and angle and the corresponding velocity hypothesis are matched for both pulse repetition times. For details of that approach see [LE04, Sec. 8.3]. Angular ambiguities are resolved using the phase difference of an antenna pair, which provides unambiguous angle estimates within the field of view of the sensor. To this end, a particularly space-efficient array layout is used, which is shown in Figure 5.5. It consists of five microstrip patch array antennas (see Appendix 5.A.2 for details on microstrip antennas), where the first three comprise two serial-fed columns and the last two a single column. Each column comprises seven patches to obtain high elevation directivity. The spacing of the two single-column antennas equals the column spacing of the first three antennas. Their geometric center lies on the same grid, with spacing $d = 12.7$ mm, as the first three double-column antennas. Summing the Rx channels of the single-column antennas, yields an effective ULA, which can provide unambiguous angles within $(-9°, 9°)$. Due to the smaller spacing of the single-column antennas, their phase difference provides unambiguous angles within a much larger interval of $(-67°, 67°)$. This can be exploited to resolve the ambiguity of ULA-based estimates, by matching all possible angular hypothesis with the phase-difference-based estimates.

Table 5.2: System parameters for a series-production automotive radar.

Parameter	Symbol	Value
Center frequency	f_c	76.15 GHz
Number of samples per pulse	L_s	512
Number of pulses	M_s	256
Number of ULA antennas	N_s	4
Sampling time	t_s	100 ns
Pulse repetition time	t_r	90 µs
Antenna spacing	d	12.74 mm
Effective bandwidth	B_e	200 MHz
Window function (range)	w_λ	Chebyshev 60 dB SLL
Window function (radial velocity)	w_μ	Chebyshev 40 dB SLL
Window function (angle)	w_ν	rectangular
Resolution limit (range)		0.75 m
Resolution limit (radial velocity)		0.08 m/s
Resolution limit (angle)		4.4 °
Unambiguous interval (range)		$(0, 384\,\text{m})$
Unambiguous interval (radial velocity)		$(-11\,\text{m/s}, 11\,\text{m/s})$
Unambiguous interval (angle)		$(-9°, 9°)$

To implement such an approach, the processing sequence shown in Figure 5.3 is extended as shown in Figure 5.6. The 3-D FFT is now calculated in three steps, starting with a 2-D FFT in the range and radial velocity dimension. Subsequently channels three and four are summed and a 1-D FFT in the angular dimension is calculated. The result of the range-velocity FFT for channels three and four previous to the summation is stored for each detected peak and can be used on the GP processor to resolve the angular ambiguity of the ULA-based estimates.

The angular resolution capability of the discussed automotive radar needs to be assessed carefully. The natural approach of using the angular resolution limit in Table 5.1 falls short because of two reasons. First, angle estimation based on only two antennas fails for more than one target [vT02] and consequently the ambiguity of the ULA-based angle estimates can not be resolved by the above approach. Second, the effective angular separation is obtained after mapping angles to the unambiguous interval of the ULA. This means, angular separations above the resolution limit
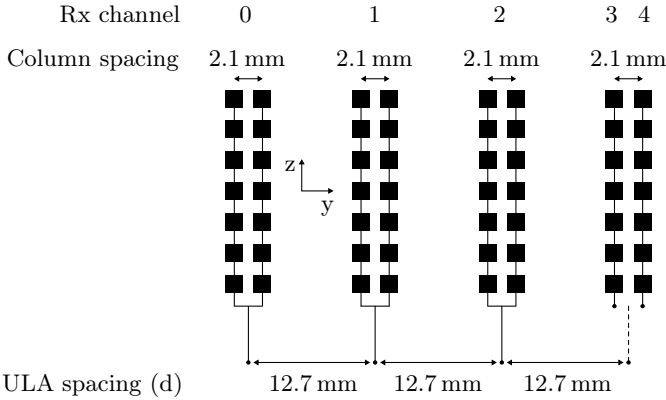
Figure 5.5: Rx antenna array with five channels, where the first three consist of double-column patch antennas and the last two of single-column ones. Summing channels three and four yields an effective ULA which can be used in conventional DFT-based processing. The ambiguity of ULA-based angle estimates can be resolved using the phase difference of channels three and four.

can fall below the resolution limit when mapped to $(-9°, 9°)$. Note that for large distances targets with angles outside $(-9°, 9°)$ are unlikely and only the central angular hypothesis needs to be considered.

5.4 High-resolution processing

In critical ADAS or HAD use-cases, e.g. as discussed in Section 5.4.1, relevant target pairs with range, radial velocity, and angular separations simultaneously below the corresponding resolution limits are possible. For practical automotive radars, e.g. as presented in Section 5.3, those can not be resolved by conventional periodogram-based processing and high-resolution methods become necessary. Other works in automotive radar focus on high-resolution methods in the spatial dimension, that is the original domain of the angular dimension [Sch10, Hei12]. However, we point out that, in critical use-cases, as discussed in Section 5.4.1, it can be advantageous to apply high-resolution methods also in the range and radial velocity dimension.

To this end, we apply the framework on multidimensional frequency estimation developed in Chapter 3, which we also consider in [EHZ+17]. This is discussed in Section 5.4.2, where Section 5.4.2.1 considers the single-cisoid search method, presented

| FFT processor	GP processor
2-D FFT range, velocity	Load peak neighborhood and Rx 3/4
Rx 3 + Rx 4	Frequency estimation
1-D FFT angle	Calculate range, radial velocity, angle
Peak detection	Resolve angular ambiguity
Store peak neighborhood and Rx 3/4	Further processing
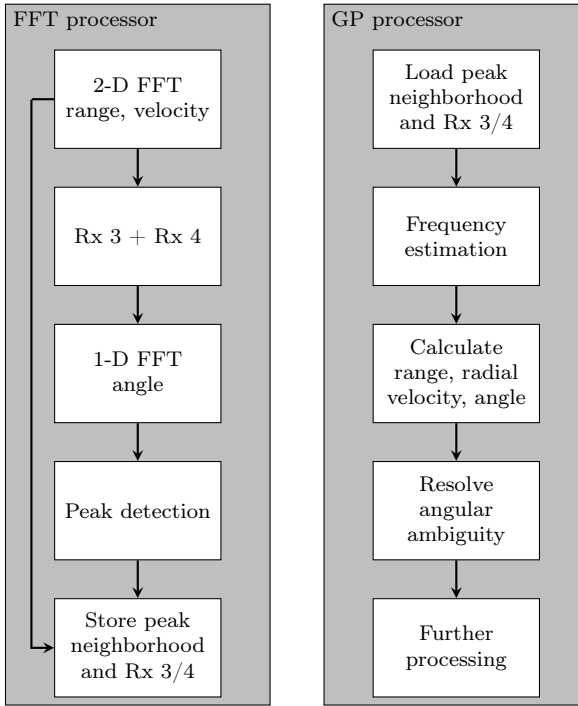
Figure 5.6: Extension of the processing sequence shown in Figure 5.3 for the antenna array shown in Figure 5.5. An effective ULA is obtained by summing channels three and four previous to calculating the angular FFT. Ambiguities of the ULA-based estimates can be resolved by using the phase difference of channels three and four after calculating the range-velocity FFT.

in Chapter 4, for further reducing computational complexity. The effectiveness of the proposed approaches is demonstrated in Section 5.4.3 using experimental results obtained with a series production automotive radar. For reference, high-resolution parameter estimation in the spatial dimension is outlined in Appendix 5.A.4.

5.4.1 Use cases

We motivate multidimensional high-resolution frequency estimation for automotive radar applications by considering two important use cases. First, scenarios involving specular multipath propagation are considered. Here, so-called mirror targets occur,
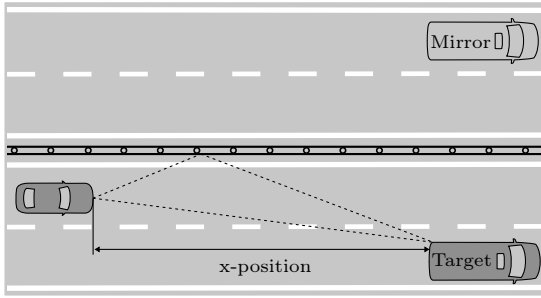
(a)
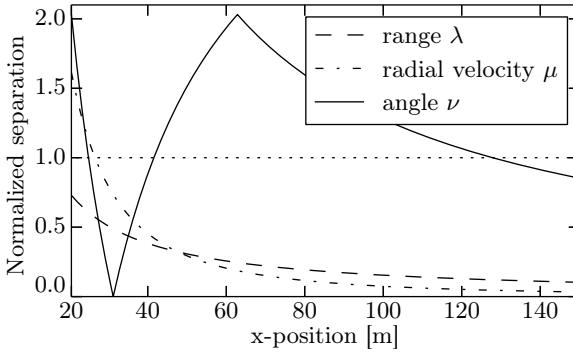
(b)

Figure 5.7: Specular multipath example leading to two targets in a practically relevant scenario for ACC or FCA (a) and corresponding normalized frequency separation (b). For the mapping of range, radial velocity, and angle to normalized frequencies, the radar system parameters in Table 5.2 are used.

which can have similar range, radial velocity, and angle as the corresponding actual targets. If mirror and actual targets are not resolved, merged peak detections occur, which can trigger erroneous system reactions, such as unjustified emergency braking. Second, scattering center extraction is considered, that is resolving different parts of the same large target such as a car. This enables target classification or even determining the shape and orientation of targets.

5.4.1.1 Specular multipath

Specular multipath propagation is the phenomenon of receiving target echoes not only directly, but also indirectly via specular reflection at other targets. This gives rise to mirror targets, which can be obtained geometrically by mirroring the actual target in the surface leading to the specular reflection. Practical examples are target cars mirrored in the road surface, guardrails, tunnel walls, or road works borders.

A typical scenario is shown in Figure 5.7 (a). Here, the subject, that is the radar-equipped vehicle, is travelling on the passing lane of a two-lane highway and is in the process of overtaking a slower target vehicle on the rightmost lane. The two driving directions are separated by a middle guardrail, which gives rise to specular multipath propagation. The direct and indirect propagation paths are shown as dashed lines and the position of the mirror target is indicated.

For calculating the range, radial velocity, and angular separations between the original target and the mirror target, we consider a lane width of 3.75 m, a subject vehicle speed of 100 kph, and a target vehicle speed of 80 kph. We map the parameter separation to normalized frequency separation using the system parameters, gathered in Table 5.2, of a typical series production automotive radar sensor. Figure 5.7 (b) shows the frequency separations normalized to the respective resolution limit over the relative x-position of the target. Note that the shape of the angular separation stems from the ambiguous mapping to normalized frequencies. Observe, that above 130 m and between 25 m and 42 m the frequency separation is below the respective resolution limit in all three dimensions, so that conventional periodogram-based processing will fail to resolve the original and mirror target. This can lead to misplaced target estimates in the driving path of the subject vehicle and may thus trigger erroneous ACC or FCA reactions such as deceleration or even unjustified emergency braking. This holds in particular for small x-positions in from 25 m to 42 m. In that region it will be advantageous to use either the range or the radial velocity dimension when applying high-resolution methods, due to their larger separation compared to the angular dimension.

5.4.1.2 Scattering center extraction

Electromagnetic scattering from targets, which are large with respect to a wavelength, is a superposition of local scattering hot spots known as scattering centers. Details can be found in Appendix 5.A.3. Extracting multiple scattering centers of the same target enables many advances in automotive radar, e.g. lateral velocity estimation [FR06], advanced target tracking [HSSS12], and target classification [Heu13]. Note that scattering center extraction was considered in [Eng14] for motivating multidimensional high-resolution frequency estimation.

(a)

(b)
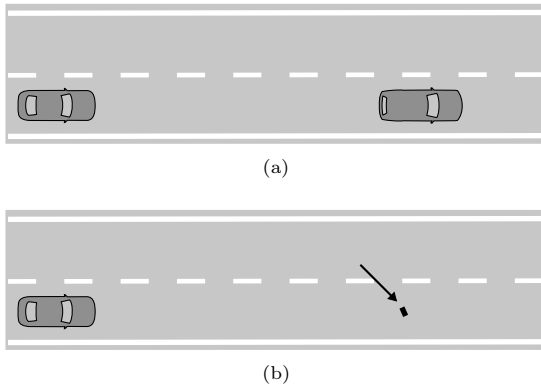
Figure 5.8: FCA example: the subject is approaching a stationary vehicle. In this case, emergency braking shall be performed (a). A small metallic object, e.g. a beverage can, shall not trigger emergency braking (b).

Here, we consider scattering center extraction for target classification, which serves as an important input to FCA for deciding if autonomous emergency braking shall be triggered. In Figure 5.8, two example scenarios are shown. The first comprises the subject vehicle, which is approaching another stationary car and the second consists of a small metallic object, e.g. a beverage can, in the driving path of the subject. Only in the first scenario emergency braking is justified. Here, correct target classification aids in taking the appropriate decision in both scenarios. A typical feature used for radar-based classification is the longitudinal target extension, which can be obtained from extracted scattering centers. The beverage can shows typically a single scattering center, while for the target car multiple, longitudinally displaced scattering centers can be obtained. To see this, consider Figure 5.9, which shows the propagation paths associated with two potential scattering centers. One at the rear end of the car and one at the cars rear axle, which the radar observes only indirectly via specular multipath involving the street surface. High-resolution methods applied to the range dimension can be used to resolve the two scattering centers, which are then used for feature calculation.

5.4.2 Proposed approach

A practical approach to obtain high-resolution capability in the range, radial velocity, and angle dimension is the framework on multidimensional frequency estimation proposed in Chapter 3. It can be straightforwardly incorporated in the processing sequence shown in Figure 5.3 by applying the processing steps shown in Figure 3.1 for
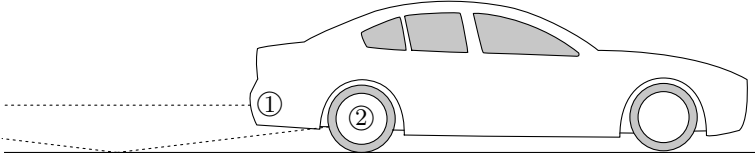
Figure 5.9: Propagation paths associated with two scattering centers: one at the rear end of the car (1) and one at the rear axle (2). The latter is only observed indirectly via the road surface.

each detected peak. To see this, we show that the local Fourier-domain models (3.1) and (3.2) apply directly to peak neighborhoods obtained according to Figure 5.3.

Substituting the baseband model in (5.13) in the 3-D DTFT in (5.15) and using

$$2\cos x = e^{jx} + e^{-jx}$$

yields

$$X\left(\lambda, \mu, \nu\right) = \sum_{k=1}^{K} a_k W_\lambda\left(\lambda - \lambda_k\right) W_\mu\left(\mu - \mu_k\right) W_\nu\left(\nu - \nu_k\right) +$$
$$\sum_{k=1}^{K} a_k^* W_\lambda\left(\lambda + \lambda_k\right) W_\mu\left(\mu + \mu_k\right) W_\nu\left(\nu + \nu_k\right) + \Xi_r(\lambda, \mu, \nu). \quad (5.18)$$

Herein, $W_\lambda\left(\lambda\right)$, $W_\mu\left(\mu\right)$, $W_\nu\left(\nu\right)$ are the Fourier-domain window functions given in (2.5), (2.6), (2.7), respectively, $a_k = \frac{A_k}{2} e^{j\varphi_k}$, and

$$\Xi_r\left(\lambda, \mu, \nu\right)$$
$$= \sum_{l_s=0}^{L_s-1} \sum_{m_s=0}^{M_s-1} \sum_{n_s=0}^{N_s-1} w_\lambda(l_s)\, w_\mu(m_s)\, w_\nu(m_s)\, \xi_r\left(l_s, m_s, n_s\right)\, e^{-j(\lambda\, l_s + \mu\, m_s + \nu\, n_s)}. \quad (5.19)$$

If frequencies in one dimension are restricted to $[0, \pi)$ and the target frequencies in that dimension lie in the same interval, the second term in (5.18) is on the order of the SLL of the corresponding Fourier-domain window function and can be neglected. If the frequency interval is further restricted to $(0, \pi)$, that is frequencies equal to zero are excluded, the noise term $\Xi_r(\lambda, \mu, \nu)$ is approximately circular symmetric with covariance given by (2.9) [Bri81, Ch.5]. In that case, the model in (5.18) can be approximated as

$$X\left(\lambda, \mu, \nu\right) \approx \underbrace{\sum_{k=1}^{K} a_k W_\lambda\left(\lambda - \lambda_k\right) W_\mu\left(\mu - \mu_k\right) W_\nu\left(\nu - \nu_k\right) + \Xi(\lambda, \mu, \nu)}_{\text{Model in (2.4)}}. \quad (5.20)$$

where $\lambda \in (0, \pi)$, $\mu \in [0, 2\pi)$, $\nu \in [0, 2\pi)$, and $\lambda_k \in (0, \pi)$.

The right-hand side of (5.20) is given by the model (2.4) considered in Chapter 3. Therefore, the framework on multidimensional frequency estimation, as shown in Figure 3.1, can be directly applied to peak neighborhoods obtained with the automotive radar processing sequence in Figure 5.3. In this way, high-resolution capability in the range, radial velocity, and angular dimension can be obtained and the memory efficiency of Fourier-based automotive radar processing can be retained. Computational efficiency is addressed by two approaches within the framework, as discussed in Chapter 3. The first is that computationally involved high-resolution methods are only applied to a subset of detected peaks, which most likely contain two targets. The second is decoupling the multidimensional frequency estimation problem into a sequence of computationally simpler 1-D problems.

Using that approach for the series production sensor presented in Section 5.3.1, yields ambiguous angle estimates due to the employed ULA spacing. However, high-resolution frequency estimates in either the range or the radial velocity dimension can be used to extract the corresponding signal components for Rx channels two and three, which are available when the processing sequence as in Figure 5.6 is used. The phase difference of the obtained signal components can be used for resolving the angular ambiguity of the corresponding high-resolution estimates.

5.4.2.1 Single-cisoid search pre-processing

Calculating 1-D high-resolution estimates in the resolution dimension constitutes the main computational burden of the proposed decoupled frequency estimation framework. In principle, single-cisoid search based frequency estimation, as proposed in Chapter 4, could be used, which is computational simpler than the NLS approach considered in the optimal framework. However, frequency separation in at least two dimensions are required, that is in the selected resolution dimension and in one of the remaining dimensions. Therefore, we combine single-cisoid search based frequency estimation and optimal NLS-based estimation sequentially as shown in Figure 5.10.

Here, the first processing steps, that is fitting the single-target model for the three possible decoupled models in the range, radial-velocity, or angle dimension, determining the resolution dimension, and two-target indication based on the fitting error in the resolution dimension, are retained as in the original framework shown in Figure 3.1. Subsequently, single-cisoid search based frequency estimation is performed and the resulting estimates are used for calculating the fitting error of the corresponding two-cisoid model. The fitting error is then to decide if the single-cisoid search result can be accepted or if optimal NLS-based frequency estimation shall be applied. In the latter case, further processing follows the original sequence in Figure 3.1, that

is the two-cisoid model is fitted based on the NLS-based frequency estimates and the corresponding fitting error is used to decide between the single-cisoid model and the two-cisoid model. For the latter, the remaining dimension frequencies are obtained as discussed in Section 3.4.2.

5.4.3 Experimental Results

We use experimental data of a series production automotive radar sensor to compare conventional radar processing, high-resolution frequency estimation in the spatial domain, and the proposed high-resolution frequency estimation in the Fourier domain with optimal selection of resolution dimension. Note that the radar system parameters are given in Table 5.2 and are thus the same as the ones considered in Section 5.4.1.

The experimental setup is designed such that resolution is the dominant influence on the target position estimates and detections can be straightforwardly associated to the targets of interest. To this end, corner reflectors are employed to obtain point-target radar responses. The radar sensor is kept stationary and the targets are moved towards the radar sensor to easily separate the targets from the environment, having a different relative velocity. Overall, this results in a clean two-target scenario without additional effects. Figure 5.11 (a) shows the experimental setup. The two corner reflectors are placed on a carrier, which allows for variable relative positioning. For the two experiments the corner reflectors are positioned such that either the angular or the range dimension has a significantly larger frequency separation than all others. The carrier is then moved straight towards the radar sensor at walking speed.

Figure 5.11 (b) shows the corresponding frequency separations normalized to the respective resolution limits. The radial velocity separation is very low and thus omitted. Observe that for the first experiment the frequency separation in the angular dimension is the largest, whereas for the second experiment the frequency separation in the range dimension is the largest. For all dimensions the separations are below the resolution limit except for x-positions below 18 m, where the angular separation exceeds the resolution limit for the first experiment. Therefore, we expect that conventional radar processing will fail for both experiments, except for x-positions below 18 m in the first experiment. For the first experiment we expect further that high-resolution processing in the spatial domain will perform well due to the dominating angular separation and that high-resolution processing in the Fourier domain selects the angular dimension as resolution dimension, leading to a similar performance. For the second experiment we expect, that high-resolution processing in the Fourier domain correctly selects the range dimension as resolution dimension and will thus
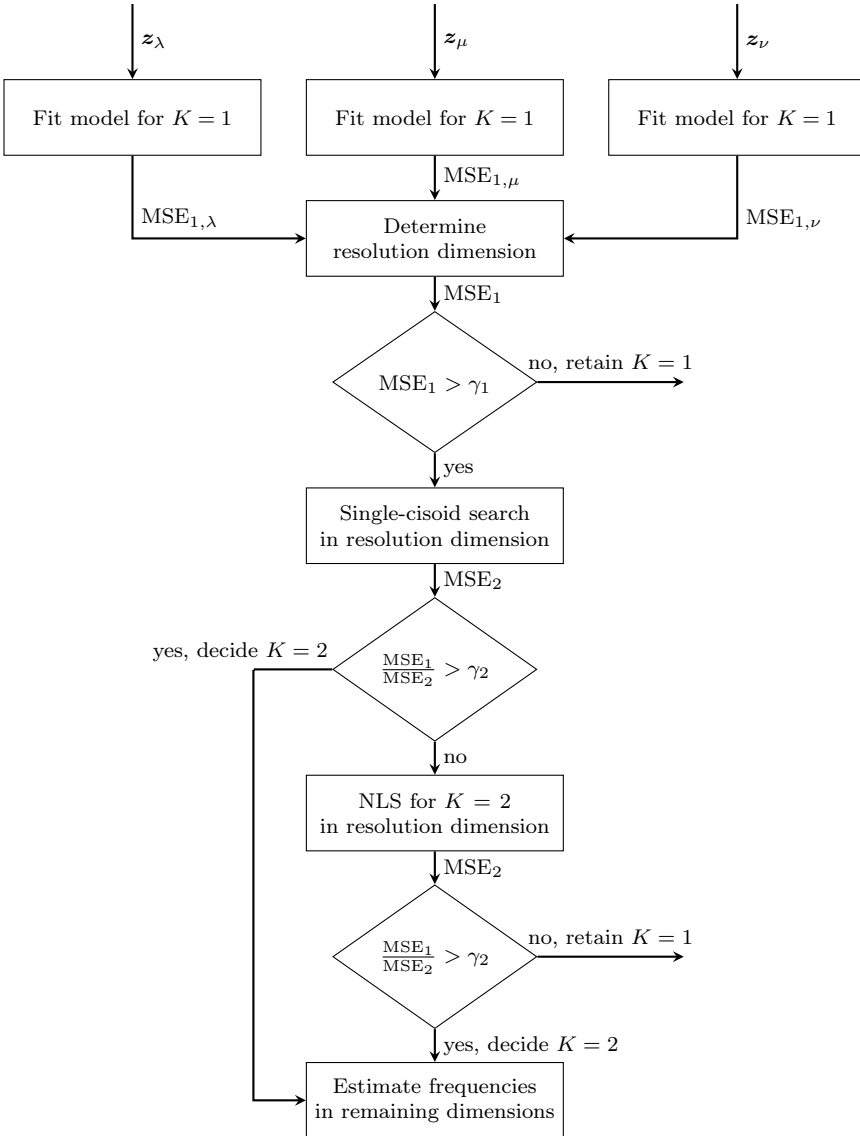
Figure 5.10: Processing sequence proposed in Chapter 3 extended with the single-cisoid search approach of Chapter 4.

(a)

(b)
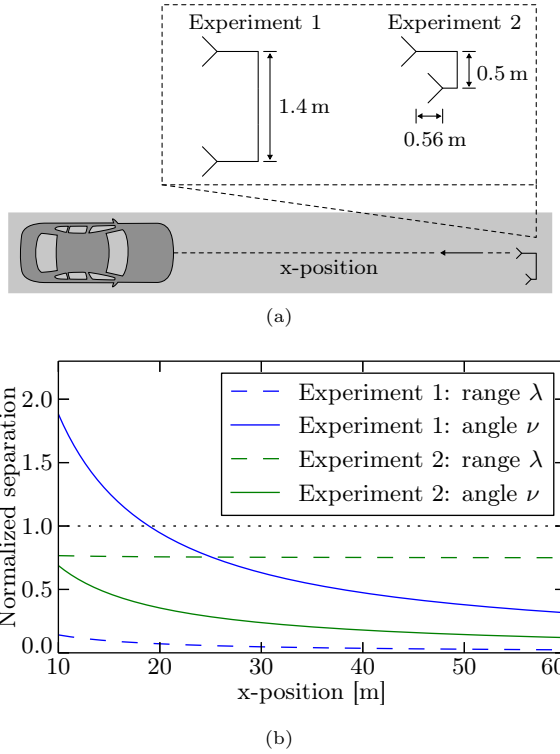
Figure 5.11: Experimental setup with two corner reflectors (a) and corresponding normalized frequency separation (b). For the mapping of range and angle to normalized frequencies, the radar system parameters in Table 5.2 are used.

provide resolved and accurate frequency estimates. In contrast, we expect that high-resolution processing in the spatial domain performs significantly worse due to the predefined resolution dimension and the much smaller angular separation.

Figure 5.12 shows the resulting position estimates in Cartesian coordinates for the first experiment, which are obtained with (a) conventional radar processing, (b) high-resolution frequency estimation in the spatial domain, and (c) high-resolution frequency estimation in the Fourier domain with optimal selection of resolution dimension. The true target positions are shown as dashed vertical lines. As expected, conventional processing fails to resolve the two targets except for x-positions below 18 m. In contrast, both high-resolution approaches are well able to resolve the targets and provide accurate position estimates. Note that this means, that the resolution
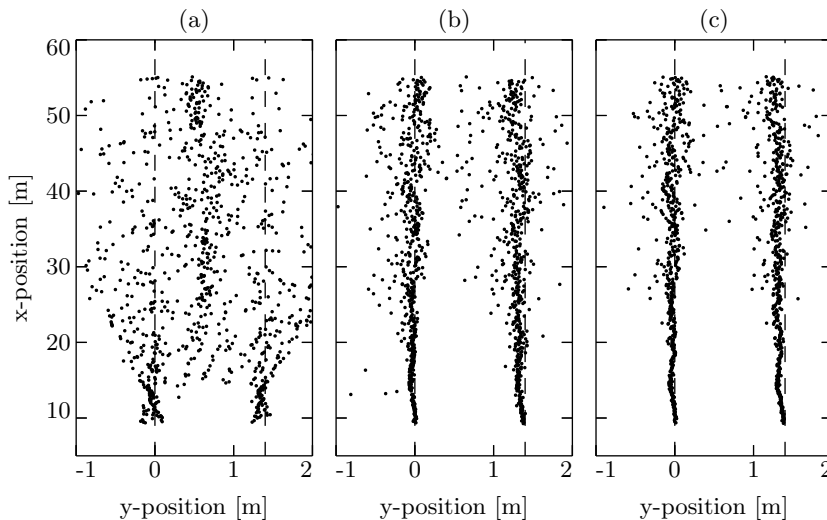
Figure 5.12: Real data results of a series production automotive radar sensor for experiment 1 as described in Figure 5.11. Position estimates in Cartesian coordinates obtained with (a) conventional radar processing (b) high-resolution frequency estimation in the spatial domain (c) high-resolution frequency estimation in the Fourier domain with optimal selection of resolution dimension.

dimension was correctly selected by the approach proposed in Section 3.2.1.

Figure 5.13 shows the corresponding results for the second experiment. Here, conventional processing fails for all x-positions. The high-resolution approach in the spatial domain breaks down for x-positions above 30 m due to the small frequency separation in the angular dimension. Only the high-resolution, Fourier-domain approach can resolve the two targets for all x-positions, as it exploits the much larger range separation. Note that this is enabled by the approach proposed in Section 3.2.1, which correctly selects the range dimension as resolution dimension.

5.4.4 Single-cisoid search comparison

We use additional experiments to demonstrate the effectiveness of combining the optimal NLS-based frequency estimation and the single-cisoid search based frequency estimation, as outlined in Figure 5.10. Note that the radar system parameters are the same as considered before and are gathered in Table 5.2.
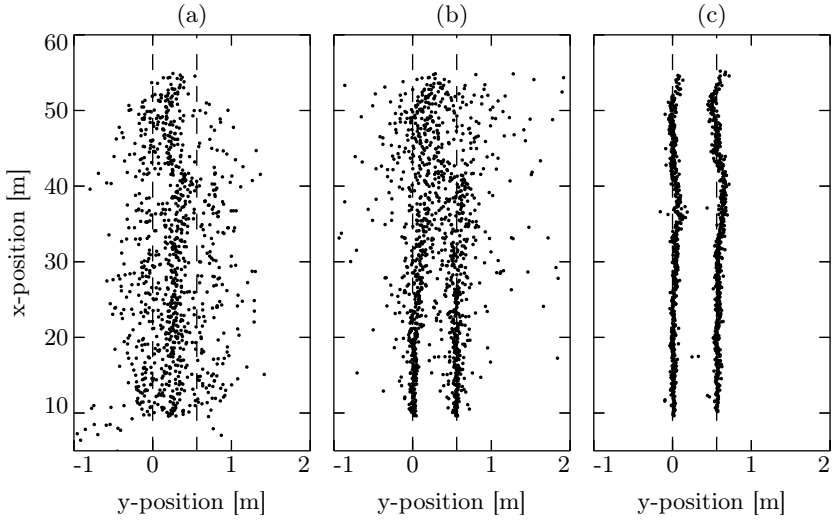
Figure 5.13: Real data results of a series production automotive radar sensor for experiment 2 as described in Figure 5.11. Position estimates in Cartesian coordinates obtained with (a) conventional radar processing (b) high-resolution frequency estimation in the spatial domain (c) high-resolution frequency estimation in the Fourier domain with optimal selection of resolution dimension.

The experimental setup is shown in Figure 5.14 (a) and is of the same type as in Figure 5.11 (a). That is, two corner reflectors are placed on a carrier, which allows for variable relative positioning, and are moved towards the radar sensor. Here, longitudinal corner separations of 0.56 m (experiment 2), 0.37 m (experiment 3), and 0.22 m (experiment 4) and a lateral separation of 0.5 m are used.

Figure 5.14 (b) shows the corresponding frequency separations normalized to the respective resolution limits. The radial velocity separation is very low and thus omitted. Observe that for all experiments the frequency separation in the range dimension is the largest for x-positions above 25 m. The separation in the angular dimension exceeds the frequency separation in the range dimension for x-positions below 15 m and 25 m for the third and the fourth experiment, respectively.

Figure 5.15 shows the resulting position estimates in Cartesian coordinates for the second, third, and fourth experiment, which are obtained with (a) single-cisoid search based frequency estimation, according to Figure 4.1 and (b) with NLS-based frequency estimation according to Figure 3.1. Observe that both methods are able to provide resolved position estimates for the second and third experiment, whereas for

(a)

(b)
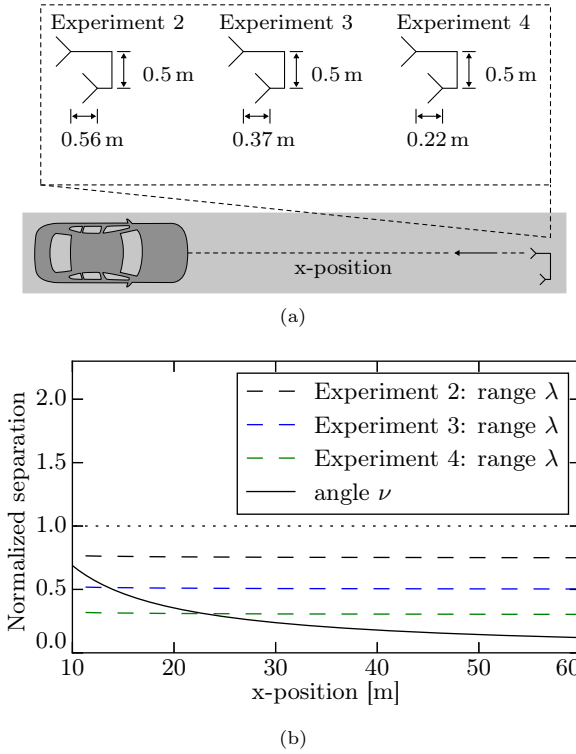
Figure 5.14: Experimental setup with two corner reflectors (a) and corresponding normalized frequency separation (b). For the mapping of range and angle to normalized frequencies, the radar system parameters in Table 5.2 are used.

the fourth experiment the resolution performance starts to break down due to the small frequency separation in the range dimension, which is below 50 % of the resolution limit. The obtained results show, that single-cisoid search based frequency estimation constitutes a computationally simpler alternative to NLS-based estimation and that the processing sequence in Figure 5.10 is a computationally efficient approach for automotive radars to obtain high-resolution capability in the range, radial velocity, and angular dimension.

(a)

(b)
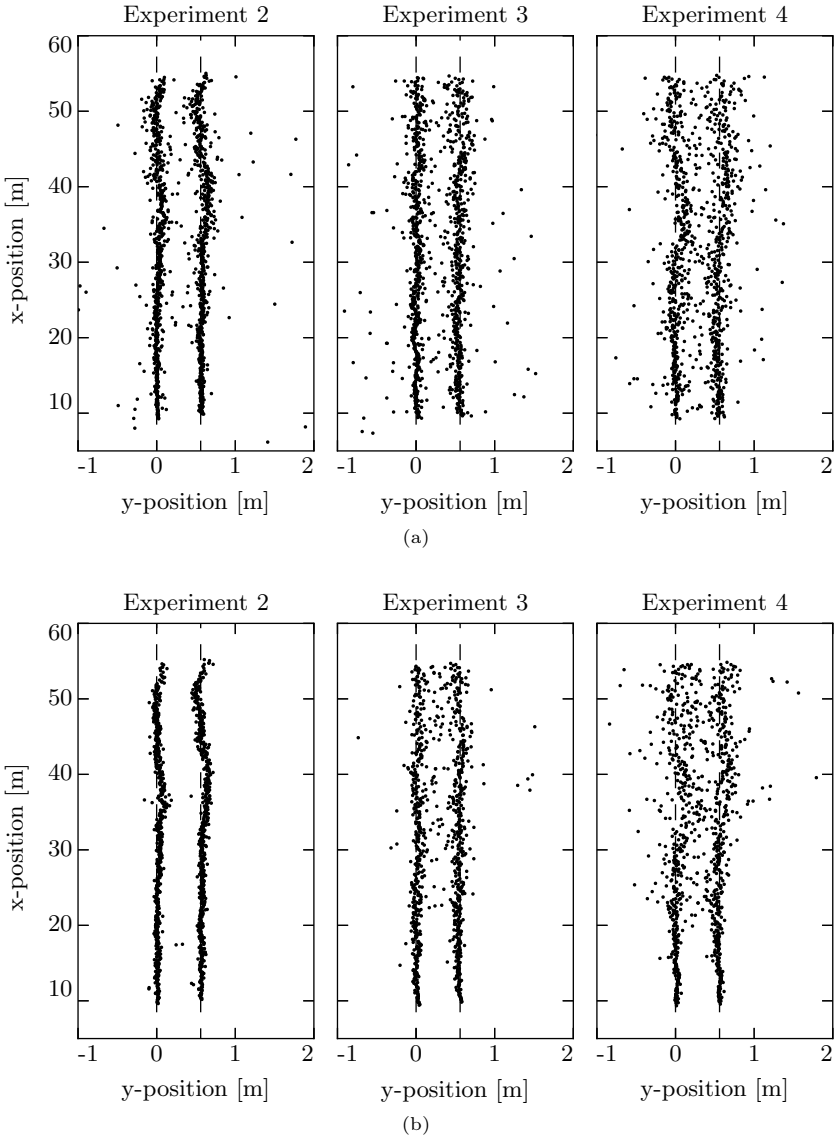
Figure 5.15: Real data results of a series production automotive radar sensor for experiment 2, experiment 3, and experiment 4 as described in Figure 5.14. Position estimates in Cartesian coordinates obtained with (a) single-cisoid search frequency estimation (b) NLS-based frequency estimation.

5.A Appendix

5.A.1 Target detection

We derive the detection threshold considered in Section 5.2.1 to distinguish periodogram values, which are due to noise only from periodogram values due to a target plus noise.

To this end, consider the likelihood ratio test [vT68b]

$$\frac{p(P(l,m,n)\,|\,\mathrm{H}_0)}{p(P(l,m,n)\,|\,\mathrm{H}_1)} \underset{\mathrm{H}_0}{\overset{\mathrm{H}_1}{\gtrless}} \tilde{\gamma}, \tag{5.21}$$

where H_0 denotes the noise only hypothesis, H_1 the target plus noise hypothesis, and $p(P(l,m,n)\,|\,\mathrm{H}_0)$ and $p(P(l,m,n)\,|\,\mathrm{H}_1)$ are the distributions of the periodogram $P(l,m,n)$ under both hypothesis. For each DFT index the likelihood ratio on the left hand side of (5.21) is compared to a threshold $\tilde{\gamma}$. For likelihood ratios above $\tilde{\gamma}$ the H_1-hypothesis is accepted and for values below the H_0-hypothesis.

To calculate the likelihood ratio, the probability distributions of the periodogram under both hypotheses are needed. In the noise only case it is exponentially distributed

$$p\left(P(l,m,n)\,|\,\mathrm{H}_0\right) = \frac{1}{\sigma^2} e^{\frac{-P(l,m,n)}{\sigma^2}}, \tag{5.22}$$

where σ^2 is the variance after Fourier transformation. The distribution of the periodogram under the H_1-hypothesis is given by a non-central chi-square distribution with two degrees of freedom [Pat49]

$$p\left(P(l,m,n)\,|\,\mathrm{H}_1\right) = \frac{1}{\sigma^2} e^{-\frac{P(l,m,n)+P_s(l,m,n)}{\sigma^2}} \, I_0\left(2\frac{\sqrt{P_s\left(l,m,n\right)}}{\sigma^2}\sqrt{P(l,m,n)}\right), \tag{5.23}$$

since the target parameters are unknown but deterministic. Herein,

$$P_s\left(l,m,n\right) = \left|\sum_{k=1}^{K} a_k W_\lambda\left(\Delta\lambda\, l - \lambda_k\right) W_\mu\left(\Delta\mu\, m - \mu_k\right) W_\nu\left(\Delta\nu\, n - \nu_k\right)\right|^2,$$

and $I_0\left(\cdot\right)$ denotes the modified Bessel function of the first kind.

The calculation of the likelihood ratio can be avoided and the periodogram can be compared directly with a modified threshold. This can be seen by substituting (5.22) and (5.23) in (5.21), taking the logarithm on both sides, and rearranging terms

$$\ln\left[I_0\left(2\frac{\sqrt{P_s\left(l,m,n\right)}}{\sigma^2}\sqrt{P(l,m,n)}\right)\right] \underset{\mathrm{H}_0}{\overset{\mathrm{H}_1}{\gtrless}} \ln\tilde{\gamma} + \frac{P_s\left(l,m,n\right)}{\sigma^2}.$$

The logarithm, the Bessel function, and the square root are all monotonically increasing functions. Thus the same test result can be obtained by comparing the periodogram directly with a modified threshold γ, which gives the test

$$P(l, m, n) \underset{H_0}{\overset{H_1}{\gtrless}} \gamma.$$

The threshold can be obtained as [vT68b]

$$\gamma = \ln(P_F)\,\sigma^2$$

where P_F is a desired probability of false alarm, that is the probability of erroneously deciding for H_1.

5.A.2 Microstrip antennas

Microstrip antennas consist of planar structures, e.g. patches or strips, etched out in metal films on dielectric substrates [Kil15]. They can be fabricated using printed circuit board technology, which enables cost-efficient mass production and space-efficient sensor design. This makes microstrip antennas attractive for automotive radar, where they constitute a cost and space-efficient alternative to reflector or lens antennas [MM12].

Multiple microstrip antennas can be combined, either via serial feeding or by a parallel power distribution network, to form an array antenna [Kil15, RA13]. The number of antenna elements, their positions, and their relative amplitudes serve as design parameters to obtain a desired gain and directivity. A practical example is the rectangular patch array, which consists of microstrip patches arranged on a rectangular grid. An example is shown in Figure 5.16, where the array consists of five columns, each comprised of seven patch elements. Columns are realized by serial feeding and combined via parallel power distribution. For the given patch arrangement, the directivity of the array antenna can be controlled via the row and column spacings and via tapering of the patch or connection line widths [CO09].

5.A.3 High-frequency electromagnetic scattering

Typical automotive radar targets, such as cars, trucks, motorcycles, road boundaries, or road signs are large with respect to typical wavelengths, 3.79 mm, 3.94 mm, and 12.5 mm, employed in automotive radar. Therefore so called high frequency, that is small wavelength, approximations to the general electromagnetic scattering problem apply. High frequency methods solve Maxwell's equations [MPM89] asymptotically in order to avoid a complex, rigorous solution. The so obtained results allow an intuitive insight to scattering problems for which the scatterers dimensions are so large,
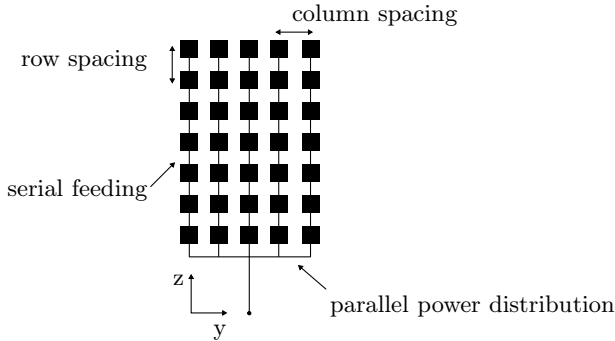
Figure 5.16: Rectangular microstrip patch antenna array with five columns, each comprised of seven patch antennas. Columns are realized by serial-fed patch antennas and are combined by a parallel power distribution network.

that scattering becomes a local phenomenon and interactions of different scatterer parts can be neglected. High frequency methods include: geometrical optics (GO), geometrical theory of diffraction (GTD), and physical optics (PO). GO as well as GTD are based on a ray optical approach, where the scattered field is comprised of multiple plane waves each propagating along straight lines called rays. In contrast, PO is based on a superposition of elementary surface currents leading to a surface integral description. Each of the above methods can be associated with canonical geometries, for which closed form high frequency approximations exist. Canonical geometries for GO are doubly curved surfaces, for GTD edges, wedges, and corners, and for PO the finite flat surface. Complex targets can be locally modelled by such canonical shapes and the high frequency scattering of the target is the superposition of the local canonical solutions. This is the idea behind so-called scattering center models [RB68, KST93, PM97, BML97, JHZQ08, GPGV99], which are considered in [SBW08, Büh08, Bud11, HSSS12] for modelling the scattering of automotive radar targets. Experimental verification of scattering center models can be found in [AFM+11, AFM12, SFGT+11].

Here, we consider an example and discuss the dominating scattering centers of a typical car, which is shown in Figure 5.17. The locations of dominant scattering centers are labeled with ① to ④. Note that those do not necessarily coincide with exact scattering center positions but only indicate target parts which can lead to a scattering center for certain directions of incidence. This is in particular true for flat surfaces such as the cars side ①, which give rise to PO type specular scattering and can be modelled by a scattering center at the point of reflection [Büh08]. As the reflection point depends on the direction of incidence, so does the scattering center position. In the same way we can determine the scattering center locations associated
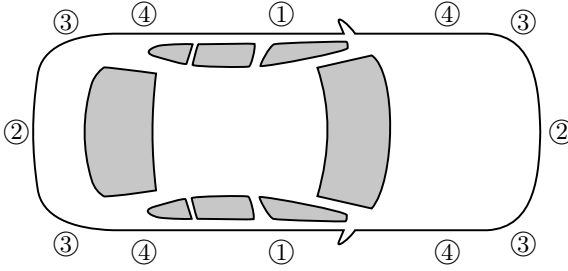
Figure 5.17: Outline of a typical car with scattering center locations.

with the cars front ②, the cars back ②, and its corners ③. The corresponding scattering types are flat surface PO scattering ② and doubly curved surface GO type scattering ③ [Büh08]. The main scattering contribution of ② stems from the cars license plates [AFM+11] acting as the flat surface for reflection. The wheelhouses give rise to so called multiple bounce scattering [LCL89]. The incident ray is reflected multiple times inside the wheelhouse before eventually leaving it. This leads to a scattering center ④ for a large range of incident angles [Büh08].

In addition to the scattering centers shown in Figure 5.17, the radar can observe scattering centers at the bottom side of the car, via specular multipath involving the road surface. The reflectivity of road surfaces is studied comprehensively in [Sch98], where it is found that the most common surfaces act as a mirror at automotive radar wavelengths. The cars bottom side has an inhomogeneous structure compared to the body [Sch98] and a main scattering center is difficult to locate by considering a geometry common to a large variety of cars. However, we found from measurements that scattering centers are often located at the cars axles.

5.A.4 High-resolution processing in the spatial domain

High-resolution processing in the spatial domain has been considered in [Hei12] for state-of-the-art automotive radars and are discussed in [EHZ+17] as a special case of the framework developed in this thesis. Here we give a brief overview.

A calculation similar to (5.15), but without the angular DTFT is

$$Y(\lambda, \mu; n_s) = \sum_{l_s=0}^{L_s-1} \sum_{m_s=0}^{M_s-1} w_\lambda(l_s) w_\mu(m_s) x(l_s, m_s, n_s) e^{-j(\lambda l_s + \mu m_s)} \qquad (5.24)$$

with $\lambda \in [0, 2\pi)$, $\mu \in [0, 2\pi)$, and $n_s = 0, \ldots, N_s - 1$. The data model after 2-D finite DTFT calculation in (5.24) can be obtained similarly to (5.15). The corresponding local vector model is

$$\mathbf{y}(\lambda, \mu) = \sum_{k=1}^{K} \alpha_k(\lambda, \mu) \mathbf{v}(\nu_k) + \text{noise}, \tag{5.25}$$

where $\alpha_k(\lambda, \mu)$ is given in (3.11), and $\mathbf{v}(\nu_k) = \left[1, e^{j\nu_k}, \ldots, e^{j(N_s-1)\nu_k}\right]^T$ is a ULA steering vector. Note that the model in (5.25) is in the original domain, in which the vector elements correspond to spatial array elements, whereas the model in (3.8) is in the Fourier domain, in which the vector elements correspond to samples of the angular spectrum.

Figure 5.18 gives an overview of high-resolution processing in the spatial domain. Here, the single-target model is fitted in the spatial domain and the resulting MSE is used for two-target indication. If a two-target situation is likely the corresponding model is fitted and the resulting MSE is used in simplified GLRT to decide between the two models. For the two-target model, resolved angular frequencies can be used to obtain the corresponding frequencies in the range and radial velocity dimension similarly to the approach in Section 3.4.2.
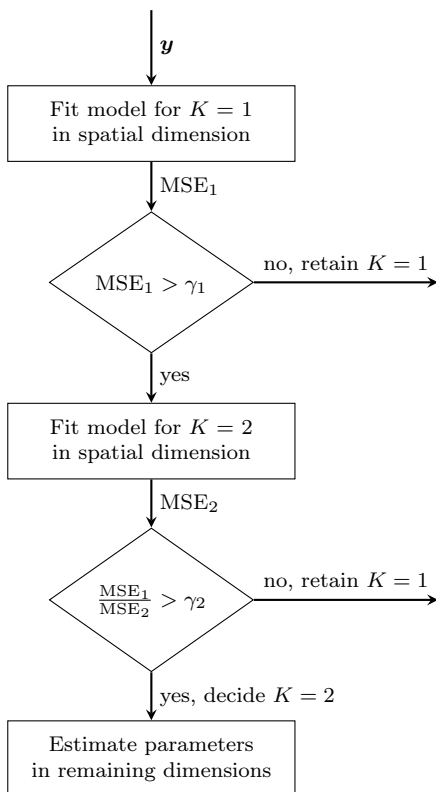
Figure 5.18: Overview of high-resolution processing in the spatial domain.

6 Conclusions and outlook

In this thesis, novel approaches to computationally efficient multidimensional frequency estimation with high-resolution capability have been developed. In Section 6.1 we draw conclusions and in Section 6.2 we give an outlook on possible future work.

6.1 Conclusions

We have developed a framework on multidimensional high-resolution frequency estimation, which employs Fourier transform pre-processing to select frequency sub-bands, which are either represented by a local single-cisoid model or a local two-cisoid model. The sub-bands are obtained by frequency neighborhoods of periodogram peaks. For each local model a different approach to frequency estimation has been employed: high-resolution frequency estimation for the two-cisoid model and periodogram-based estimation for the single-cisoid model. For the latter, we proposed a computationally simple LUT-based method to compensate estimation errors due to a frequency discretization.

For the two-cisoid model, a high-resolution frequency estimation, which estimates frequencies in all dimensions jointly is considered to costly. To reduce the computational complexity, the multidimensional frequency estimation has been decoupled in a sequence of computationally simpler 1-D problems. For a decoupled frequency estimation, one has to decide on the processing sequence. In one dimension, referred to as resolution dimension, a high-resolution frequency estimation for two cisoids is performed first. In a second step, the resulting frequency estimates in the resolution dimension are used to obtain two single-cisoid frequency estimation problems in the remaining dimensions. These are computationally much simpler than the frequency estimation for two cisoids and can be solved by a periodogram-based approach. For the success of the decoupled approach, frequency separation in the resolution dimension is crucial. To ensure this, we proposed to select the best resolution dimension adaptively. To this end, we selected the dimension with the largest corresponding MSE of the single-cisoid model fit. For the 1-D frequency estimation for two cisoids we proposed a NLS-based method, which comprises two steps. First, the NLS criterion function is evaluated on a coarse frequency grid. Subsequently, the resulting estimates are refined by Gauss-Newton iterations in a second step. For the frequency

estimation in the remaining dimensions, we considered a LUT-based approach to correct estimation errors due to frequency discretization. Simulation results show that the proposed framework can provide resolved frequencies for the case of two cisoids with frequency separations below the resolution limits. The accuracy of the obtained frequency estimates are close to the CRB. Further simulations demonstrate the effectiveness of selecting the resolution dimension according to the largest MSE of the single-cisoid model fit.

The computational complexity of the proposed decoupled framework is determined by NLS-based frequency estimation for two cisoids. To simplify that step we have proposed a novel frequency estimation, which we have called single-cisoid search. It is based on finding frequencies in the remaining dimensions, for which the resolution dimension is well represented by a single-cisoid model. The frequencies in the resolution dimension are then obtained by a simple periodogram maximization and the remaining dimension frequencies by the previously considered decoupled approach. To improve the accuracy of the so obtained frequency estimates we proposed a bias correction step. Compared to optimal NLS-based frequency estimation, the single-cisoid search frequency estimator is computationally much simpler. However, it relies on frequency separation in at least two dimensions. Simulation results show a good resolution performance for the two cisoid case with frequency separations below the resolution limits. Interestingly, out-of-band interference showed only a minor influence on accuracy and resolution performance.

We have considered the proposed framework on multidimensional frequency estimation to enhance the resolution capability of state-of-the-art automotive radar sensors. Here, the frequency dimensions are associated with range, radial velocity, and angle of targets and thus localization and motion estimation are achieved through frequency estimation. The proposed framework has been incorporated in conventional radar processing, which is based on Fourier transformation of the sampled baseband signal. The processing steps of the proposed framework are applied for each detected peak. Due to the fact that targets are for most scenarios well separated, the peak neighborhoods are typically represented by a single-target model. As a consequence, the proposed framework employs mostly computationally efficient periodogram-based frequency estimation. In critical use-cases a small subset of peaks are due to unresolved target pairs. We have pointed out that in such use-cases it is advantageous to use either the range, the radial velocity, or the angular dimension as the resolution dimension in a decoupled approach. The effectiveness of the proposed framework has been demonstrated using experimental results obtained with a series-production automotive radar sensor. The results show a strong resolution enhancement compared to conventional processing and demonstrate the practical relevance of resolution dimension selection for decoupled frequency estimation.

6.2 Outlook

Possible future work includes the extension of the proposed framework to cases, where local frequency sub-bands can contain more than two cisoids with frequency separations below the resolution limits. The presented decoupled framework is still appropriate when the initial 1-D high-resolution frequency estimation is performed for more than two cisoids. For this task, optimal NLS-based frequency estimation might be to costly and methods with lower complexity should be investigated.

For strong out-of-band interference, it might be advantageous to use the single-cisoid search approach also for sub-bands with only one cisoid. In this way, remaining dimension frequencies might be found for which the resolution dimension is less influenced by the interference than it is for the peak frequencies. This should be validated with simulations and experimental data.

For automotive radars, the influence of imperfections in the signal generation, e.g. non linearities in the frequency chirps or a slow drift of the carrier frequency, on a decoupled frequency estimation have to be investigated. In particular the influence on high-resolution frequency estimation in the range or radial velocity dimension should be considered. Further, scattering center extraction based on the proposed framework should be validated with experimental data.

List of acronyms

ACC	Adaptive cruise control
ADAS	Advance driver assistance systems
CFAR	Constant false alarm rate
CPI	Coherent processing interval
CRB	Cramér Rao bound
DFT	Discrete Fourier transform
DTFT	Discrete time Fourier transform
EEG	Electroencephalogram
EM	Electromagnetic
BS-ESPRIT	Beamspace estimation of signal parameters via rotational invariance techniques
FCA	Forward collision avoidance
FFT	Fast Fourier transform
FMCW	Frequency modulated continuous wave
GO	Geometrical optics
GP	General purpose
GTD	Geometrical theory of diffraction
HAD	Highly automated driving
LCA	Lane change assist
LFM	Linear frequency modulation
LUT	Look-up table
BS-MUSIC	Beamspcae multiple signal classification
MC	Monte Carlo
ML	Maximum likelihood

List of acronyms

MLW	Mainlobe width
NLS	Non linear least squares
NMR	Nuclear magnetic resonance
1-D	One-dimensional
PO	Physical optics
RMSE	Root mean square error
Rx	Receive
SIR	Signal-to-interference ratio
SLL	Sidelobe level
SNR	Signal-to-noise ratio
Tx	Transmit
3-D	Three-dimensional
ULA	Uniform linear array

Bibliography

[AFM+11]   M. Andres, P. Feil, W. Menzel, H.-L. Bloecher, and J. Dickmann, "Analysis of automobile scattering center locations by SAR measurements," in *Radar Conference (RADAR), 2011 IEEE*, May 2011, pp. 109–112.

[AFM12]   M. Andres, P. Feil, and W. Menzel, "3D-scattering center detection of automotive targets using 77 GHz UWB radar sensors," in *Antennas and Propagation (EUCAP), 2012 6th European Conference on*, March 2012, pp. 3690–3693.

[AS64]   M. Abramowitz and I. A. Stegun, *Handbook of Mathematical Functions with Formulas, Graphs, and Mathematical Tables*, 5th ed. Dover Publications, 1964.

[Ath01]   F. Athley, "Angle and frequency estimation using sensor arrays," Ph.D. dissertation, Chalmers University of Technology, 2001.

[Büh08]   M. Bühren, "Simulation und Verarbeitung von Radarziellisten im Automobil," Ph.D. dissertation, Universität Stuttgart, Jan 2008.

[BDF+14]   K. Bengler, K. Dietmayer, B. Farber, M. Maurer, C. Stiller, and H. Winner, "Three decades of driver assistance systems: Review and future perspectives," *IEEE Intelligent Transportation Systems Magazine*, vol. 6, no. 4, pp. 6–22, winter 2014.

[BML97]   R. Bhalla, J. Moore, and H. Ling, "A global scattering center representation of complex targets using the shooting and bouncing ray technique," *IEEE Trans. Antennas and Propagation* , vol. 45, no. 12, pp. 1850–1856, Dec 1997.

[BMS12]   A. Bartels, M. Meinecke, and S. Steinmeyer, "Lane change assist," in *Handbook of Intelligent Vehicles*, 1st ed., A. Eskandarian, Ed. Springer New York, 2012, pp. 729–757.

[Bri81]   D. R. Brillinger, *Time Series: Data Analysis and Theory*, 2nd ed. Holden Day Inc., 1981.

[Bud11]   H. Buddendick, "Streuzentrenmodelle zur Simulation der Wellenausbreitung für automobile Radar- und Funksysteme," Ph.D. dissertation, Technische Universität München, 2011.

[Can13]   C. Candan, "Analysis and further improvement of fine resolution frequency estimation method from three DFT samples," *IEEE Signal Processing Letters*, vol. 20, no. 9, pp. 913–916, Sept 2013.

[Cap71]   W. J. Caputi, "Stretch: A time-transformation technique," *IEEE Trans. Aerospace and Electronic Systems*, vol. AES-7, no. 2, pp. 269–278, March 1971.

[CO09]   Z. Chen and S. Otto, "A taper optimization for pattern synthesis of microstrip series-fed patch array antennas," in *2009 European Wireless Technology Conference*, Sept 2009, pp. 160–163.

[CS94]   M. P. Clark and L. L. Scharf, "Two-dimensional modal analysis based on maximum likelihood," *IEEE Trans. Signal Processing*, vol. 42, no. 6, pp. 1443–1452, Jun 1994.

[CT65]   J. W. Cooley and J. W. Tukey, "An algorithm for the machine calculation of complex fourier series," *Mathematics of computation*, vol. 19, no. 90, pp. 297–301, 1965.

[DAB⁺14]   J. Dickmann, N. Appenrodt, H.-L. Bloecher, C. Brenk, T. Hackbarth, M. Hahn, J. Klappstein, M. Muntzinger, and A. Sailer, "Radar contribution to highly automated driving," in *European Radar Conference (EuRAD)*, Oct 2014, pp. 412–415.

[DAK⁺15]   J. Dickmann, N. Appenrodt, J. Klappstein, H.-L. Bloecher, M. Muntzinger, A. Sailer, M. Hahn, and C. Brenk, "Making bertha see even more: Radar contribution," *IEEE Access*, vol. 3, pp. 1233–1247, 2015.

[DDF⁺12]   T. Dang, J. Desens, U. Franke, D. Gavrila, L. Schäfers, and W. Ziegler, "Steering and evasion assist," in *Handbook of Intelligent Vehicles*, 1st ed., A. Eskandarian, Ed.   Springer New York, 2012, pp. 759–782.

[DH07]   A. Drosopoulos and S. Haykin, "Angle-of-arrival estimation in the presence of multipath," in *Adaptive Radar Signal Processing*, 1st ed., S. Haykin, Ed.   John Wiley & Sons, 2007, pp. 11–91.

[DKH⁺15]   J. Dickmann, J. Klappstein, M. Hahn, M. Muntzinger, N. Appenrodt, C. Brenk, and A. Sailer, "Present research activities and future requirements on automotive radar from a car manufacturers point of view"," in *IEEE MTT-S International Conference on Microwaves for Intelligent Mobility (ICMIM)*, April 2015, pp. 1–4.

[Dol46]   C. Dolph, "A current distribution for broadside arrays which optimizes the relationship between beam width and side-lobe level," *Proceedings of the IRE*, vol. 34, no. 6, pp. 335–348, June 1946.

[EHZ$^+$17]   F. Engels, P. Heidenreich, A. Zoubir, F. Jondral, and M. Winterman-tel, "Advances in automotive radar: A framework on computationally efficient high-resolution frequency estimation," *IEEE Signal Processing Magazine*, Mar 2017.

[Eng14]   F. Engels, "Target shape estimation using an automotive radar," in *Smart Mobile In-Vehicle Systems – Next Generation Advancements*, 1st ed.   Springer New York, 2014.

[FR06]   F. Fölster and H. Rohling, "Lateral velocity estimation based on automotive radar sensors," in *Radar Conference*, Oct 2006, pp. 1–4.

[Fri08]   B. Friedlander, "Adaptive signal design for MIMO radars," in *MIMO Radar Signal Processing*, 1st ed., J. Li and P. Stoica, Eds.   John Wiley & Sons, Inc., 2008, pp. 193–234.

[GHFS14]   A. Garcia-Fernandez, L. Hammarstrand, M. Fatemi, and L. Svensson, "Bayesian road estimation using onboard sensors," *IEEE Trans. Intelligent Transportation Systems*, vol. 15, no. 4, pp. 1676–1689, Aug 2014.

[GMP12]   F. Gini, A. D. Maio, and L. K. Patton, *Waveform Design and Diversity for Advanced Radar Systems*.   The Institution of Engineering and Technology, 2012.

[GPGV99]   M. Gerry, L. Potter, I. Gupta, and A. Van Der Merwe, "A parametric model for synthetic aperture radar measurements," *IEEE Trans. Antennas and Propagation*, vol. 47, no. 7, pp. 1179–1188, Jul 1999.

[Gra83]   T. Grandke, "Interpolation algorithms for discrete fourier transforms of weighted signals," *IEEE Trans. Instrumentation and Measurement*, vol. 32, no. 2, pp. 350–355, June 1983.

[GSDB07]   J. Gunnarsson, L. Svensson, L. Danielsson, and F. Bengtsson, "Tracking vehicles using radar detections," in *IEEE Intelligent Vehicles Symposium*, June 2007, pp. 296–302.

[GvL96]   G. Golub and C. van Loan, *Matrix Computations*, 3rd ed.   The Johns Hopkins University Press, 1996.

[Har78]   F. Harris, "On the use of windows for harmonic analysis with the discrete Fourier transform," *Proceedings of the IEEE*, vol. 66, no. 1, pp. 51–83, Jan 1978.

[HBN98]   M. Haardt, C. Brunner, and J. Nossek, "Efficient high-resolution 3-D channel sounding," in *48th IEEE Vehicular Technology Conference*, vol. 1, May 1998, pp. 164–168 vol.1.

[Hei12]   P. Heidenreich, "Antenna Array Processing: Autocalibration and Fast High-Resolution Methods for Automotive Radar," Ph.D. dissertation, Technische Universität Darmstadt, Feb 2012.

[Heu13]   S. Heuel, "Fußgängererkennung im Straßenverkehr mi 24GHz Radarsensoren," Ph.D. dissertation, Technische Universität Hamburg-Harburg, Dez 2013.

[HLS12]   L. Hammarstrand, M. Lundgren, and L. Svensson, "Adaptive radar sensor model for tracking structured extended objects," *IEEE Trans. Aerospace and Electronic Systems*, vol. 48, no. 3, pp. 1975–1995, Jul 2012.

[HN98]   M. Haardt and J. A. Nossek, "Simultaneous schur decomposition of several nonsymmetric matrices to achieve automatic pairing in multidimensional harmonic retrieval problems," *IEEE Trans. Signal Processing*, vol. 46, no. 1, pp. 161–169, Jan 1998.

[HSSS12]   L. Hammarstrand, L. Svensson, F. Sandblom, and J. Sorstedt, "Extended object tracking using a radar resolution model," *IEEE Trans. Aerospace and Electronic Systems*, vol. 48, no. 3, pp. 2371–2386, Jul 2012.

[JHZQ08]   Z. Jianxiong, Z. Hongzhong, S. Zhiguang, and F. Qiang, "Global scattering center model extraction of radar targets based on wideband measurements," *IEEE Trans. Antennas and Propagation*, vol. 56, no. 7, pp. 2051–2060, Jul 2008.

[JK07]   E. Jacobsen and P. Kootsookos, "Fast, accurate frequency estimators," *IEEE Signal Processing Magazine*, vol. 24, no. 3, pp. 123–125, May 2007.

[JR81]   E. Jacobs and E. W. Ralston, "Ambiguity resolution in interferometry," *IEEE Trans. Aerospace and Electronic Systems*, vol. AES-17, no. 6, pp. 766–780, Nov 1981.

[KB13]   B. Keel and J. Baden, "Advanced pulse compression waveform modulations and techniques," in *Principles of Modern Radar Advanced Techniques*, 1st ed., W. Melvin and J. Scheer, Eds.   SciTech Publishing, Incorporated, 2013, pp. 19–85.

[KHC07]   S. Kia, H. Henao, and G.-A. Capolino, "A high-resolution frequency estimation method for three-phase induction machine fault detection," *IEEE Trans. Industrial Electronics*, vol. 54, no. 4, pp. 2305–2314, Aug 2007.

[Kil15]   P.-S. Kildal, *Foundations of Antenna Engineering - A Unified Approach for Line-Of-Sight and Multipath*, 1st ed.   Kildal AB, 2015.

[Kle06]   R. Klemm, *Principles of Space-Time Adaptive Processing*, 3rd ed. The Institution of Engineering and Technology, 2006.

[Knu97]   D. E. Knuth, *The Art of Computer Programming, Vol. 1: Fundamental Algorithms*, 3rd ed.   Addison-Wesley Professional, 1997.

[Kro14]   M. Kronauge, "Waveform Design for Continuous Wave Radars," Ph.D. dissertation, Technische Universität Hamburg-Harburg, Jul 2014.

[KST93]   E. Knott, J. Shaeffer, and M. Tuley, *Radar Cross Section*, 2nd ed. Artech House, 1993.

[KV96]   H. Krim and M. Viberg, "Two decades of array signal processing research: the parametric approach," *IEE Signal Processing Magazine*, vol. 13, no. 4, pp. 67–94, Jul 1996.

[LCL89]   H. Ling, R.-C. Chou, and S.-W. Lee, "Shooting and bouncing rays: calculating the rcs of an arbitrarily shaped cavity," *IEEE Trans. Antennas and Propagation*, vol. 37, no. 2, pp. 194–205, Feb 1989.

[LE04]   N. Levanon and M. E., *Radar Signals*, 1st ed.   John Wiley & Sons, 2004.

[LHG11]   C. Lundquist, L. Hammarstrand, and F. Gustafsson, "Road intensity based mapping using radar measurements with a probability hypothesis density filter," *IEEE Trans. Signal Processing*, vol. 59, no. 4, pp. 1397–1408, Apr 2011.

[LHSV95]   J. Li, B. Halder, P. Stoica, and M. Viberg, "Computationally efficient angle estimation for signals with known waveforms," *IEEE Trans. Signal Processing*, vol. 43, no. 9, pp. 2154–2163, Sep 1995.

[LHT+13]   K. Li, B. Habtemariam, R. Tharmarasa, M. Pelletier, and T. Kirubarjan, "Multitarget tracking with doppler ambiguity," *IEEE Trans. Aerospace and Electronic Systems*, vol. 49, no. 4, pp. 2640–2656, Oct 2013.

[LRL98]   Y. Li, J. Razavilar, and K. Liu, "A high-resolution technique for multidimensional NMR spectroscopy," *IEEE Trans. Biomedical Engineering*, vol. 45, no. 1, pp. 78–86, Jan 1998.

[LSG12]   C. Lundquist, T. Schön, and F. Gustafsson, "Situational awareness and road prediction for trajectory control applications," in *Handbook of Intelligent Vehicles*, 1st ed., A. Eskandarian, Ed.   Springer New York, 2012, pp. 366–396.

[Mac98]   M. Macleod, "Fast nearly ml estimation of the parameters of real or complex single tones or resolved multiple tones," *IEEE Trans. Signal Processing*, vol. 46, no. 1, pp. 141–148, Jan 1998.

[Mau12]   M. Maurer, "Forward collision warning and avoidance," in *Handbook of Intelligent Vehicles*, 1st ed., A. Eskandarian, Ed.   Springer New York, 2012, pp. 657–687.

[MBF+13]   M. Murad, I. Bilik, M. Friesen, J. Nickolaou, J. Salinger, K. Geary, and J. S. Colburn, "Requirements for next generation automotive radars," in *IEEE Radar Conference (RadarCon13)*, April 2013, pp. 1–6.

[MLJ09]   J. Ma, G. Li, and B. H. Juang, "Signal processing in cognitive radio," *Proceedings of the IEEE*, vol. 97, no. 5, pp. 805–823, May 2009.

[MM12]   W. Menzel and A. Moebius, "Antenna concepts for millimeter-wave automotive radar sensors," *Proceedings of the IEEE*, vol. 100, no. 7, pp. 2372–2379, July 2012.

[MPM89]   D. McNamara, C. Pistorius, and J. Malherbe, *Introduction to the Uniform Geometrical Theory of Diffraction*, 1st ed.   Artech House, 1989.

[MSKB15]   F. Meinl, E. Schubert, M. Kunert, and H. Blume, "Realtime FPGA-based processing unit for a high-resolution automotive MIMO radar platform," in *European Radar Conference (EuRAD), 2015 12th*, Sep 2015, pp. 213–216.

[MV01]   T. McKelvey and M. Viberg, "A robust frequency domain subspace algorithm for multi-component harmonic retrieval," in *Conference Record of the Thirty-Fifth Asilomar Conference on Signals, Systems and Computers*, vol. 2, Nov 2001, pp. 1288–1292 vol.2.

[NRY15]   D. Nugraha, A. Roger, and R. Ygnace, "Intgerated FFT accelerator and inline bin-rejection for automotive FMCW radar signal processing," in *12th European Radar Conference (EuRAD)*, Sep 2015, pp. 213–216.

[NS10]   D. Nion and N. D. Sidiropoulos, "Tensor algebra and multidimensional harmonic retrieval in signal processing for mimo radar," *IEEE Trans. Signal Processing*, vol. 58, no. 11, pp. 5693–5705, Nov 2010.

[OSB98]   A. Oppenheim, R. Schafer, and J. Buck, *Discrete-time signal processing*, 2nd ed.   Prentice Hall, 1998.

[Pat49]   P. B. Patnaik, "The non-central χ^2- and F-distribution and their applications," *Biometrika*, vol. 36, no. 1, pp. 202–232, 1949.

[Pes05]   M. Pesavento, "Fast algorithms for multidimensional harmonic retrieval," Ph.D. dissertation, Ruhr Universität Bochum, 2005.

[PM97]   L. Potter and R. Moses, "Attributed scattering centers for SAR ATR," *IEEE Trans. Image Processing*, vol. 6, no. 1, pp. 79–91, Jan 1997.

[PPG12]   P. Parvazi, M. Pesavento, and A. B. Gershman, "Rooting-based harmonic retrieval using multiple shift-invariances: The complete and the incomplete sample cases," *IEEE Trans. Signal Processing*, vol. 60, no. 4, pp. 1556–1570, Apr 2012.

[PSH08]   J.-B. Poullet, D. M. Sima, and S. V. Huffel, "MRS signal quantitation: A review of time- and frequency-domain methods," *Journal of Magnetic Resonance*, vol. 195, no. 2, pp. 134 – 144, 2008.

[Qui94]   B. Quinn, "Estimating frequency by interpolation using fourier coefficients," *IEEE Trans. Signal Processing*, vol. 42, no. 5, pp. 1264–1268, May 1994.

[Qui97]   ——, "Estimation of frequency, amplitude, and phase from the dft of a time series," *IEEE Trans. Signal Processing*, vol. 45, no. 3, pp. 814–817, Mar 1997.

[RA13]   V. Rabinovich and N. Alexandrov, *Antenna Arrays and Automotive Applications*, 1st ed.   Springer, 2013.

[RB68]   R. Ross and M. E. Bechtel, "Scattering-center theory and radar glint analysis," *IEEE Trans. Aerospace and Electronic Systems*, vol. AES-4, no. 5, pp. 756–762, Sept 1968.

[RHST00]   A. Richter, D. Hampicke, G. Sommerkorn, and R. Thoma, "Joint estimation of dod, time-delay, and doa for high-resolution channel sounding," in *IEEE 51st Vehicular Technology Conference Proceedings*, vol. 2, 2000, pp. 1045–1049 vol.2.

[Ric14]   M. A. Richards, *Fundamentals of Radar Signal Processing*, 2nd ed.   McGraw-Hill Education, 2014.

[Rih69]   A. Rihazcek, *Principles of High-Resolution Radar*, 1st ed.   Artech House, 1969.

[Roh83]   H. Rohling, "Radar CFAR Thresholding in Clutter and Multiple Target Situations," *IEEE Trans. Aerospace and Electronic Systems*, vol. AES-19, no. 4, pp. 608–621, July 1983.

[RBVW06]   A. Rodriguez-Rivera, B. Baryshnikov, B. Van Veen, and R. Wakai, "MEG and EEG source localization in beamspace," *IEEE Trans. Biomedical Engineering*, vol. 53, no. 3, pp. 430–441, Mar 2006.

[RRH14]   M. Ravan, J. Reilly, and G. Hasey, "Minimum variance brain source localization for short data sequences," *IEEE Trans. Biomedical Engineering*, vol. 61, no. 2, pp. 535–546, Feb 2014.

[RSH10]   M. Richards, J. Scheer, and W. Holm, *Principles of Modern Radar Basic Principles.* SciTech Publishing, Incorporated, 2010.

[RSR69]   L. Rabiner, R. Schafer, and C. Rader, "The chirp z-transform algorithm," *IEEE Trans. Audio and Electroacoustics*, vol. 17, no. 2, pp. 86–92, Jun 1969.

[RV70]   D. Rife and G. Vincent, "Use of the discrete fourier transform in the measurement of frequencies and levels of tones," *The Bell System Technical Journal*, vol. 49, no. 2, pp. 197–228, Feb 1970.

[SA91]   P. Stoica and N. A., "Comparative performance study of element-space and beam-space music estimator," *Circuits, Systems and Signal Processing*, vol. 10, no. 3, pp. 285–292, Sep 1991.

[SBW08]   K. Schuler, D. Becker, and W. Wiesbeck, "Extraction of virtual scattering centers of vehicles by ray-tracing simulations," *IEEE Trans. Antennas and Propagation*, vol. 56, no. 11, pp. 3543–3551, Nov 2008.

[Sch98]   A. Schuster, "On the investigation of hidden periodicities with application to a supposed 26 day period of meteorological phenomena," *Terrestrial Magnetism*, vol. 3, no. 1, pp. 13–41, 1898.

[Sch98]   R. Schneider, "Modellierung der Wellenausbreitung für ein bildgebendes Kfz-Radar," Ph.D. dissertation, Universität Karlsruhe, Jun 1998.

[Sch10]   M. Schoor, "Hochauflösende Winkelschätzung für automobile Radarsysteme," Ph.D. dissertation, Universität Stuttgart, Feb 2010.

[SFGT⁺11] T. Schipper, J. Fortuny-Guasch, D. Tarchi, L. Reichardt, and T. Zwick, "RCS measurement results for automotive related objects at 23-27 GHz," in *Proceedings of the 5th European Conference on Antennas and Propagation (EUCAP)* , April 2011, pp. 683–686.

[SJL97]   P. Stoica, A. Jakobsson, and J. Li, "Cisoid parameter estimation in the colored noise case: asymptotic Cramer-Rao bound, maximum likelihood, and nonlinear least-squares," *IEEE Trans. Signal Processing*, vol. 45, no. 8, pp. 2048–2059, Aug 1997.

[SL01]   P. Stoica and E. Larsson, "Comments on "linearization method for finding cramér-rao bounds in signal processing"," *IEEE Trans. Signal Processing*, vol. 49, no. 12, pp. 3168–3169, Dec 2001.

[SM05]   P. Stoica and R. Moses, *Spectral Analysis of Signals*, 1st ed. Prentice Hall, 2005.

[SS98] A. Swindlehurst and P. Stoica, "Maximum likelihood methods in radar array signal processing," *Proceedings of the IEEE*, vol. 86, no. 2, pp. 421–441, Feb 1998.

[SSSL04] N. Sandgren, Y. Selen, P. Stoica, and J. Li, "Parametric methods for frequency-selective mr spectroscopy - a review," *Journal of Magnetic Resonance*, vol. 168, no. 2, pp. 259 – 272, 2004.

[SW14] T. Styles and L. Wildman, "An optimised processor for FMCW radar," in *11th European Radar Conference (EuRAD)*, Oct 2014, pp. 497–500.

[SWK85] T. Shan, M. Wax, and T. Kailath, "On spatial smoothing for direction-of-arrival estimation of coherent signals," *IEEE Trans. Acoustics, Speech and Signal Processing*, vol. 33, no. 4, pp. 806–811, Aug 1985.

[Tho82] D. Thomson, "Spectrum estimation and harmonic analysis," *Proceedings of the IEEE*, vol. 70, no. 9, pp. 1055–1096, Sept 1982.

[TN88] J. Tang and J. Norris, "LP-ZOOM, a linear prediction method for local spectral analysis of NMR signals," *Journal of Magnetic Resonance (1969)*, vol. 79, no. 1, pp. 190 – 196, 1988.

[VOK91] M. Viberg, B. Ottersten, and T. Kailath, "Detection and estimation in sensor arrays using weighted subspace fitting," *IEEE Trans. Signal Processing*, vol. 39, no. 11, pp. 2436–2449, Nov 1991.

[VS98] M. Viberg and P. Stoica, "A computationally efficient method for joint direction finding and frequency estimation in colored noise," in *Conference Record of the Thirty-Second Asilomar Conference on Signals, Systems amp; Computers* , vol. 2, Nov 1998, pp. 1547–1551 vol.2.

[VSH+00] L. Vanhamme, T. Sundin, P. V. Hecke, S. V. Huffel, and R. Pintelon, "Frequency-selective quantification of biomedical magnetic resonance spectroscopy data," *Journal of Magnetic Resonance*, vol. 143, no. 1, pp. 1 – 16, 2000.

[vT68a] H. van Trees, *Detection, Estimation, and Modulation Theory - Part 1*, 1st ed. John Wiley & Sons, 1968.

[vT68b] ——, *Detection, Estimation, and Modulation Theory - Part 3*, 1st ed. John Wiley & Sons, 1968.

[vT02] ——, *Detection, Estimation, and Modulation Theory - Part 4 Optimum Array Processing*, 1st ed. John Wiley & Sons, 2002.

[VVB88]   B. Van Veen and K. Buckley, "Beamforming: a versatile approach to spatial filtering," *IEEE ASSP Magazine*, vol. 5, no. 2, pp. 4–24, Apr 1988.

[WF94]   A. Weiss and B. Friedlander, "Preprocessing for direction finding with minimal variance degradation," *IEEE Trans. Signal Processing*, vol. 42, no. 6, pp. 1478–1485, Jun 1994.

[Win06]   M. Wintermantel, "New approach for an approximate realization of rank order filtering with low complexity," *Frequenz*, vol. 60, no. 1-2, pp. 24–28, Feb 2006.

[Win07]   V. Winkler, "Range Doppler detection for automotive FMCW radars," in *European Microwave Conference*, Oct 2007, pp. 1445–1448.

[Win12]   H. Winner, "Adaptive cruise control," in *Handbook of Intelligent Vehicles*, 1st ed., A. Eskandarian, Ed.   Springer New York, 2012, pp. 613–656.

[Win15]   ——, "Radarsensorik," in *Handbuch Fahrerassistenzsysteme - Grundlagen, Komponenten und Systeme für aktive Sicherheit und Komfort*, 3rd ed., H. Winner, S. Hakuli, F. Lotz, and C. Singer, Eds.   Springer, 2015, pp. 259–316.

[WM14]   C. Waldschmidt and H. Meinel, "Future trends and directions in radar concerning the application for autonomous driving," in *11th European Radar Conference (EuRAD)*, Oct 2014, pp. 416–419.

[WZ89]   M. Wax and I. Ziskind, "On unique localization of multiple sources by passive sensor arrays," *IEEE Trans. Acoustics, Speech and Signal Processing*, vol. 37, no. 7, pp. 996–1000, Jul 1989.

[Yeo08]   M. Yeomans, "Radar receivers," in *Radar Handbook*, 3rd ed., M. Skolnik, Ed.   Mc Graw Hill, 2008, pp. 6.1–6.51.

[ZCD$^+$09]   J. Zhang, M. Christensen, J. Dahl, S. Jensen, and M. Moonen, "Subband implementation of the harmonic music algorithm," in *IEEE International Conference on Acoustics, Speech and Signal Processing*, April 2009, pp. 309–312.

[ZHM96]   M. Zoltowski, M. Haardt, and C. P. Mathews, "Closed-form 2-d angle estimation with rectangular arrays in element space or beamspace via unitary esprit," *IEEE Trans. Signal Processing*, vol. 44, no. 2, pp. 316–328, Feb 1996.

[ZKS93]   M. Zoltowski, G. Kautz, and S. Silverstein, "Beamspace root-music," *IEEE Trans. Signal Processing*, vol. 41, no. 1, pp. 344–, Jan 1993.

[ZL91a]   M. Zoltowski and T.-S. Lee, "Interference cancellation matrix beam-forming for 3-D beamspace ML/MUSIC bearing estimation," *IEEE Trans. Signal Processing*, vol. 39, no. 8, pp. 1858–1876, Aug 1991.

[ZL91b]   ——, "Maximum likelihood based sensor array signal processing in the beamspace domain for low angle radar tracking," *IEEE Trans. Signal Processing*, vol. 39, no. 3, pp. 656–671, Mar 1991.

[Zol88]   M. Zoltowski, "High resolution sensor array signal processing in the beamspace domain: novel techniques based on the poor resolution of fourier beamforming," in *Fourth Annual ASSP Workshop onSpectrum Estimation and Modeling*, Aug 1988, pp. 350–355.

Curriculum Vitae

Name:	Florian Engels
Date of birth:	October 29th, 1979
Place of birth:	Wuppertal, Germany
Citizenship:	German
Familiy status:	married, three children

Education

09/2006 - 11/2008	Universität Karlsruhe (TH), Electrical Engineering and Information Technology, Master of Science (M.Sc.)
04/2003 - 04/2006	Bergische Universität Wuppertal, Electrical Engineering and Information Technology, Bachelor of Science (B.Sc.)

Work experience

Since 07/2015	Leading Technical Expert Radar Signalprocessing, A.D.C. GmbH (Continental AG)
11/2008 - 06/2015	Development Engineer Radar, A.D.C. GmbH (Continental AG)